ANOMALY DETECTION IN DIVERSE SENSOR NETWORKS USING MACHINE LEARNING

A DISSERTATION SUBMITTED TO

THE GRADUATE SCHOOL OF ENGINEERING AND SCIENCE

OF BILKENT UNIVERSITY

IN PARTIAL FULFILLMENT OF THE REQUIREMENTS FOR

THE DEGREE OF

DOCTOR OF PHILOSOPHY

IN

ELECTRICAL AND ELECTRONICS ENGINEERING

By

Ali Alp Akyol

January 2022

ANOMALY DETECTION IN DIVERSE SENSOR NETWORKS USING MACHINE LEARNING

By Ali Alp Akyol

January 2022

We certify that we have read this dissertation and that in our opinion it is fully adequate, in scope and in quality, as a dissertation for the degree of Doctor of Philosophy.

Orhan Arıkan(Advisor)

Sinan Gezici

Selim Aksoy

Cenk Toker

Gökhan Muzaffer Güvensen

Approved for the Graduate School of Engineering and Science:

Ezhan Karaşan
Director of the Graduate School

ABSTRACT

ANOMALY DETECTION IN DIVERSE SENSOR NETWORKS USING MACHINE LEARNING

Ali Alp Akyol
Ph.D. in Electrical and Electronics Engineering
Advisor: Orhan Arıkan
January 2022

Earthquake precursor detection is one of the oldest research areas that has the potential of saving human lives. Recent studies have enlightened the fact that strong seismic activities and earthquakes affect the electron distribution of the ionosphere. These effects are clearly observable on the ionospheric Total Electron Content (TEC) that shall be measured by using the satellite position data of the Global Navigation Satellite System (GNSS). In this dissertation, several earthquake precursor detection techniques are proposed and their precursor detection performances are investigated on TEC data obtained from different sensor networks.

First, a model based earthquake precursor detection technique is proposed to detect precursors of the earthquakes with magnitudes greater than 5 in the vicinity of Turkey. Precursor detection and TEC reliability signals are generated by using ionospheric TEC variations. These signals are thresholded to obtain earthquake precursor decisions. Earthquake precursor detections are made by using Particle Swarm Optimization (PSO) technique on these precursor decisions. Performance evaluations show that the proposed technique is able to detect 14 out of 23 earthquake precursors of magnitude larger than 5 in Richter scale while generating 8 false precursor decisions.

Second, a machine learning based earthquake precursor detection technique, EQ-PD is proposed to detect precursors of the earthquakes with magnitudes greater than 4 in the vicinity of Italy. Spatial and spatio-temporal anomaly detection thresholds are obtained by using the statistics of TEC variation during seismically active times and applied on TEC variation based anomaly detection signal to form precursor decisions. Resulting spatial and spatio-temporal anomaly decisions are fed to a Support Vector Machine (SVM) classifier to generate earthquake precursor detections. When the precursor detection performance of the EQ-PD is investigated, it is observed that the technique is able to detect 22 out of 24 earthquake precursors while generating 13 false precursor decisions during

147 days of no-seismic activity.

Last, a deep learning based earthquake precursor detection technique, DL-PD is proposed to detect precursors of the earthquakes with magnitudes greater than 5.4 in the vicinity Anatolia region. The DL-PD technique utilizes a deep neural network with spatio-temporal Global Ionospheric Map (GIM)-TEC data estimation capabilities. GIM-TEC anomaly score is obtained by comparing GIM-TEC estimates with GIM-TEC recordings. Earthquake precursor detections are generated by thresholding the GIM-TEC anomaly scores. Precursor detection performance evaluations show that DL-PD shall detect 5 out of 7 earthquake precursors while generating 1 false precursor decision during 416 days of no-seismic activity.

Keywords: Machine Learning, Deep Learning, ionosphere, earthquake precursor detection, Global Navigation Satellite System (GNSS).

ÖZET

ÇEŞİTLİ SENSÖR AĞLARINDA MAKİNE ÖĞRENİMİ İLE ANOMALİ TESPİTİ

Ali Alp Akyol
Elektrik ve Elektronik Mühendisliği, Doktora
Tez Danışmanı: Orhan Arıkan
Ocak 2022

Deprem öncül tespiti, insan hayatını kurtarma potansiyeline sahip olan en eski araştırma alanlarından biridir. Yapılan son çalışmalar, güçlü sismik aktivitelerin ve depremlerin iyonosferin elektron dağılımını etkilediğini göstermiştir. İyonosferdeki bu etkiler, Küresel Konum Belirleme Sistemlerinin uydu pozisyonu verileri kullanılarak ölçülebilen, Toplam Elektron İçeriği (TEİ) üzerinde açıkça gözlemlenmektedir. Bu tezde, çeşitli deprem öncül tespit teknikleri önerilmiş, önerilen bu tekniklerin öncül tespit başarımları farklı sensör ağlarından elde edilen TEİ verileri üzerinde irdelenmiştir.

İlk olarak, Türkiye ve çevresinde meydana gelmiş 5 şiddeti üzerindeki depremlerin öncüllerinin tespit edilmesi amacıyla, model tabanlı bir deprem öncül tespit tekniği önerilmiştir. TEİ değişimleri kullanılarak deprem öncül tespit ve TEİ güvenilirlik sinyalleri oluşturulmuştur. Oluşturulan bu sinyallerin eşiklendirilmesi ile deprem öncülü kararları elde edilmiştir. Elde edilen deprem öncülü kararları üzerinde Parçacık Sürüsü Optimizasyonu (PSO) tekniği kullanılarak deprem öncül tespitleri üretilmektedir. Başarım değerlendirmeleri, önerilen tekniğin Richter ölçeğinde 5 şiddeti üzerinde meydana gelmiş 23 depremden 14 tanesine ait öncülleri doğru tespit ederken 8 yanlış öncül kararı verdiğini göstermektedir.

İkinci olarak, İtalya ve çevresinde meydana gelmiş 4 şiddeti üzerindeki depremlerin öncüllerinin tespit edilmesi amacıyla, makine öğrenimi tabanlı bir deprem öncül tespit tekniği olan EQ-PD önerilmiştir. Sismik aktivitenin olduğu zamanlara ait TEİ değişim istatistikleri kullanılarak, uzaysal ve uzay-zamansal anomali tespit eşikleri elde edilmiş ve öncül kararlarının oluşturulması amacıyla, TEİ değişimi tabanlı anomali tespit sinyaline uygulanmıştır. Elde edilen uzaysal ve uzay-zamansal öncül kararları, deprem öncül tespitlerinin oluşturulması için Destek Vektör Makinesi (DVM) sınıflandırıcısına beslenmiştir. EQ-PD tekniğinin deprem öncül tespit performansı incelendiğinde, tekniğinin 24 deprem öncülünden 22'sini doğru tespit ederken 147 sismik aktivite olmayan günde 13 yanlış alarm

ürettiği gözlemlenmiştir.

Son olarak, Anadolu bölgesinde meydana gelmiş 5.4 şiddeti üzerindeki depremlerin öncüllerinin tespit edilmesi amacıyla, derin öğrenme tabanlı bir deprem öncül tespit tekniği olan DL-PD önerilmiştir. DL-PD tekniği uzay-zamansal Küresel İyonosferik Harita (KİH)-TEİ veri kestirimi kabiliyetine sahip bir yapay sinir ağı kullanmaktadır. KİH -TEİ kestirimleri ve KİH -TEİ ölçümleri karşılaştırılarak, KİH -TEİ anomali skorları elde edilmiştir. Deprem öncül tespitleri KİH -TEİ anomali skorlarının eşiklendirilmesi ile oluşturulmuştur. Öncül tespit başarımları incelendiğinde, DL-PD tekniğinin 7 deprem öncülünden 5'ini doğru tespit ederken 416 sismik aktivite olmayan günde 1 yanlış alarm ürettiği gözlemlenmiştir.

Anahtar sözcükler: Makine Öğrenimi, Derin Öğrenme, iyonosfer, deprem öncül tespiti, Küresel Konum Belirleme Sistemi.

Acknowledgement

First, I would like to thank my supervisors, Prof. Dr. Orhan Arıkan and Prof. Dr. Feza Arıkan, for their supervision, special guidance, suggestions, and support throughout my study. I would especially want to thank Prof. Dr. Orhan Arıkan for his invaluable encouragement and motivation through the development of this thesis.

I also thank Prof. Dr. Sinan Gezici and Prof. Dr. Selim Aksoy as my Thesis Tracking Committee members for their helps on the way of developing machine learning and deep learning models, reading this thesis and being a member of my thesis dissertation committee. Also, I would like to thank Prof. Dr. Cenk Toker and Asst. Prof. Gökhan Muzaffer Güvensen for approving my work, reading this thesis and being a member of my thesis dissertation committee.

There are some colleagues and friends who directly or indirectly contributed to my completion of this thesis. I am grateful for my colleagues Caner Tezel, Haluk Doğuş Sezer, Emre Kalender and Hüseyin Emre Şahinbay with being positive, sharing ideas and put a smile on my face each work day. I thank my friends Fatih Emre Şimşek, Taha Ufuk Taşcı, Güneş Bayır and Fatih Aslan for their understanding and support. I also thank my friends Ferman Kırkan, Serhan Taşcı, Seckin Bildik and Onur Taşoğlan for always being there to listen and motivate.

I am also appreciative of the financial and technical support from TUBITAK 114E541, 115E915, Joint TUBITAK 114E092 and AS CR 14/001 projects.

Finally, but forever I would express my thanks to my family, Mustafa and Melahat Akyol, and my loving wife Aycan Akyol for their love, encouragement and endless moral support.

Contents

List of Figures

List of Tables

Chapter 1

INTRODUCTION

Earthquakes (EQs) are one of the oldest and deadliest of the natural disasters. They can cause colossal damage on buildings, structures and living quarters that result with loss of hundreds of human lives, injuries, fires and economic losses. This is an inevitable fact that EQs still have a dangerous impact on human lives in spite of advancements in the construction technologies of the buildings. Detrimental effects of EQs are hard to prevent, since EQ epicenter, EQ magnitude and time of onset are uncertain for humanity. EQ prediction aims to estimate, epicenter, magnitude and time of EQs [1]. Sadly, an EQ prediction technique that can estimate epicenter, magnitude and time of EQs accurately has not been developed yet. Hence, from decades EQ prediction is one of the challenging research areas which aims to unveil uncertainties regarding the EQs. In the following sections, EQ prediction and EQ precursor detection studies are detailed.

1.1 Earthquake Prediction Studies

There are a still ongoing discussions on the predictability of EQs. These discussions focus on the obscurity of underlying seismic activity and EQ preparation

mechanisms and reliability of the possible EQ precursor based prediction techniques [2, 3]. Despite the underlying seismic activity triggered phenomenon is not fully comprehended, the ongoing discussion has not bring to a conclusion yet. Furthermore, EQ prediction related literature consists of empirical case studies that are conducted to detect EQ precursory signals after a strong EQ had taken place. Due to the lack of comprehensive studies that investigate the precursory signal behaviors for longer time intervals, critics related with the reliability and repeatability of these techniques still exist [4].

EQ prediction techniques in the literature shall be grouped into model based and precursor based prediction techniques. Model based techniques aim to fit a mathematical, machine learning or deep learning model to simulate a recurrence behaviour between past seismic activities or EQs with the upcoming EQs. Some of the chosen mathematical EQ prediction models in the literature shall be listed as follows. An EQ reappearance model proposed a relationship between fault line strain related forces and EQ reappearance periodicity [5]. Another model that uses Poisson's distributions and distance factors claims that all the EQ occurrences in a fault zone are related and shall be predicted [6]. Similarly, a probabilistic model is proposed to predict location, magnitude and time of the upcoming EQs [7]. A Fibonacci Lucas Dual model is fitted to past EQ occurrence times to predict upcoming EQ recurrence times [8].

In recent years, several machine learning based models are also proposed to predict EQ locations, magnitudes or occurrence times. These machine learning models are based on: boosting techniques such as AdaBoost, decisions trees and random forests, multi-objective info-fuzzy network, unsupervised techniques such as k-nearest neighbors, Support Vector Machine (SVM) and artificial neural networks [9, 10, 11, 12, 13]. Furthermore, SVM regressors and hybrid neural networks are trained to predict EQs on a chosen earthquake catalog [14]. Deep learning based models are also proposed [15, 16, 17, 18, 19]

1.2 Earthquake Precursor Detection Studies

Earthquake precursor detection related studies aims to detect anomalies in various precursory signals prior to strong EQs. These precursory signals shall be generated from radon gas emissions [20, 21], ionospheric phenomenon [22, 23, 24, 25, 26], temperature variations [27, 28, 29], chemical composition of underground water [30, 21] and even unusual animal behaviour [31] or strange lights [32].

There are studies suggesting the possible coupling mechanisms between seismic activities and state of the ionosphere prior to strong EQs. A possible coupling mechanism between Earth's lithosphere, atmosphere and ionosphere is proposed in [33]. The Lithosphere Atmosphere Ionosphere Coupling (LAIC) model claims that seismic activity or tectonic plate movements generate radom gas emission from Earth's crust through atmosphere. Released radom gases ionize air in atmosphere that results with changes in ionosphere. These changes are observed in critical frequency of maximum ionization layer (foF2), maximum ionization height (hmF2) and Total Electron Content (TEC) parameters of the ionosphere. Another physical coupling mechanism is proposed in [34]. The proposed claims that low height of planetary boundary layer (PBL) causes accumulation of radon gases that are released from Earth's crust. This radon gas accumulation results with high ionization in ionosphere during the nighttime. Furthermore, the proposed also claimed that resulting positive electron density anomalies have a unique characteristic. Hence, it is possible to create a pattern (mask) which may serve as an EQ precursor signal for upcoming strong EQs.

Comprehensive investigations are performed on the possible correlations between F2 layer ionospheric parameters and seismic activities and EQs. A preliminary statistical analysis for foF2 critical frequencies that are measured at Chung-Li (Taiwan Island) ground based station is performed for the EQs with magnitudes $M \geq 4$ that had taken place near this ground based station for the time period from 1978 to 1986 [35]. Ionospheric data is processed for 6 days prior to the each chosen EQ time. Results of this study claim that shallow focus EQs (z

$<$ 60 km) hardly generates a detectable EQ precursor while the deep focus EQs (60 km $<$ z $<$ 300 km) causes significant increase in the ionospheric response prior to upcoming EQs with magnitudes $M \geq 4$. Another study is conducted on the EQs which had taken place in Taiwan area during the period of 1997 - 1999 [36]. Results of this study suggest that it is possible to observe foF2 and TEC anomalies 1 to 7 days prior to investigated EQs. Similarly, another ionospheric foF2 related statistical investigation is performed for the 184 EQs with magnitude $M \geq 5.0$ during 1994 - 1999 in the Taiwan area [37]. The study reported empirical evidences to pre-earthquake ionospheric anomalies (PEIAs) 1 to 5 days prior to 184 $M \geq 5.0$ investigated earthquakes. Another comprehensive study is conducted to investigate relationship between ionospheric TEC anomalies and seismic activities. In the study, TEC data is extracted from Global Ionosphere Maps (GIM) [38]. During the investigation, 736 $M \geq 6.0$ earthquakes around the world during 2002 - 2010 are selected. TEC anomalies are defined on the chosen TEC data with respect to chosen EQs. Statistics of anomaly occurrence rates for 1-21 days prior to the EQs (PE) and the background days with no seismic activity (PN) are calculated. Results of the investigation revealed that rate of TEC anomalies start increasing for 10 days prior to EQs. Furthermore, probability of observing a TEC anomaly during 1 to 10 days prior to a strong EQ is 1.8 to 3.6 times more likely compared to observing these TEC anomalies during chosen background days. In another statistical study, pre-EQ ionospheric anomalies are investigated on TEC data obtained from GIM for the chosen EQs around Japan [39]. Results of the study suggest the fact that probability of observing the GIM-TEC anomalies gets higher when 1 to 5 days prior to investigated EQs. The presented statistical investigations [35, 36, 37, 38, 39] conducted their investigations during the seismically active time periods that detected ionospheric anomalies are attributed to seismic activities. Hence, reoccurrence statistics of ionospheric anomalies when there is no seismic activity remain uncertain.

There are also other ionospheric precursor related studies that report ionospheric anomalies prior to strong EQs around Italy [40, 41, 42, 43], Taiwan [44, 45, 46], Indonesia [47], Japan [23, 48, 49, 26], Chile [25, 50], India [51], Nepal [52], China [53, 23], Mexico [24, 54, 55], El-Salvador [56], USA

[57, 58] and Turkey [59, 60, 61]. In these studies, various statistical methods have been practiced to understand the relationship between ionospheric variations and seismic activities such as: TEC variation and difference analysis [25, 23, 48, 49, 50, 56, 59], ionospheric correction [51], inter-quartile and percentile analysis [26, 44, 45, 46, 52, 53], correlation analysis between TEC and foF2 [24, 58, 55, 54], equatorial TEC abnormality analysis [47], ionospheric parameter based precursor pattern generation [43], relative TEC deviation analysis [41, 57] and seismo-ionospheric variation investigation [40] and detection [42].

1.3 Contributions of the Thesis

When the previous EQ precursor related research studies are taken into consideration, these research fall short on providing statistical characterizations of their EQ prediction capabilities due to following reasons.

1. Most of these studies are post-EQ techniques that conduct statistical analysis on ionospheric data in the aftermath of a strong EQ.

2. Typically, statistical analysis is conducted on a relatively short time interval leading to EQs of magnitude 6 or higher. There is no statistical analysis of false alarms over larger periods of data.

Therefore, pre-EQ or real-time EQ precursor detection and false alarm performances of these methods are highly uncertain and might lead to inconsistent EQ precursor detections.

An objective investigation on relationship between TEC based ionospheric anomalies and EQ precursors is conducted in [61], [60]. These investigations revealed the fact that TEC based ionospheric anomalies are correlated with the EQ preparation process and probability of observing such TEC anomalies prior to strong EQs is notably higher than observing these anomalies when there is no

seismic activity. In this dissertation, model based, machine learning based (EQ-PD) and deep learning based (DL-PD) EQ precursor detection techniques are presented. The proposed techniques contributes to the literature in the following aspects.

1. Precursor detection performances of the proposed techniques are evaluated by dividing each day into two separate classes: seismic activity days and no-seismic activity days. Number of days in no-seismic activity class is greater than seismic activity class days in all investigations.
2. The model based and machine learning based techniques are trained in a supervised way that during the training set of days seismic activity and no-seismic activity class information of each day is processed. Hence, these proposed techniques are trained, validated and tested for unbiased precursor detection performance evaluations.
3. During the training of the model based and machine learning based techniques, geomagnetic parameters are also processed to increase the reliability of precursor decisions.
4. EQ-PD is a novel Boosting technique which combines multiple EQ precursor decisions to generate a final EQ precursor detection.
5. DL-PD is a deep learning technique which can be trained in an unsupervised way that during the training seismic activity information is not processed. DL-PD is capable of reliably predicting the future GIM-TEC data from the past.

1.4 Organization of the Thesis

This dissertation consists of three different EQ precursor detection studies presented in detail in the following chapters. Chapter 2 is an extension of a previous study detailed in [60]. In [60], it is shown that there is a correlation between seismic activities and ionospheric TEC. In Chapter 2, a model based EQ precursor

detection technique is implemented by exploiting the results of the previous study. In Chapter 3, a machine learning based EQ precursor detection technique that process TEC data obtained from EUREF Permanent GNSS Network to detect precursors of EQs around Italy is presented [62]. In Chapter 4, a deep learning based EQ precursor detection technique that process GIM-TEC data obtained from International GNSS Service to detect precursors of EQs around Anatolian region is proposed. Finally, Chapter 5 concludes this dissertation with future research directions.

Chapter 2

MODEL BASED EARTHQUAKE PRECURSOR DETECTION TECHNIQUE

GPS networks with precisely known receiver positions are deployed to provide highly accurate real-time geolocation information. These permanently located GPS networks shall also generate indirect ionospheric TEC measurements for monitoring state of the ionosphere.

In this work, TEC measurements of Turkish National Permanent GPS Network (TNPGN) are processed and presented in Section 2.1. There are multiple sources of ionization in the ionosphere, such as strong solar radiation, radon gas emission, ionospheric chemistry and strong seismic activities. The TEC measurements vary both spatially and temporally due to ionization in the atmosphere. The proposed model based earthquake precursor detection technique relies on detection of local TEC anomalies that are triggered by strong seismic activities on the earth's crust.

The proposed detection technique consists of five sequential processing stages. First of all, TEC measurements are estimated by using a spatio-temporal estimation technique as detailed in Section 2.2. Then, earthquake precursor detection

and TEC reliability signals are generated as presented in Section 2.3 and Section 2.4, respectively. Generated earthquake precursor detection signal is thresholded for declaring a precursor decision by using precursor detection thresholds as described in Section 2.5. Declared precursor decisions are validated by anomaly detectors that use TEC reliability signal and detection parameters to assess reliability of the anomaly decisions as introduced in Section 2.6. Finally, as detailed in Section 2.6.3, validated precursor decisions of the precursor detectors are fused to generate final earthquake precursor detections that has higher robustness and performance in terms of lower false alarm rates.

2.1 Turkish National Permanent GPS Network (TNPGN)

The TNPGN is a Global Navigation Satellite System (GNSS) network with 158 operational reference stations which are deployed across Turkey and Northern Cyprus. The TNGPN is operational since 2009 and all its reference stations are presented in Fig. 2.1.

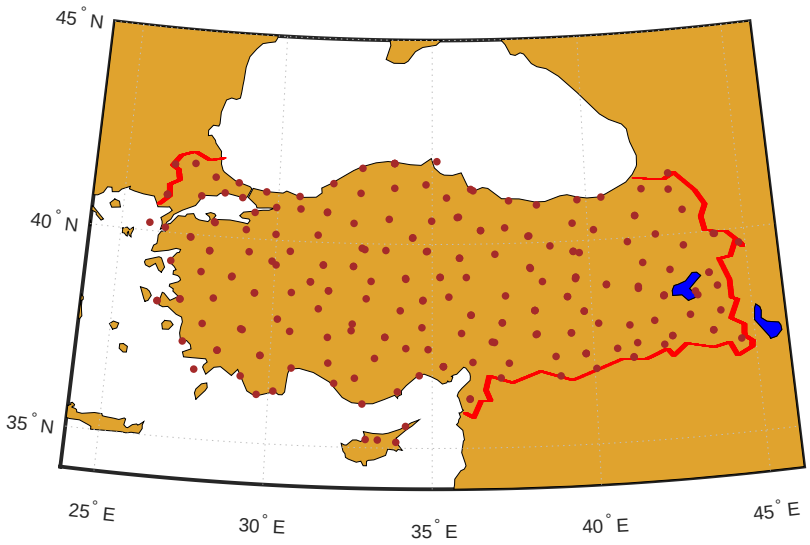

Figure 2.1: TNGPN reference station locations.

Raw TEC data which is recorded at each operational reference station is processed by IONOLAB-TEC and IONOLAB-BIAS services [63, 64]. Pre-processed TEC measurements shall be generated with a time separation of 0.5 seconds. In this work, TEC measurements with time separation of 2.5 minutes are post processed. Samples of the processed TEC data are presented in Fig. 2.2.

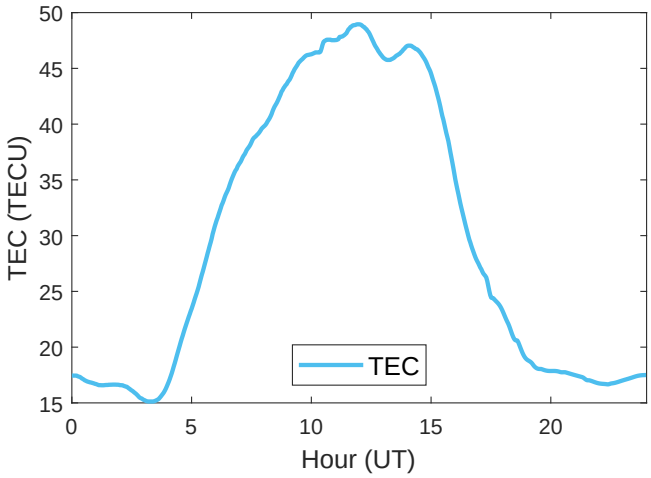

(a)

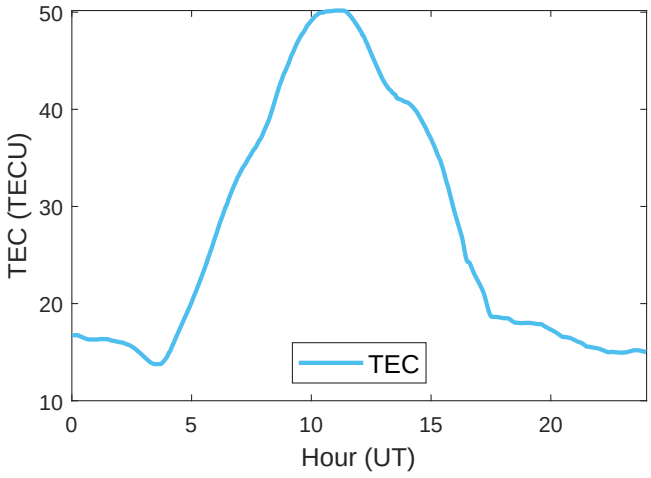

(b)

Figure 2.2: Daily TEC measurements at station "datc" on two different dates: (a) 16.10.2011 and (b) 17.10.2011.

For two different dates of 16.10.2011 and 17.10.2011, pre-processed daily TEC measurements at reference station with code name "datc" are visualized. As seen

in Fig. 2.2, despite the daily TEC measurements are recorded in two consecutive days, there are temporal differences between the hourly TEC recordings.

2.2 A spatio-temporal TEC interpolation technique

Anomalous behaviours in TEC measurements shall be detected by generating estimates for the TEC measurements and comparing these estimates with the TEC measurements. The TEC estimate of a reference station shall be generated by using the TEC measurements of neighbouring reference stations (spatial TEC estimation), past TEC measurements of the same reference station (temporal TEC estimation) or both past TEC measurements of the reference station and its neighbours (spatio-temporal TEC estimation). In this work, a spatio-temporal TEC estimation technique is implemented [65, 60].

Let $\mathbf{x}_{u;d}$ ($(N_{u;d} \times 1)$ column vector) defined as the available TEC data at reference station u on day d:

$$\mathbf{x}_{u;d} = [x_{u;d}(1) \cdots x_{u;d}(n) \cdots x_{u;d}(N_{u;d})]^T, \tag{2.1}$$

where $N_{u;d}$ is the total number of TEC measurements, $x_{u;d}(n)$, is the n^{th} TEC measurement of $N_{u;d}$ consecutive TEC measurements. Neighboring reference stations of the reference station u shall be chosen with respect to a circle where center of the circle is u reference station location and radius of the circle is R_r km. TEC data of the v'th reference station which is located within the circle shall be defined as $\mathbf{x}_{v;d;R_r}$ ($(N_{u;d} \times 1)$ vector) and total number of neighboring reference stations shall be defined as $N_{u;R_r}$. Then a spatio-temporal TEC estimate of the chosen reference station u on day d, $\hat{\mathbf{x}}_{u;d;R_r}$ shall be obtained as:

$$\hat{\mathbf{x}}_{u;d;R_r} = \sum_{v=1}^{N_{u;R_r}} \alpha_{u;d;R_r}(v)\mathbf{x}_{v;d;R_r}, \tag{2.2}$$

where $\alpha_{u;d;R_r}(v)$ is weight of the v^{th} neighboring station. Hence, weights vector $\boldsymbol{\alpha}_{u;d;R_r}$ ($N_{u;R_r} \times 1$) shall be defined as the unique solution of the following

minimization:

$$\boldsymbol{\alpha}_{u;d;R_r} = \underset{\alpha_{u;d;R_r}(v)}{\operatorname{argmin}} \sum_{d_i}^{d_s} \left\| \mathbf{x}_{u;d_n} - \sum_{v=1}^{N_{u;R_r}} \alpha_{u;d;R_r}(v) \mathbf{x}_{v;d_n;R_r} \right\|_2^2. \tag{2.3}$$

$\boldsymbol{\alpha}_{u;d;R_r}$ shall also be obtained in closed form as:

$$\underline{\boldsymbol{\alpha}}_{u;d;R_r} = \left(\sum_{d_n=d_i}^{d_s} \mathbf{X}_{u;d_n;R_r}^T \mathbf{X}_{u;d_n;R_r} \right)^{-1} \left(\sum_{d_n=d_i}^{d_s} \mathbf{b}_{u;d_n;R_r} \right), \tag{2.4}$$

where $\mathbf{X}_{u;d_n;R_r}$ matrix $(N_{u;d} \times N_{u;R_r})$ is formed by combining multiple TEC measurements of R_r km. neighbouring reference stations as:

$$\mathbf{X}_{u;d_n;R_r} = [\mathbf{x}_{1;d_n;R_r} \dots \mathbf{x}_{v;d_n;R_r} \dots \mathbf{x}_{N_{u;R_r};d_n;R_r}], \tag{2.5}$$

and $\mathbf{b}_{u;d_n;R_r}$ vector $(N_{u;R_r} \times 1)$ is defined as:

$$\mathbf{b}_{u;d_n;R_r} = \mathbf{X}_{u;d_n;R_r}^T \mathbf{x}_{u;d_n}. \tag{2.6}$$

Ionosphere electron density and the strong solar radiation based magnetic activity of the sun are highly correlated. Sun spot number (SSN) is a widely used index to monitor sun and solar activity in a daily basis [66]. Since the proposed spatio-temporal TEC estimation technique depends on past TEC observations, days within $[d_i, d_s]$ in (2.4) are clustered with respect to their corresponding SSN. Past TEC data which is in the same cluster with the estimation day is processed during the minimization in (2.4). Hence, the minimization process is temporally correlated with the magnetic activity of the sun.

By using the obtained weights $\underline{\boldsymbol{\alpha}}_{u;d_n;R_r}$, $\hat{\mathbf{x}}_{u;d;R_r}$ can be computed and compared to $\mathbf{x}_{u;d}$ to detect the local TEC anomalies. TEC estimation performance of the spatio-temporal TEC interpolation technique is presented in Table 2.1 and Fig. 2.3 for the reference station "datc" on two different 16.10.2011 and 17.10.2011 that are also illustrated on the Fig. 2.2. Root Mean Square TEC estimation error, $TEC_{RMS,u,d}$ is defined in (2.7), and calculated for the reference station and the chosen dates. As shown in the Table 2.1, root mean squared error (RMS) of both estimation dates are close to zero.

$$\hat{\mathbf{x}}_{RMS,u,d,R_r} = \sqrt{\frac{1}{N_{u,d}} \left\| \mathbf{x}_{u;d} - \hat{\mathbf{x}}_{u;d;R_r} \right\|_2^2} \tag{2.7}$$

Table 2.1: RMS error for the TEC measurements and their estimates at reference station "datc" on two different dates: 16.10.2011 and 17.10.2011.

16.10.2011 "Datça" Sunspot Number : 60	17.10.2011 "Datça" Sunspot Number : 74
$\hat{\mathbf{x}}_{RMS,u,d,R_r} = 0.4230$ TECU	$\hat{\mathbf{x}}_{RMS,u,d,R_r} = 0.4214$ TECU

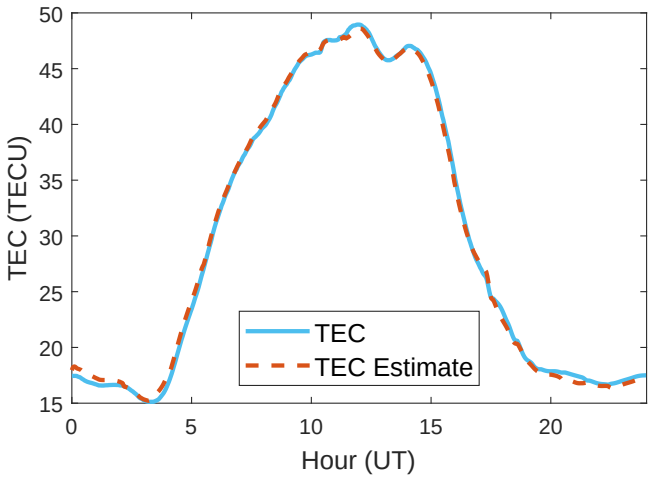

(a)

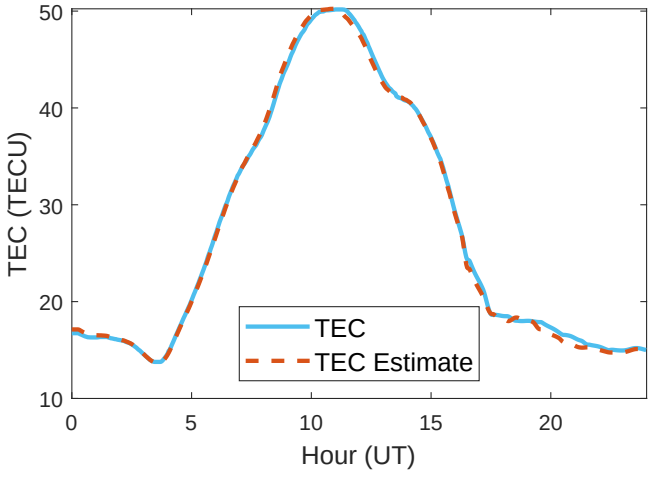

(b)

Figure 2.3: Daily TEC measurements and their estimates at station "datc" on two different dates: (a) 16.10.2011 and (b) 17.10.2011.

2.3 Generation of the Earthquake Precursor Detection Signal

An anomaly shall be defined as a "variation from the norm." [67]. Detection of an TEC anomaly requires comparing the TEC measurements with the norm or i.e. TEC estimates. Result of this comparison is the anomaly score of the compared TEC measurements or i.e. local TEC variation. Amount of local TEC variation on a TEC measurement and its estimate shall be calculated by using Symmetric Kullback-Leibler Distance (SKLD) between the normalized $\mathbf{x}_{u;d}$ and its normalized estimate $\hat{\mathbf{x}}_{u;d;R_r}$ [68, 69]:

$$SKLD(P_{u;d}; \hat{P}_{u;d;R_r}) = KLD(\hat{P}_{u;d;R_r}|P_{u;d}) + KLD(P_{u;d}|\hat{P}_{u;d;R_r}), \tag{2.8}$$

where KLD is the Kullback-Leibler Distance given by:

$$KLD(\hat{P}_{u;d;R_r}|P_{u;d}) = \left(\sum_{n=1}^{N_{u;d}} \hat{P}_{u;d;R_r}(n) ln \left(\frac{\hat{P}_{u;d;R_r}(n)}{P_{u;d}(n)} \right) \right), \tag{2.9}$$

$$KLD(P_{u;d}|\hat{P}_{u;d;R_r}) = \left(\sum_{n=1}^{N_{u;d}} P_{u;d}(n) ln \left(\frac{P_{u;d}(n)}{\hat{P}_{u;d;R_r}(n)} \right) \right), \tag{2.10}$$

where $P_{u;d}$ and $\hat{P}_{u;d;R_r}$ are the normalized $\mathbf{x_{u;d}}$ and $\hat{\mathbf{x}}_{\mathbf{u;d;R_r}}$ as:

$$P_{u;d} = \frac{\mathbf{x}_{u;d}}{\|\mathbf{x}_{u;d}\|_1}, \tag{2.11}$$

$$\hat{P}_{u;d;R_r} = \frac{\hat{\mathbf{x}}_{u;d;R_r}}{\|\hat{\mathbf{x}}_{u;d;R_r}\|_1}. \tag{2.12}$$

Earthquake precursor detection signal which can serve to detect anomalies on local TEC variations is constructed by 2D interpolation of all the calculated SKLDs for all stations in the TNPGN [70, 71]. For two consecutive dates: 29.08.2011 and 30.08.2011, earthquake precursor detection signals are generated and presented in Fig. 2.4. As shown in Fig. 2.4, despite dates of the generated precursor detection signals are two consecutive days, they show spatial and temporal local TEC variation differences.

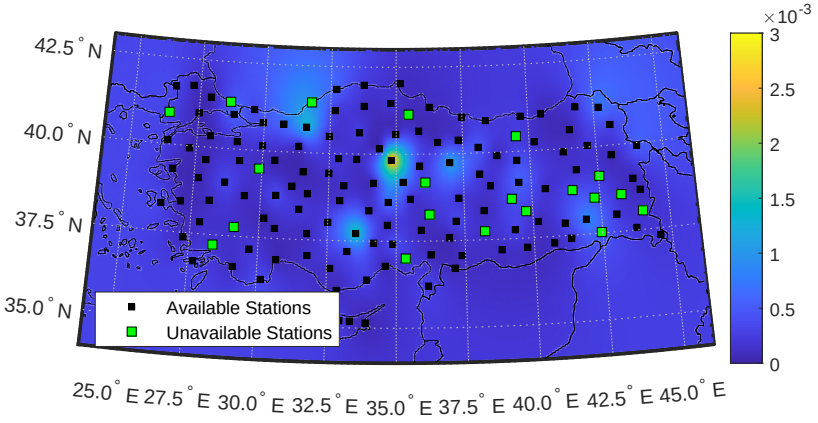

(a)

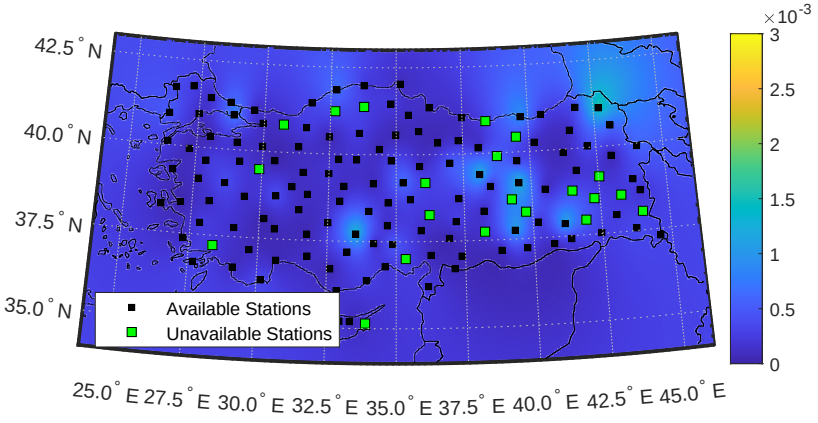

(b)

Figure 2.4: Visualization of earthquake precursor detection signals for two different dates: (a) 29.08.2011 with sunspot number 34 and (b) 30.08.2011. with sunspot number 51.

2.4 Generation of the TEC Reliability Signal

Ionospheric TEC disturbances are not only triggered by the solar radiation and the seismic activities but also affected by the geomagnetic storms. For robust

and reliable detection of local TEC anomalies, TEC anomalies that are caused by the geomagnetic storms should be taken into consideration by monitoring geomagnetic storm related parameters. D_{st}, K_p and the planetary ionospheric storm index W_p are some of the widely used parameters for identifying the geomagnetic storms [72]. W_p can easily be obtained by using TEC measurements and can serve to identify the ionospheric storms even under magnetically quiet-time conditions [73, 74]. Hence, W_p is a reasonable candidate for assessing the reliability of TEC measurements. W_p parameter is a discrete parameter that can be obtained by categorizing ionosphere variability, $\mathbf{w}_{u;d}$. $\mathbf{w}_{u;d}$ can take both negative and positive values indicating negative and positive geomagnetic storms as their magnitudes are proportional to $\mathbf{w}_{u;d}$, respectively. As the $\mathbf{w}_{u;d}$ gets closer to zero, state of the ionosphere gets more quiet. To represent reliability of local variation in TEC for the detection of local anomalies due to seismic activities, $\mathbf{w}_{u;d}$ shall be defined as:

$$\mathbf{w}_{u;d} = log_{10}(\mathbf{x}_{u;d}/x_{u;d;med}), \tag{2.13}$$

where local ionosphere variability, $\mathbf{w}_{u;d}$ is an unquantized version of the ionospheric W_p parameter and $x_{u;d;med}$ is defined as the median of 7 days TEC preceding the day d, at station u.

In this work, earthquake precursor detection signals are generated by calculating SKLD based local TEC variations for each and every station in the GPS network. Similarly, TEC reliability signals are generated by calculating local ionosphere variabilities, $\mathbf{w}_{u;d}$ for each and every station in the GPS network. Thereafter, an estimate of local ionosphere variabilities, $\hat{\mathbf{w}}_{u;d}$ is generated by the spatio-temporal algorithm as described in Section 2.2 to reduce spatial variation of the local ionosphere variabilities. The TEC reliability score, $TEC_{\alpha;u;d}$ for reference station u and day d shall be defined as follows:

$$TEC_{\alpha;u;d} = max(\hat{w}_{u;d}). \tag{2.14}$$

Similarly, TEC reliability signal which shall serve to assess reliability of the TEC measurements is also generated by 2D interpolation of all the calculated TEC reliability scores for all stations in the TNPGN. Fig. 2.5 illustrates generated TEC reliability signals for the same days that are also presented in Fig. 2.4.

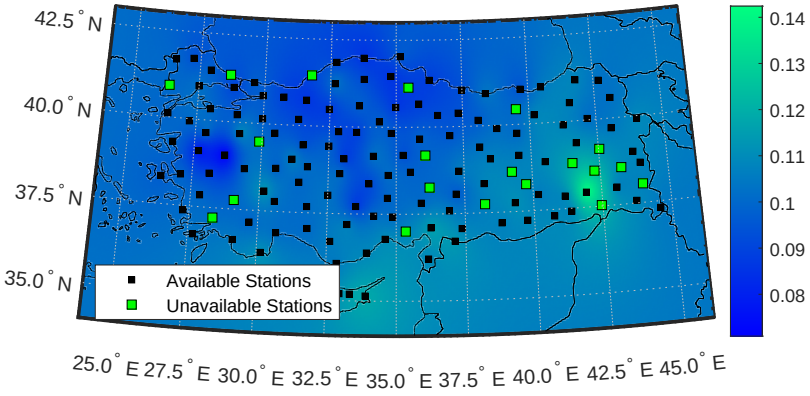

(a)

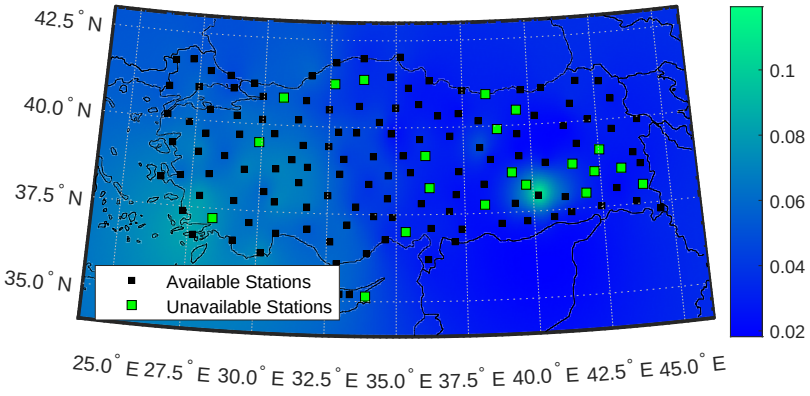

(b)

Figure 2.5: Visualization of TEC reliability signals for two different dates: (a) 29.08.2011 with sunspot number 34 and (b) 30.08.2011. with sunspot number 51.

As presented in Fig. 2.5, Diyarbakır and Bitlis regions of Turkey show higher TEC reliability scores compared to other regions of Turkey. This issue shall be attributed to the fact that these regions are at the border of the Eurasian tectonic plate and Arabian tectonic plate. Therefore, these regions may exhibit frequent seismic activities resulting with higher reliability scores.

In the following, two different earthquake precursor detectors operating on these precursor detection and reliability signals are presented.

2.5 Adaptive Generation of the Anomaly Detection Thresholds

A decision boundary shall be defined as a hyperplane that separates observation space into multiple decision regions [75]. The generated spatio-temporal earthquake precursor detection signals are the observation space of the proposed anomaly detection technique. Hence, anomaly detection thresholds shall separate anomalous TEC variations from the regular TEC variations on the generated earthquake precursor detection signals. These anomaly detection thresholds shall be generated with respect to spatial, temporal or spatio-temporal variations of the generated earthquake precursor detection signals. In this work, spatial earthquake precursor detection thresholds that are constant in time are generated to detect spatial TEC anomalies and temporal earthquake precursor detection thresholds that are constant in space are generated to detect temporal TEC anomalies. Each day classified into two non-overlapping classes named as: "seismic activity" and "no seismic activity" and TEC variation statistics of the days of no seismic activity class are used during the threshold generation process.

2.5.1 Spatial earthquake precursor detection thresholds

Spatial earthquake precursor detection thresholds shall be generated by estimating TEC variation behaviour of each reference station on the days of no seismic activity class [76]. The TEC variation behaviour of each reference station is estimated by negative Pareto cumulative distributions. Each negative Pareto cumulative distribution is unique to a TNPGN reference station and maps each local TEC variation of this reference station to a tail probability. Hence, choosing a constant tail probability corresponds to a different local TEC variation value

for each TNPGN reference station.

Upper truncated Pareto distributions provide appropriate statistical characterization on dense TEC measurements, since the TEC measurement and their generated estimates are positive valued. For an upper-truncated Pareto random variable Z its tail probability is given by the following three parameter model in ρ, γ and ϑ [76, 77]:

$$P(Z > z) = \frac{\gamma^{\rho}(z^{-\rho} \; - \; \vartheta^{-\rho})}{1 \; - \; \left(\frac{\gamma}{\vartheta}\right)^{\rho}} \; , \; 0 < \gamma \leq z \leq \vartheta < \infty \; . \tag{2.15}$$

Maximum Likelihood (ML) estimates for the distribution parameters are:

$$\hat{\gamma} \; = \; \min(TEC_{\Delta;u}(1) \; , \; \cdots \; , \; TEC_{\Delta;u}(N_{ns})) \; , \tag{2.16}$$

$$\hat{\vartheta} \; = \; \max(TEC_{\Delta;u}(1) \; , \; \cdots \; , \; TEC_{\Delta;u}(N_{ns})) \; , \tag{2.17}$$

and $\hat{\rho}$ is obtained as the solution to:

$$\frac{N_{ns}}{\hat{\rho}} \; + \; \frac{N_{ns}\left(\frac{\hat{\gamma}}{\hat{\vartheta}}\right)^{\hat{\rho}} \; \log\left(\frac{\hat{\gamma}}{\hat{\vartheta}}\right)}{1 \; - \; N_{ns}\left(\frac{\hat{\gamma}}{\hat{\vartheta}}\right)^{\hat{\rho}}} \; = \; \sum_{i=1}^{N_{ns}} \left[\log(TEC_{\Delta;u}(i)) \; - \; \log(\hat{\gamma})\right] \; , \tag{2.18}$$

where N_{ns} is number of days with no seismic activity and $TEC_{\Delta;u}(i)$, $0 \leq i \leq N_{ns}$ is a time series of the local TEC variations obtained from the no seismic activity days for the reference station u [76, 77].

$\hat{\gamma}$, $\hat{\vartheta}$ and $\hat{\rho}$ parameters shall be obtained by using (2.16), (2.17) and (2.18), respectively. Thereafter, probabilistic distribution of local TEC variation tail probability, $P_{tail;TEC_{\Delta}}$ shall be estimated for all stations in the TNPGN for seismically inactive days. As an example demonstration of the estimation performance, Three different local TEC variation tail probability distributions are illustrated in Fig. 2.6 for three different reference stations “Fethiye”, “Eskisehir” and “Samsun”.

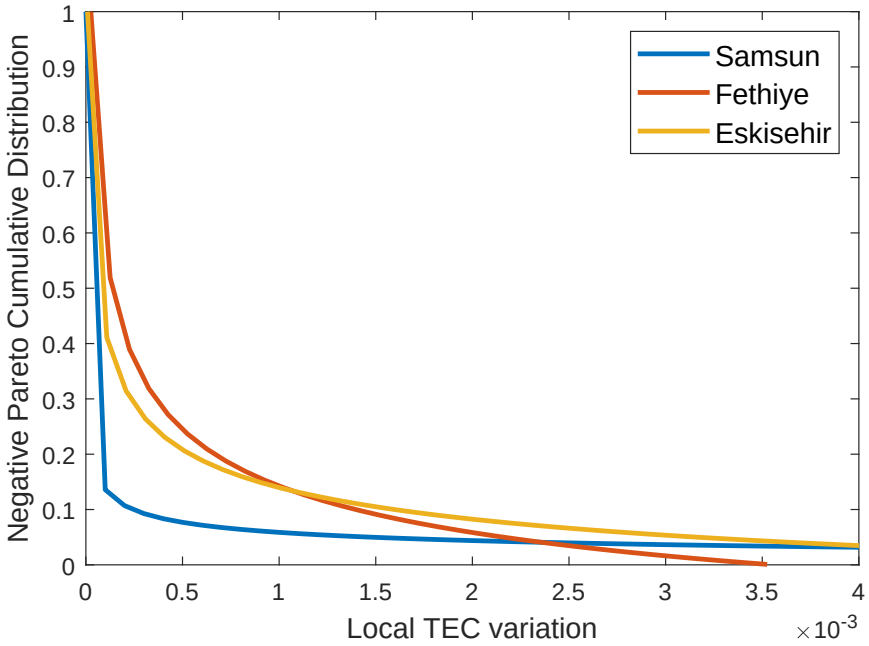

Figure 2.6: Local TEC variation Negative Pareto cumulative distributions for the "Fethiye" (red), "Eskisehir" (orange) and "Samsun" (blue) stations.

As presented in Fig. 2.6, estimated local TEC variation tail probability distributions show spatial variation that distributions vary with respect to the locations of the reference stations. When a constant tail probability is chosen as $P_{tail;TEC_\Delta} = 0.1$, the tail probability corresponds to a different local TEC variation in "Fethiye", "Eskisehir" and "Samsun" reference stations as 0.0013, 0.0015 and 0.0002, respectively. If this procedure is repeated for all TNPGN reference stations and the corresponding local TEC variations are chosen as spatial thresholds, then a spatial earthquake precursor detection threshold that corresponds to the chosen tail probability shall be generated. Three different spatial earthquake precursor detection thresholds are illustrated in Fig. 2.7 for three different TEC variation tail probabilities. Tail probabilities are chosen as 0.05 in Fig. 2.7a, 0.005 in Fig. 2.7b and 0.0005 in Fig. 2.7c.

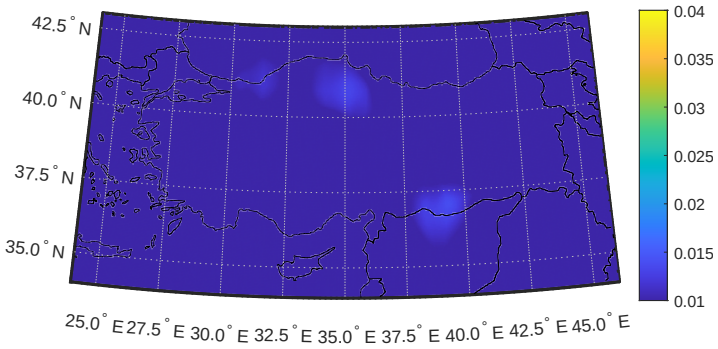

(a)

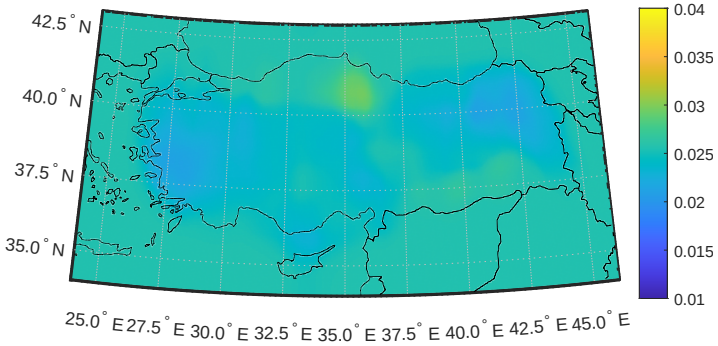

(b)

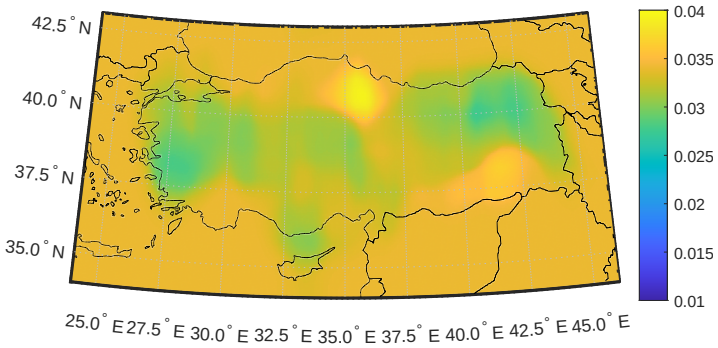

(c)

Figure 2.7: Spatial earthquake precursor detection thresholds with different local TEC variation tail probabilities: (a) 0.05, (b)0.005 and (c) 0.0005.

2.5.2 Temporal earthquake precursor detection thresholds

Temporal earthquake precursor detection thresholds are generated by using all daily local TEC variations $TEC_{\Delta;v;d}$ obtained from all reference stations $v = 1, .., N_s$ where N_s is the number of all stations on TNGPN and d is the chosen day. Let $TEC_{\Delta;d;sort}$ denote the $(N_s \times 1)$ sorted vector containing all local TEC variations for the day d:

$$TEC_{\Delta;d;sort} = f([TEC_{\Delta;1;d} \cdots TEC_{\Delta;v;d} \cdots TEC_{\Delta;N_s;d}]^T), \tag{2.19}$$

where $f(.)$ function is a vector sorting function. Median local TEC variation of the chosen day d, Med_d shall be defined as follows:

$$Med_d = \frac{TEC^{N_s/2}_{\Delta;d;sort} + TEC^{N_s/2+1}_{\Delta;d;sort}}{2} \tag{2.20}$$

where $TEC^{N_s/2}_{\Delta;d;sort}$ is the $N_s/2$'th element of the $TEC_{\Delta;d;sort}$ vector. Similarly, mean M_d and standard deviation S_d of the daily local TEC variations of the day d shall be defined as follows:

$$M_d = \frac{1}{N_s} \sum_{v=1}^{N_s} TEC_{\Delta;v;d} \, , \tag{2.21}$$

$$S_d = \sqrt{\frac{1}{N_s - 1} \sum_{v=1}^{N_s} \left(TEC_{\Delta;v;d} - M_d \right)^2} \, , \tag{2.22}$$

Hence, temporal earthquake precursor detection threshold TET_d for the chosen day d shall be generated by:

$$TET_d(\beta) = Med_d + \beta S_d \, , \tag{2.23}$$

where β parameter is a control parameter that adjusts the expected range of daily TEC variations. Choosing a high β parameter corresponds to increasing the expected daily TEC variations that results with fewer earthquake precursor detections for the day d. On the other hand, choosing a high β parameter will also result with fewer number of false TEC anomaly decisions.

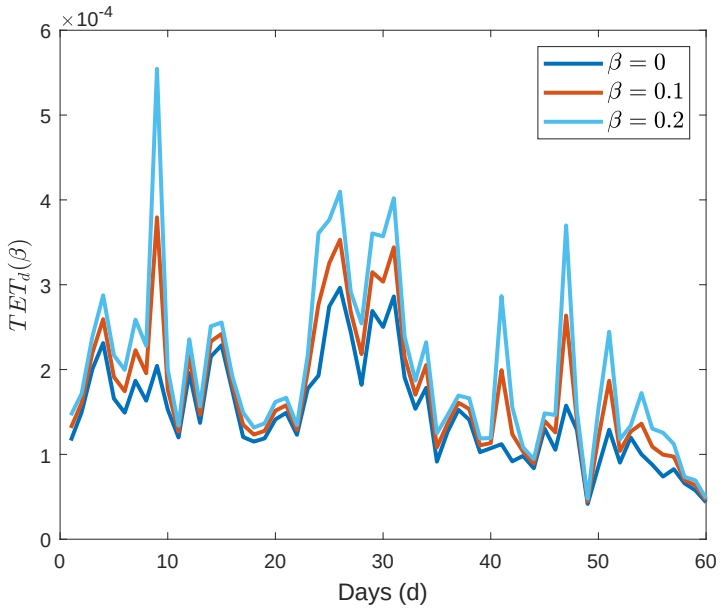

Figure 2.8: Temporal earthquake precursor detection for the first 60 days of 2011 with different β parameters.

Different temporal earthquake precursor detection thresholds are illustrated in Fig. 2.8. The thresholds are generated for the first 60 days of 2011 with three different β parameters chosen as: 0, 0.1 and 0.2. As seen in Fig. 2.8, generated temporal earthquake precursor detection thresholds show temporal variations while remaining constant over space.

2.6 Earthquake Precursor Detectors

Different from the previous research, spatial and temporal earthquake precursor detectors are obtained that can operate on both generated earthquake precursor detection and reliability signals as generation of these signals described in Section 2.3 and Section 2.4 [78]. During the operation, these detectors require detection parameters and the earthquake precursor detection thresholds that are generated based on techniques detailed in Section 2.5. Since spatial and temporal earthquake precursor detectors can declare a precursor decision on the detection signal

with respect to the detection parameters, determining an appropriate set of detector parameters has a significant importance on the performance of earthquake precursor detection technique. In the following, a detector parameters based earthquake precursor classification technique making use of false alarm control of these detectors will be presented.

2.6.1 Control of False Alarm

To demonstrate the false alarm control performance of the proposed detectors, false alarms that are generated by the proposed earthquake precursor detectors are investigated on the days of no seismic activity. For each earthquake presented in Table 2.2, a unique time window is defined for day labeling purposes. Days of seismic activity are labeled with respect to these time windows which start from 9 days prior to an earthquake and end with the day of the related earthquake. Hence, 154 days of 2011 are labeled as seismically active days and belong to seismic activity class. Remaining 211 days in 2011 are labeled as in the no seismic activity class.

Local TEC variation statistics that are obtained from the days of no seismic activity are used to generate spatial earthquake precursor detection thresholds. The relation between the tail probability of local TEC variation $P_{tail;TEC_{\Delta}}$ and probability of false alarm, P_{FA} for the days of no seismic activity class is presented in Fig. 2.9. As shown in Fig. 2.9, a desired level of P_{FA} can be achieved by obtaining the corresponding tail probability. Once a tail probability is chosen, the spatial earthquake precursor detection thresholds can be obtained by using the corresponding Pareto distribution for each reference station.

Unlike the spatial earthquake precursor detection thresholds, temporal earthquake precursor detection thresholds are generated by using the statistics that are obtained from both days of seismic activity and no seismic activity. The relation between the β parameter in (2.23) and P_{FA} for the days of no seismic activity class is also presented in Fig. 2.9. As shown in Fig. 2.9, P_{FA} can be set to a desired level by adjusting β parameter. Once a β parameter is chosen, temporal

earthquake precursor detection thresholds shall be generated by using (2.23).

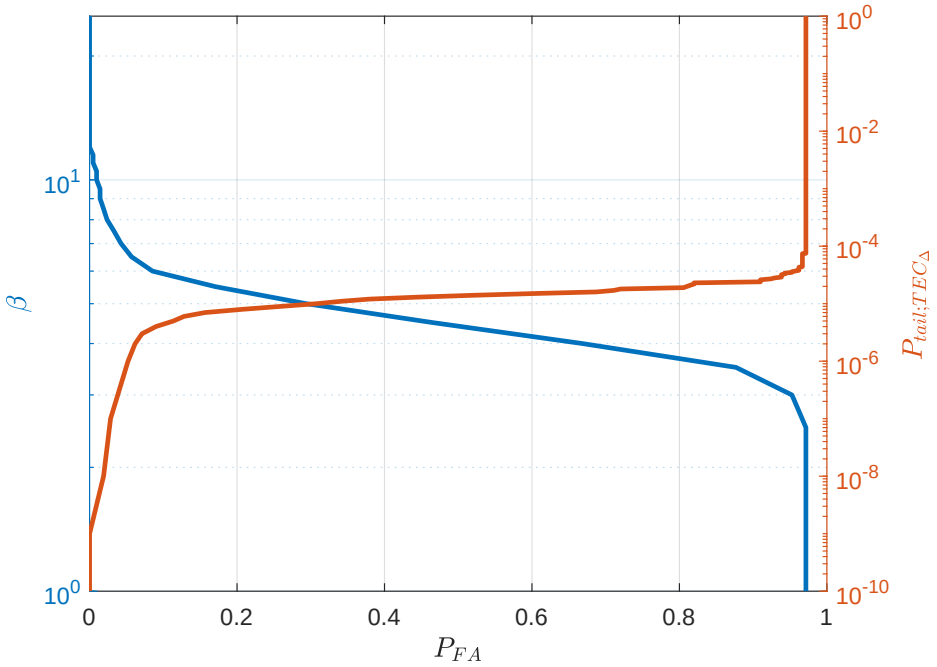

Figure 2.9: (Right)Adjusting Spatial Detector's P_{FA} by adjusting local TEC variation tail probability $P_{tail;TEC_\Delta}$, (Left) Adjusting Temporal Detector's P_{FA} by adjusting β parameter in (2.23).

Spatial and temporal earthquake precursor detectors shall adjust $P_{tail;TEC_\Delta}$ and β parameters to obtain appropriate spatial and temporal earthquake precursor detection thresholds for a desired level of P_{FA}. If spatial or temporal earthquake precursor detection thresholds are exceeded on the generated earthquake precursor detection signal, the detector generates a precursor decision which might be related to an upcoming earthquake. Generated precursor decisions shall be classified with respect to their TEC reliability scores. Decision classification validates precursor decisions with acceptable TEC reliability scores, and rejects remaining precursor decisions. A decision classification technique is detailed in the next section.

2.6.2 Classification of Precursor Decisions

Earthquake precursor detection signals and TEC reliability signals shall be synchronized such that each and every reference station in the TNPGN will have a local TEC variation, $TEC_{\Delta;u;d}$ and TEC reliability score, $TEC_{\alpha;u;d}$ for a chosen day d and reference station u. The synchronized signal represents each TEC measurement in terms of its variation and reliability. Therefore, it is possible to assess each TEC variation with respect to its reliability. In order to distinguish the local TEC variations with respect to their reliability, a linear classifier shall be used. For a chosen reference station u, and day d, a linear classifier shall be defined as:

$$TEC_{\Delta;u;d} \leq g_{LC} \times TEC_{\alpha;u;d} + C_{TEC_{\Delta}}, \tag{2.24}$$

where g_{LC} is gradient of linear classifier and $C_{TEC_{\Delta}}$ is the intersection point of the linear classifier and the TEC variation axis. g_{LC} and $C_{TEC_{\Delta}}$ parameters can be considered as the detector parameter pair for an earthquake precursor detector.

To demonstrate the particular advantage of the proposed linear classifier, precursor decisions generated by a spatial detector for a chosen $P_{FA} = 0.1517$, and the detector parameters ($g_{LC} = -0.25, C_{TEC_{\Delta}} = 0.029$) are illustrated in Fig. 2.10. As shown in Fig. 2.10, the linear classifier may reduce P_{FA} by rejecting 7 precursor decisions that result with false alarms while preserving 20 precursor decisions resulting with true positive precursor detections. Despite the observed performance enhancement may be limited to this particular case, a performance enhancement is not guaranteed with constant detector parameters. Therefore, the detector parameters of both the spatial and the temporal earthquake precursor detectors require tuning for a chosen P_{FA}.

Note that, choosing a linear classifier is also advantageous in terms of computation complexity. In order to choose an univariate quadratic decisions boundary, a 3 dimensional optimization problem should be solved for the equation

$TEC_{\Delta;u;d} \leq a \times TEC^2_{\alpha;u;d} + b \times TEC_{\alpha;u;d} + c$. However, the resulting decision boundary will open through upwards or downwards only that classification accuracy of this decision boundary might be limited. Similarly, proposing a bivariate decision boundary requires solving a 6 dimensional optimization problem that makes the optimization problem difficult. If decision boundaries of both temporal and spatial detectors are simultaneously optimized for univariate and bivariate quadratic decision boundaries, resulting optimization problem will be 6 or 12 dimensional, respectively.

A decision fusion technique with parameter tuning for the individual earthquake precursor detectors will be presented in the following section.

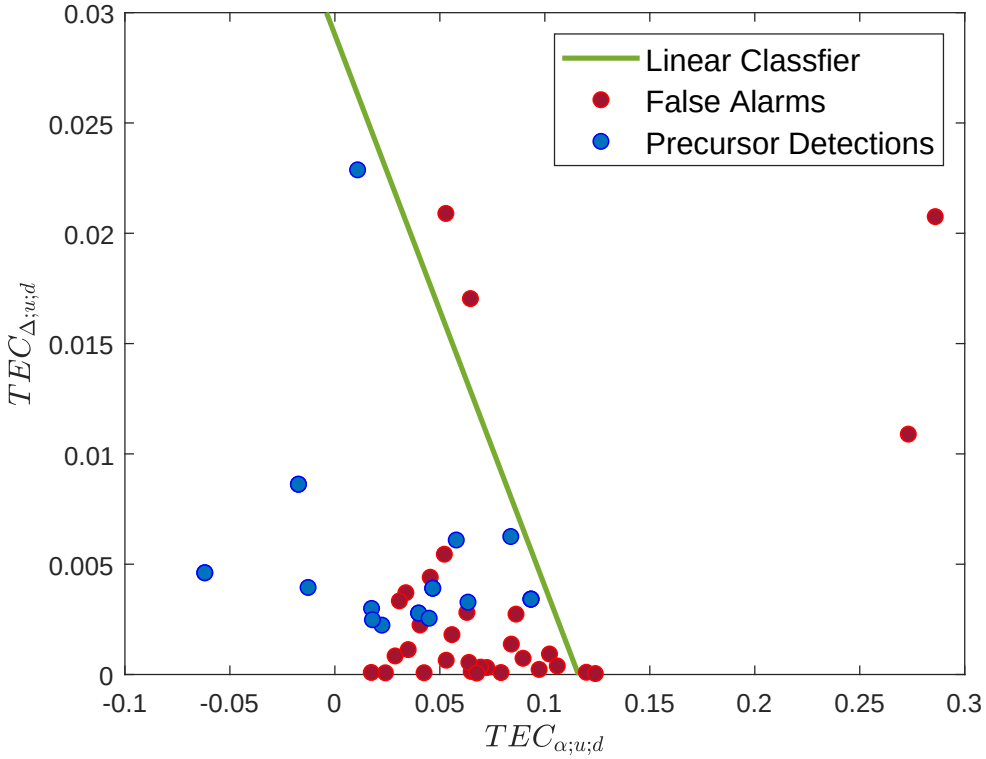

Figure 2.10: Precursor decisions of spatial earthquake precursor detector separated by pre-defined linear classifier parameters.

2.6.3 Decision Fusion Technique

The proposed decision fusion technique is based on generating a fused precursor decision that combines precursor decisions of two or more detectors simultaneously so that the fused precursor decision is more reliable than the individual precursor decisions [79]. Detection performance of the fused precursor decisions is highly dependent on the diversity and the number of the individual decisions. In this work, the earthquake precursor detections generated by dissimilar spatial and temporal detectors. Precursor decisions that are generated by these detectors are combined to form fused earthquake precursor detections for achieving improved performance in terms of fewer false alarms and higher detection rates.

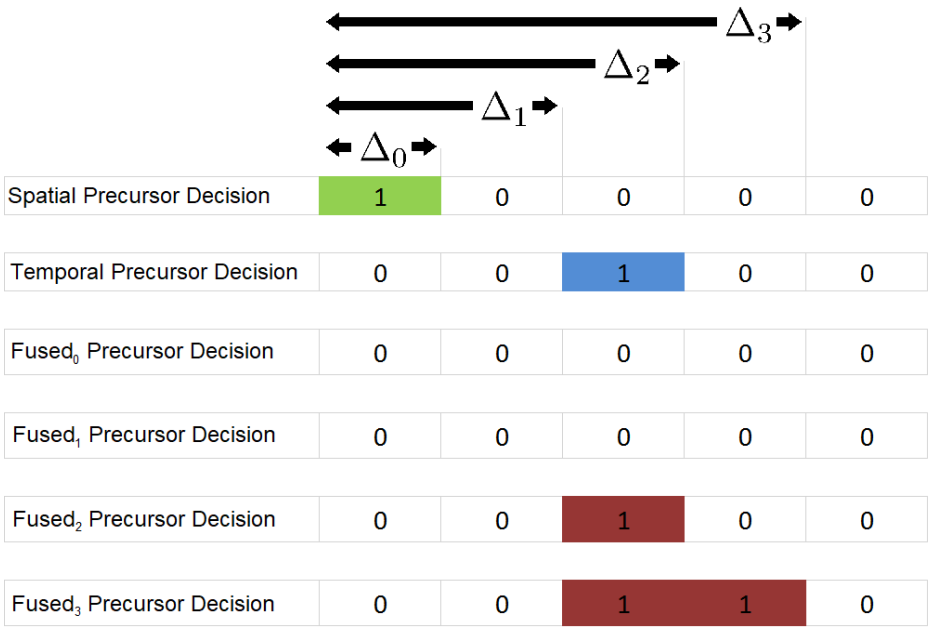

Figure 2.11: Spatial and temporal decision time series for 5 days with fused decision time series for different Δ_d parameters.

Daily earthquake precursor decisions that are generated by spatial and temporal earthquake precursor detectors can be considered as hard decisions. These hard decisions can be grouped into two distinct classes such that the upcoming

earthquake precursor decisions are marked as $1's$ and remaining days without precursor decisions are marked as $0's$. Therefore, the daily earthquake precursor decisions of an earthquake precursor detector can be represented as a time series consisting of only $1's$ and $0's$.

These earthquake precursory decisions can be fused by using two stage of processing. First, precursor decisions that are marked as $1's$ in the decision time series will be echoed for Δ_d days for each decision time series. Thereafter, logical AND operation is applied for the two different echoed decision time series to obtain $Fused_{\Delta_d}$ earthquake precursor decisions. To demonstrate decision fusion technique, two different spatial and temporal decision time series are generated for 5 days and their corresponding $Fused_{\Delta_d}$ decisions are presented as in Fig. 2.11.

For a chosen Δ_d parameter and given P_{FA}, each earthquake precursor detector shall generate hard earthquake precursor decisions without considering the detector parameters and the reliability assessment. As discussed in Section 2.6.2, applying decision classification with detector parameters is a promising performance enhancement, while it requires parameter tuning for the detector parameters. In this work, both spatial and temporal detector parameters are tuned by using Particle Swarm Optimization (PSO) technique [80].

PSO is an iterative optimization technique based on simulating behaviour of moving particles in a parameter search-space with respect to predefined constraints. The technique aims to obtain best parameter set in the search-space represented by a particle beginning from first iteration to last. Detector parameters of spatial detector, $(g_{LC;S}, C_{TEC_\Delta;S})$ and temporal detector, $(g_{LC;T}, C_{TEC_\Delta;T})$ form a 4 dimensional search-space as $(g_{LC;S}, C_{TEC_\Delta;S}, g_{LC;T}, C_{TEC_\Delta;T})$ where performance of each particle in PSO is evaluated subject to this space. Performance of the i'th particle x_i shall be represented as an operation point on a Receiver Operating Characteristic (ROC) space which has the same probability of precursor detection $P_{D;x_i;\Delta_d}$, and probability of false alarm $P_{FA;x_i;\Delta_d}$ as the $Fused_{\Delta_d}$ earthquake precursor decisions shall achieve. Pseudocode of the applied PSO technique is presented in Algorithm 1.

Algorithm 1 Particle Swarm Optimization Pseudocode

// Parameter Definition //
$N_{iter} \leftarrow$ Maximum number of iterations
$N_{particles} \leftarrow$ Number of particles
$P_{FA;MIN} \leftarrow$ Minimum permissible P_{FA} for all particles
$\Delta_d \leftarrow$ Decision Fusion echo parameter

// Initialization //
for `i = (1 to` $N_{particles}$`)` **do**
  $x_i \leftarrow$ initialize the position of the i'th particle
  $v_i \leftarrow$ initialize the velocity of the i'th particle
  $L_{best,i} \leftarrow$ set initial local best of the i'th particle
  if $L_{best,i} > G_{best}$ **then**
    $G_{best} = L_{best,i}$
  end if

end for

// Iterative Optimization //
for `t = (1 to` N_{iter}`)` **do**
  for `i = (1 to` $N_{particles}$`)` **do**
    $v_i \leftarrow$ Update the velocity of the i'th particle
    $x_i(t) = x_i(t-1) + v_i \leftarrow$ Update the position of the i'th particle
    if $P_{D;x_i;\Delta_d} \leq \exp^{-\gamma(P_{FA;x_i;\Delta_d} - P_{FA;MIN})}$ **then**
      if $P_{D;x_i;\Delta_d} > L_{best,i}$ **then**
        $L_{best,i} = P_{D;x_i;\Delta_d}$
        if $L_{best,i} > G_{best}$ **then**
          $G_{best} = L_{best,i}$
        end if

      end if

    end if

  end for

end for

Note that, the detector parameter optimization process shall be divided into 2 parallel optimization techniques such that detector parameters of spatial and temporal detector shall be optimized separately by using 2 separate PSO techniques. However, convergence to the global minima of the 4 dimensional search space is not guaranteed in such a staged optimization process. Despite separate optimization techniques may converge to their respective global minima for 2 dimensional search spaces, combining these 2 dimensional global minima into 4 dimensional solution does not guarantee obtaining a global minima in 4 dimensional search space. Therefore, detector parameters are obtained simultaneously in 4 dimensional space, instead of optimizing these parameters in two separate 2 dimensional search spaces.

Since each particle performance is represented in 2 dimensional ROC space, they can move freely in every direction. To enforce particles to move through directions with lower P_{FA} and higher P_D, movement of the particles can be restricted to a certain P_{FA} range by using ROC-space barrier functions. These barrier functions can put a constraint on the performance of particles in terms of lower probability of false alarms and shall be defined as follows:

$$P_{D;x_i;\Delta_d} \leq \exp^{-\gamma(P_{FA;x_i;\Delta_d} - P_{FA;MIN})}, \tag{2.25}$$

where $P_{FA;MIN}$ is minimum permissible probability of false alarm for all particles and γ is a transition parameter of the barrier function. As shown in Algorithm 1, the barrier function is a constraint for fitness calculation in iterative optimization part. Fig. 2.12, illustrates the barrier functions for different $P_{FA;MIN}$ values. As shown in Fig. 2.12, the ROC-space is limited by barrier functions and detection performance of the particles that are moving outside of this region will not be considered. Since performances of the particles are restricted in the false alarm generation sense, performance of a particle shall be evaluated subject to its probability of detection only.

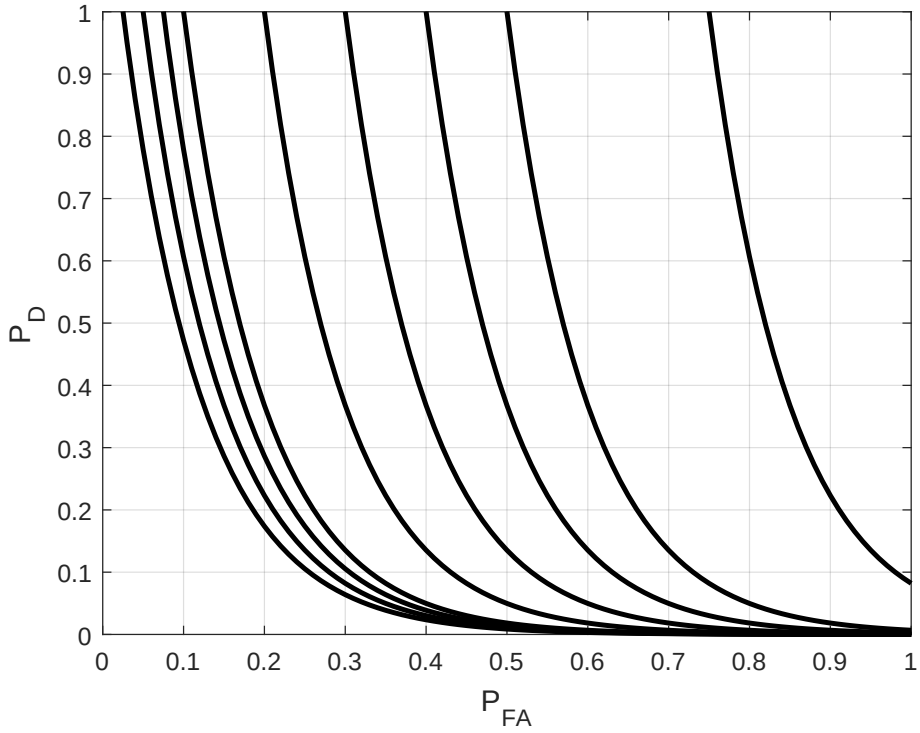

Figure 2.12: ROC barrier functions with $\gamma = 10$ and $P_{FA;MIN} = [0.025, 0.05, 0.075, 0.1, 0.2, 0.3, 0.4, 0.5, 0.75]$ (from left to the right).

In the following performance of the proposed fused earthquake precursor detection technique will be evaluated by fusing the earthquake precursor decisions of the spatial and the temporal earthquake precursor detectors for the days of 2011. Flow diagram of the proposed TEC based earthquake precursor detection technique is presented in Fig. 2.13.

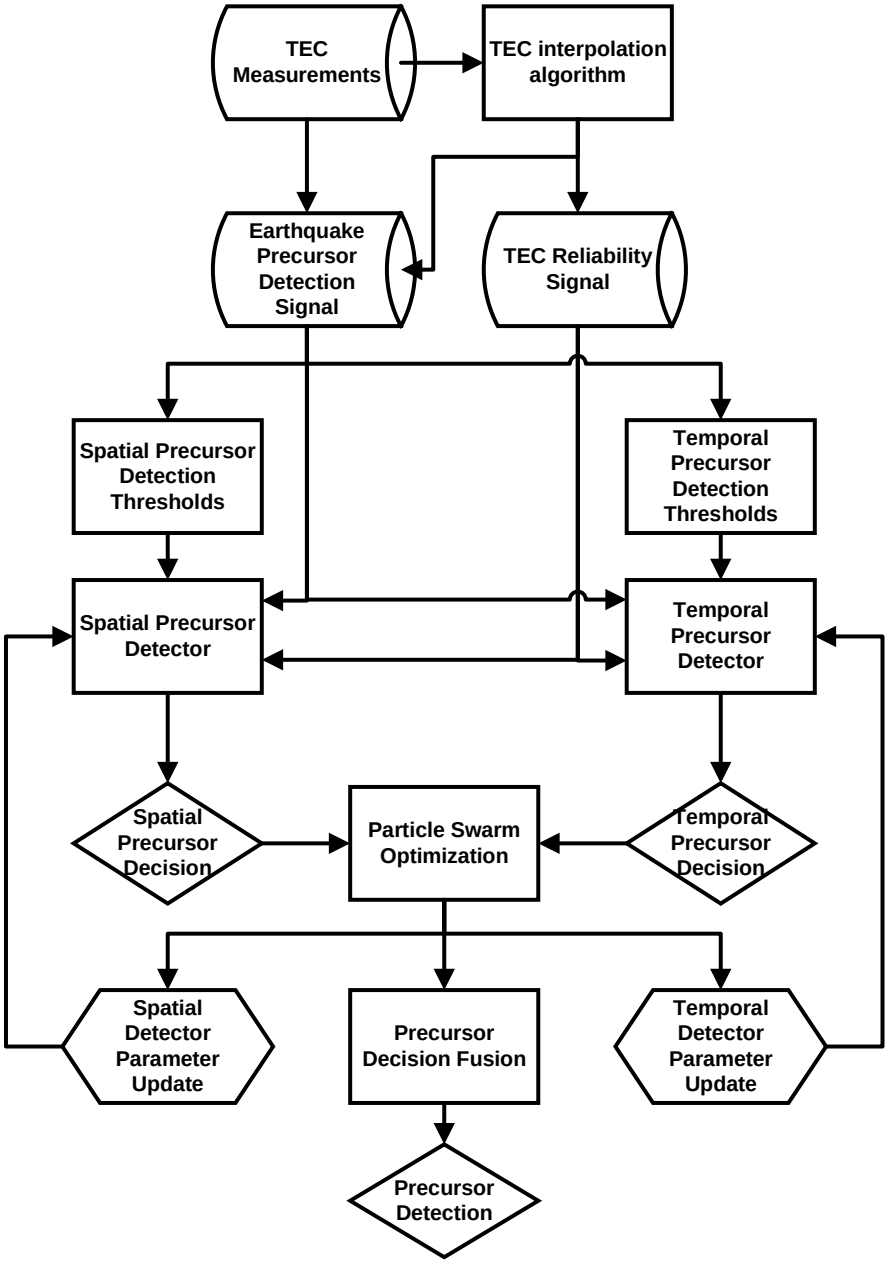

Figure 2.13: Flow diagram of the proposed earthquake precursor detection technique.

2.7 Performance of the Proposed Model Based EQ Detection Technique

Earthquake precursor detection performance of the proposed technique is investigated on the earthquakes that are presented in Table 2.2. As shown in Table 2.2, there are 23 daily different earthquakes that had taken place around Turkey in 2011 with magnitudes greater than 5 in Richter scale. All performance evaluation simulations are performed with respect to seismic activity and no seismic activity classes that are generated from the temporal information obtained from Table 2.2.

Table 2.2: 23 earthquakes that have taken place around Turkey in 2011.

Date	Time	Earthquake Epicenter		Mw	Z
(dd.mm.yyyy)	(hh:mm)	Latitude	Longitude	(Richter)	(km)
19.01.2011	09:17	41.8770	42.7038	5.3	27.81
28.02.2011	07:49	34.7417	25.3913	5.5	25.42
01.04.2011	13:29	35.4819	26.4011	6.2	8.99
19.05.2011	20:15	39.1328	29.0820	5.7	24.46
23.06.2011	07:34	38.5562	39.6307	5.3	13.42
27.06.2011	21:13	39.1108	29.0260	5.0	18.27
25.07.2011	17:57	40.8195	27.7498	5.1	6.97
18.08.2011	14:57	42.3595	43.0042	5.0	15.5
13.09.2011	16:19	34.4090	23.7220	5.0	5.00
14.09.2011	03:35	37.2030	22.0120	5.0	35.05
22.09.2011	03:22	39.6597	38.6777	5.4	7.18
27.09.2011	12:08	34.1700	23.6200	5.2	40.43
10.10.2011	19:07	37.2050	22.0600	5.1	5.00
23.10.2011	10:41	38.6890	43.4657	6.7	19.02
24.10.2011	08:49	38.7060	43.5823	5.0	17.27
25.10.2011	14:55	38.8230	43.5857	5.4	17.44
27.10.2011	08:04	37.3807	43.8343	5.6	21.61
08.11.2011	22:05	38.7192	43.0778	5.4	8.36
09.11.2011	19:23	38.4382	43.2825	5.6	21.47
14.11.2011	22:08	38.7038	43.0833	5.1	23.32
18.11.2011	17:39	38.8022	43.8528	5.2	8.00
23.11.2011	12:18	35.4048	25.9317	5.0	6.96
30.11.2011	00:47	38.4700	43.2905	5.0	19.79

Different earthquake precursor detection signals can be generated by considering the fact that amount of TEC variations changes with respect to the time of the day. Studies report that TEC variations of up to 25% during daytime and 30% during nighttime shall be observed around the earthquake fault zones [81]. Hence, daytime and nighttime ionosphere show distinguishable difference in terms of TEC variations. This difference can be attributed to strong solar radiation that causes high TEC variability in daytime and low TEC variability in nighttime. It is possible to dissociate the local TEC variation $TEC_{\Delta;u;d}$ into different sources of TEC variations as;

$$TEC_{\Delta;u;d} \simeq TEC_{\Delta;solar} + TEC_{\Delta;seismic} + TEC_{\Delta;other}, \tag{2.26}$$

where $TEC_{\Delta;solar}$ is TEC variation triggered by strong solar radiation, $TEC_{\Delta;seismic}$ is TEC variation triggered by seismic activities and $TEC_{\Delta;other}$ is TEC variations with different sources. Due to observed strong solar radiation in daytime, $TEC_{\Delta;solar}$ may attenuate seismic activity triggered TEC variations, $TEC_{\Delta;seismic}$. On the other hand, it might be possible to observe seismic activity triggered TEC variations during the nighttime since disturbing effect of strong solar radiation is less effective during nighttime. Hence, the effect of the strong solar radiation shall be removed from the TEC measurements to investigate seismic activity triggered TEC variations, $TEC_{\Delta;seismic}$ during the nighttime. A TEC measurement window function shall be applied on a chosen TEC measurement to remove the effect of the strong solar radiation from the measurement. An example window is presented in Fig. 2.14c and applied on the TEC measurements that are presented in Fig. 2.2. The windowed TEC measurements are called nighttime TEC measurements and illustrated in Fig. 2.14.

In this work, the daytime and the nighttime earthquake precursor detection signals are generated for all daytime and nighttime daily TEC measurements of all TNPGN stations in 2011. TEC estimates for the daytime and the nighttime TEC measurements are obtained as detailed in Section 2.2. Thereafter, local daytime and nighttime TEC variations are measured by the SKLD metric and earthquake precursor detection signals are generated as discussed in Section 2.3.

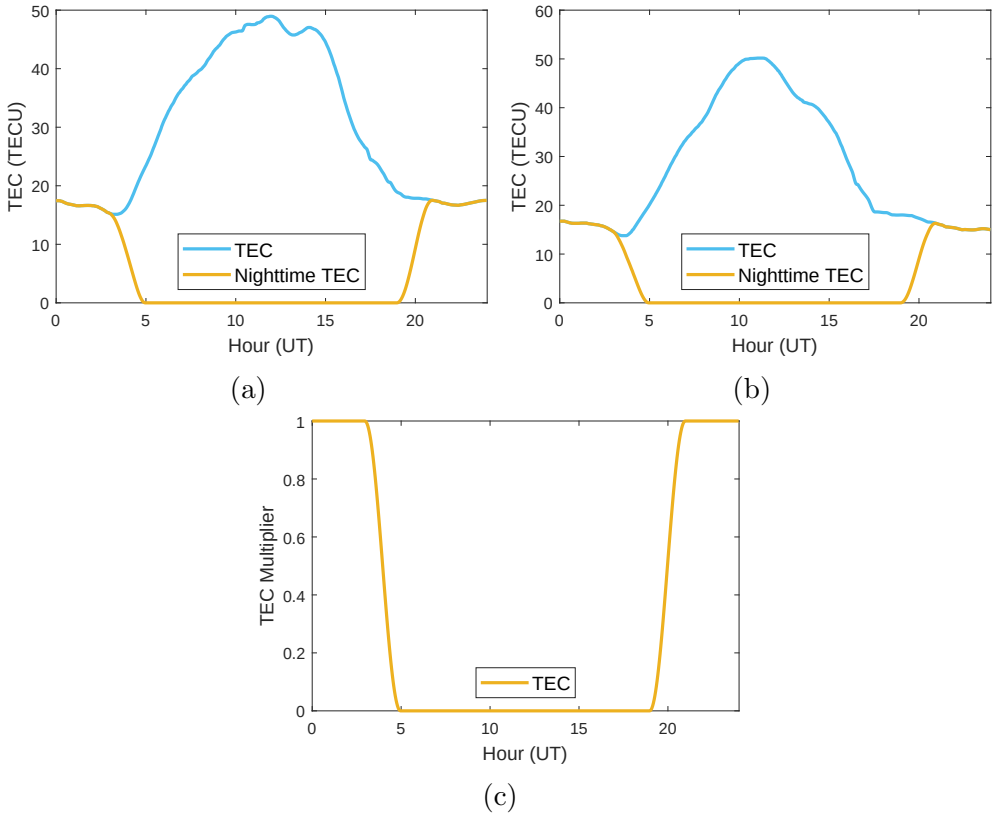

Figure 2.14: The TEC measurements and the nighttime TEC measurements at station "datc" on two different dates: (a) 16.10.2011 and (b) 17.10.2011. (c) TEC measurement window function.

Daytime earthquake reliability signals are generated by using all daytime TEC measurements of all TNPGN stations for the days in 2011. TEC reliability score of each TEC measurement is examined by the maximum value of the estimated local ionosphere variabilities, and earthquake reliability signals are generated as discussed in Section 2.4. Earthquake reliability signals are synchronized with the earthquake precursor detection signals to assess reliability of the local TEC variations during the optimization process in earthquake precursor detectors.

Previous research has revealed that the nighttime earthquake precursor detection signals with temporal earthquake precursor detectors and the daytime earthquake precursor detection signals with spatial earthquake precursor detectors achieve better performance in terms of higher detection rates with fewer false alarm rates [60],[78]. In this work, the temporal earthquake precursor detector

is operated on nighttime precursor detection signals with daytime based reliability signal and the spatial earthquake precursor detector is operated on daytime precursor detection signals with the same daytime reliability signal. Appropriate earthquake precursor detection thresholds are also generated and the spatial and the temporal earthquake precursor decisions are generated based on these thresholds.

Performance of the proposed earthquake precursor detection technique evaluated in terms of $Fused_{\Delta_d}$ precursor decisions that are generated by combining the nighttime temporal earthquake precursor decisions with the daytime spatial earthquake precursor decisions. Fig. 2.15 visualizes the ROC curves for different $Fused_{\Delta_d}$ earthquake precursor decisions. As seen in Fig. 2.15, the $Fused_{\Delta_2}$ earthquake precursor decisions detects 14 earthquake precursors prior to 23 earthquakes and generates 5 false alarms during 211 days of no seismic activity.

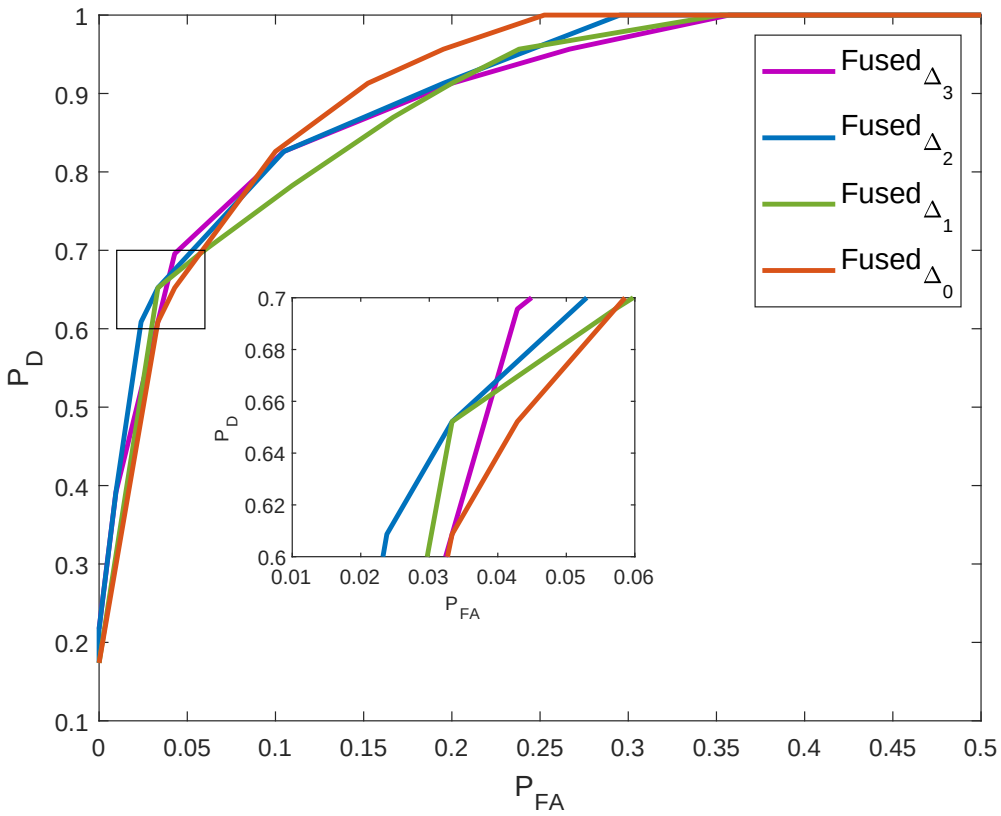

Figure 2.15: (a) ROC curves for $Fused_{\Delta_0}$ (orange), $Fused_{\Delta_1}$ (green), $Fused_{\Delta_2}$ (blue), and $Fused_{\Delta_3}$ (pink) earthquake precursor decisions.

Despite the significant detection performance of $Fused_{\Delta_2}$ precursor decisions, near real-time implementation of the proposed earthquake precursor detection technique might be limited. Therefore, near real-time performance of the proposed should also be evaluated. Cross-validation techniques are widely used to assess the performance of machine-learning based techniques over different data sets [82]. Among the cross-validation techniques, k-fold cross-validation technique is a good candidate to evaluate the near real-time precursor detection performance of the proposed earthquake precursor detection technique. The validation technique is based on training a machine learning model for k times and testing the trained model for k times by partitioning dataset into k small datasets, folds, while reserving a fold for testing and using the remaining folds for training k times.

When the proposed earthquake precursor detection technique is considered, folds are the small partitions of earthquake precursor detection and reliability signals with different time durations. Training phase of the proposed earthquake precursor detection technique can be considered as obtaining best precursor detection threshold pair with their appropriate detector parameters. Test phase performance of the proposed earthquake precursor detection technique can be assessed by using precursor detection thresholds and detector parameters that are obtained in the training phase on chosen test dataset. In this work, 10-fold cross-validation is applied by partitioning earthquake precursor detection and reliability signals into 10 different folds. Each fold contains 36.5 days on the average and number of earthquakes and number of no seismic activity class days are presented in the Fig. 2.16 and also tabulated in first and the second columns of Table 2.4, respectively.

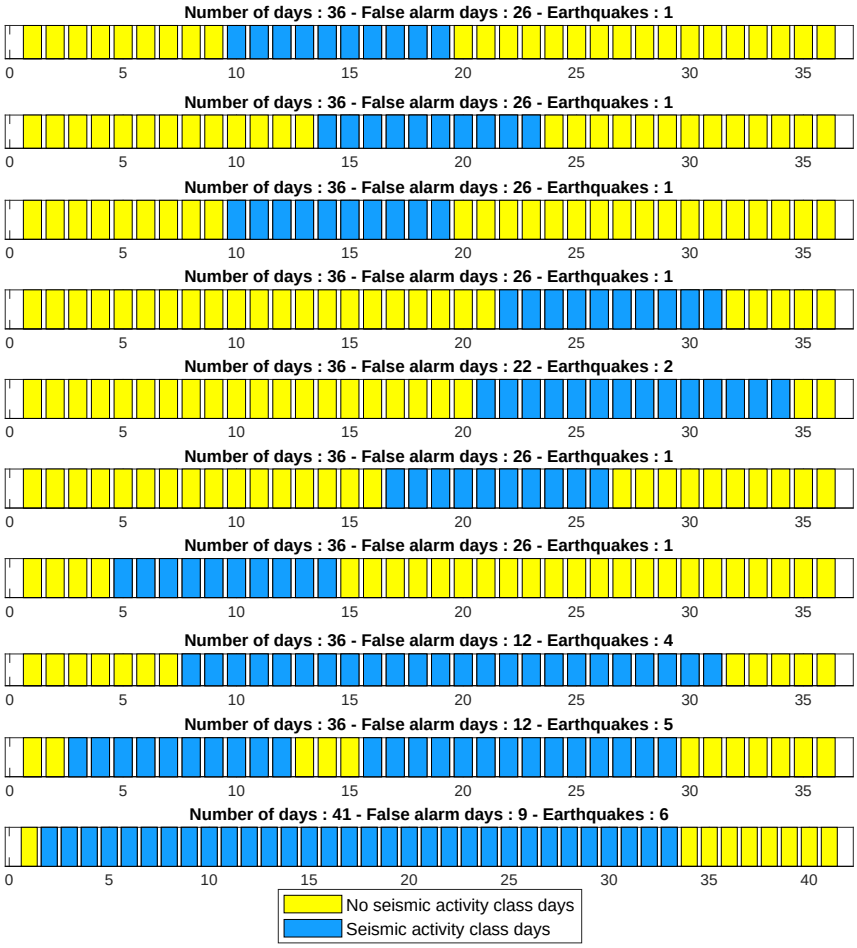

Figure 2.16: 10 different nonintersecting folds generated for the days of 2011 with their seismic activity and no seismic activity class labels. Average number of false alarm days (no seismic activity class days) is around 21.1 and average number of earthquakes is around 2.3 for each fold.

During the training phase of the proposed earthquake precursor detection technique, the proposed technique might memorize earthquake precursor detection and reliability signals such that any variation from this training signals might result with errors in the testing signals. This phenomenon is known as overfitting in machine learning [83]. There are several methods to cope with drawbacks of overfitting problem. One of the widely used solutions for this problem in machine

learning is pruning [84]. Pruning reduces the complexity of the model such that more general implications are imposed on the training dataset. In this work, two different pruning techniques are implemented to prevent the proposed technique from overfitting on earthquake precursor detection and reliability signals. First technique is based on limiting the training ROC operating points of $Fused_{\Delta_d}$ earthquake precursor decisions such that the operating points with a certain false alarm range, $P_{FA;range}$ and a detection range, $P_{D;range}$ are accepted. Another technique is choosing multiple operating points on the training ROC curve to obtain the second and the third best training ROC curves. A fitness function is also used to choose between possible operating points on training ROC curve [85]:

$$fitness(K, D, P_{FA}, P_D) = \frac{1}{K(P_{FA} - 0) \ + \ D(1 - P_D))}, \tag{2.27}$$

where K and D are tradeoff parameters to control the ROC point error penalties in terms of probability of false alarms, P_{FA} and probability of detections, P_D, respectively. To demonstrate near real-time operation performance of the proposed earthquake precursor detection technique, 10-fold cross validation technique is implemented to earthquake precursor detection and reliability signal folds with decision fusion paramater chosen as, $\Delta_d = 3$, barrier function parameters chosen as $\gamma = 20$ and $P_{FA;MIN} = [0.01 : 0.01 : 0.1]$. During the training, the ROC operating points are restricted to $P_{FA;Range} = [0, 0.07]$ and $P_{D;Range} = [0.4, 0.6]$. Table 2.3 illustrates the average training (mean of 10 different training data) and the overall testing performances (cumulative performance of all test folds) of the ROC operation points chosen with respect to (2.27), limited with respect to $P_{FA;Range}$ and $P_{D;Range}$. As shown in the third row of Table 2.3, training and testing performances are reasonably close to each other such that the effect of overfitting is nearly removed with pruning techniques. Individual training and testing performances of the third best $Fused_{\Delta_3}$ earthquake precursor decisions for 10 different folds are also presented in Table 2.4.

Table 2.3: 10-fold cross validation average training and overall testing performances of the first, the second and the third best $Fused_{\Delta_3}$ earthquake precursor decision operation points.

	Average Training Performance		Overall Test Performance	
	P_D	P_{FA}	P_D	P_{FA}
First Best	12.1/20.7	5/189.9	10/23	12/211
Second Best	12/20.7	5.7/189.9	8/23	9/211
Third Best	12/20.7	7.2/189.9	14/23	8/211

Table 2.4: Number of earthquakes and no seismic activity days in each fold. Training and testing performances of third best $Fused_{\Delta_3}$ earthquake precursor decisions for each fold.

Fold Info		Training Performance		Test Performance	
Number of Earthquakes	No Seismic Activity Days	P_{FA}	P_D	P_{FA}	P_D
1	26	6/185	12/22	3/26	0/1
1	26	8/185	13/22	0/26	1/1
1	26	6/185	13/22	1/26	0/1
1	26	7/185	13/22	0/26	1/1
2	22	6/189	12/21	0/22	2/2
1	26	8/185	13/22	2/26	0/1
1	26	9/185	13/22	0/26	1/1
4	12	7/199	11/19	0/12	3/4
5	12	7/199	10/18	2/12	1/5
6	9	8/202	10/17	0/9	5/6

During the training phase of the proposed earthquake precursor detection technique, achieved average probability of false alarm and average probability of precursor detection are 0.0380 and 0.5794 with standard deviations of 0.0057 and 0.0167, respectively. Since these standard deviations are smaller than the

mean values, the proposed earthquake precursor detection technique shall choose a similar operating point each time during the training phase. Furthermore, the proposed earthquake precursor detection technique is achieved average probability of false alarm as 0.0397 and average probability of precursor detection as 0.5783 during the test phase. Unlike the training phase, standard deviation of probability of precursor detection is 0.4657 due to the nonuniform distribution of number of earthquakes for each fold. As shown in the 6'th column of Table 2.4, there is no precursor detections for three folds with only one earthquake, P_D is calculated as zero for these folds. Hence, the calculated standard deviation of probability of precursor detection is high. Standard deviation of probability of false alarm is achieved as 0.0603 during the test phase that is comparably close to the probability of false alarm standard deviation that is achieved during the training phase.

2.8 Concluding Remarks

Geomagnetic activities and strong solar radiation enforces atmospheric gases to lose electrons. Hence, ionosphere is mostly composed of electrically charged particles and free electrons. Studies enlightened a fact that the electron density of the ionosphere is also affected by seismic activities in the Earth's crust and surface.

In this work, a statistically robust earthquake precursor detection based on reliable detection of local ionospheric anomalies is presented and implemented by using TEC data obtained from the Turkish National Permanent GPS Network (TNPGN-Active). Adaptive operation performance of the proposed earthquake precursor detection technique is evaluated without cross-validation and with cross-validation for the 23 earthquakes occurred around Turkey with magnitudes higher than 5 in Richter scale. Precursor detection results of the proposed technique show that the technique shall detect 14 out of 23 earthquake precursors and generate 5 false alarms in direct application. In cross-validated application of the proposed technique, the proposed successfully detected 14 out of 23 earthquake precursors and generated 8 false alarms. Results of the work suggests the

fact that it is possible to implement the proposed earthquake precursor detection technique in near real-time by monitoring local TEC variations in sufficiently dense GPS networks.

For further improvement on the obtained results, position of active faults can be incorporated into both the precursor detection and the reliability analysis is planned as a future work.

Chapter 3

A MACHINE LEARNING BASED EARTHQUAKE PRECURSOR DETECTION TECHNIQUE

To determine the statistical significance of real-time precursor detection of EQs, an investigation had been carried out to obtain precursor detection and false alarm generation performances of a ionospheric TEC based EQ precursor detection technique [60, 61]. Results of these investigations enlighten the fact that there is an interaction between ionospheric TEC anomalies and strong seismic activities. In this study, a machine learning based ionospheric EQ precursor detection technique, EQ-PD is proposed to detect anomalous effects of this interaction on ionospheric TEC. EQ-PD has the following key contributions to the EQ precursor detection literature.

One of the first contributions of the proposed is that EQ-PD generate precursor detections with machine learning techniques. The proposed EQ-PD technique is trained, validated and tested on ionospheric TEC data to generate EQ precursor detections. Hence, it is possible to investigate its precursor detection performance

in a robust and reliable way.

Another contribution of the proposed is that EQ-PD shall work with any chosen GNSS network that shall record daily TEC data on its reference stations. EQ-PD requires daily geomagnetic indices and daily ionospheric TEC data to generate daily EQ precursor decisions.

Final contribution to the literature is that EQ-PD shall be defined as one of the few Boosting techniques in the literature. EQ-PD generates multiple EQ precursor decisions and combines them to get EQ precursor decisions with higher robustness and performances.

In this work, TEC data obtained from reference stations located around Italy with time duration nearly 3 years is processed to evaluate the EQ precursor detection performance of the proposed technique. Obtained TEC data is divided and non-overlapping training, validation and test data sets are generated. EQ precursor detection performance evaluation of the EQ-PD is performed on the test data sets only.

This work consists of multiple sequential processing stages. TEC data processed by the technique is presented in Section 3.1. Generation of the anomaly detection signal, anomaly detection thresholds, anomaly decisions, precursor detection signal and EQ precursor detections are detailed in Section 3.2. Detection performance of the proposed is investigated in Section 3.3. Finally, the work is concluded with concluding remarks and future research directions in Section 3.4.

3.1 Data Collection and Processing

GNSS networks consist of multiple reference stations such that location of these reference stations are estimated and updated with the ionospheric phase delays of the satellite signals [86]. These phase delays are not only used to estimate reference station positions but also used to estimate Slant Total Electron Content

(STEC). STEC shall be defined as total number of electrons encapsulated by a cylinder with 1 m^2 cross section and extends between the satellite and the reference station. A Vertical Total Electron Content (VTEC) or (TEC) estimate shall also be generated by combining all STEC estimates that are obtained from a different satellite [87]. Measurement unit of the estimated TEC shall be defined as TECU and 1 TECU corresponds to 10^{16}electrons/m^2.

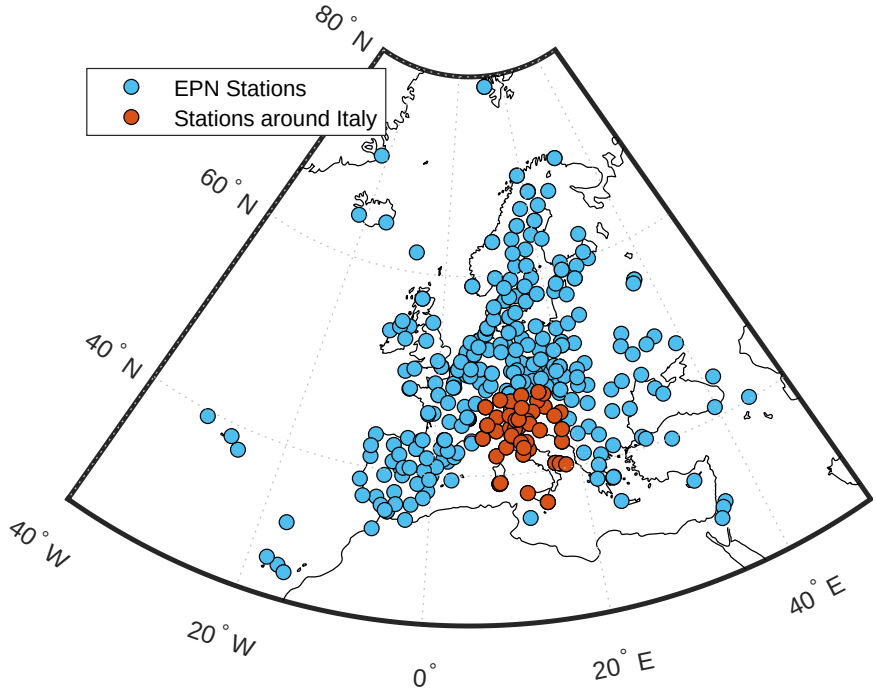

Figure 3.1: Positions of 320 EPN reference stations over Europe including region of choice covering Italy shown with green circles and chosen reference stations with red circles.

TEC data of a reference station shall be monitored by a time separation of 2.5 minutes. TEC data of multiple reference stations or a GNSS network shall also be monitored by generating 2-D TEC maps of a chosen area with the same time separation of 2.5 minutes [88, 89, 64]. Hence, it is possible to constantly and reliably monitor the TEC data of a chosen region, if a GNSS network has already been deployed on the chosen region. In this work, a subset of reference stations of EUREF Permanent GNSS Network (EPN) is chosen for TEC data collection and processing purposes [90]. Chosen reference stations are deployed

around Italy and presented as orange circles in Fig. 3.1.

EPN is a GNSS network and operated by the International Association of Geodesy Regional Reference Frame sub-Commission for Europe (EUREF). More than 100 agencies and universities contribute to the operation EPN with well-defined guidelines and standards [90]. The EPN made up of more than 300 Continuously Operating GNSS Reference Stations (CORS) deployed around Europe. In this work, TEC data of chosen reference stations of EPN is processed by IONOLAB-TEC and IONOLAB-BIAS services to obtain more reliable and refined TEC data.

IONOLAB-TEC provides reliable and accurate GPS-TEC estimates for a chosen GPS reference station [87, 89, 91, 92]. IONOLAB-TEC combines different STEC data obtained from all GPS satellites that are above the horizon limit of the chosen reference station. Thereafter, a vertical TEC is estimated for each GPS satellite and combined to form a final TEC estimate such that multipath effects of the GPS satellite positions are reduced [93]. IONOLAB-BIAS method is implemented for the the STEC estimation process. The method includes differential code biases (DCB) to STEC estimation and reduces noise on the estimations [92].

In this work, temporal and spatial variabilities of TEC measurements are visualized by the chosen reference stations with code names "AQUI" in L'Aquila region, "VEN1" in Venice region, "TORI" in Turin region and "MATE" in Matera region of Italy. Geodetic locations of these chosen reference stations are presented in Table 3.1, and shown in Fig. 3.2. As shown in Fig. 3.2, "AQUI", "VEN1" and "TORI" reference stations are located on seismically active regions and "MATE" reference station is located on a seismically inactive region compared to other reference station locations. Hence, "AQUI", "VEN1" and "TORI" reference stations are chosen to visualize spatial variabilities of TEC measurements on seismically active regions. "MATE" reference station is chosen to visualize temporal variabilities of TEC measurements on seismically inactive region.

Table 3.1: Geodetic locations and regions of chosen reference stations: "AQUI", "VEN1", "TORI" and "MATE".

Station Code	Location		Country	City
Name	Latitude	Longitude		
AQUI	42.37°N	13.35°E	Italy	L'Aquila
VEN1	45.43°N	12.35°E	Italy	Venice
TORI	45.06°N	7.66°E	Italy	Turin
MATE	40.65°N	16.7°E	Italy	Matera

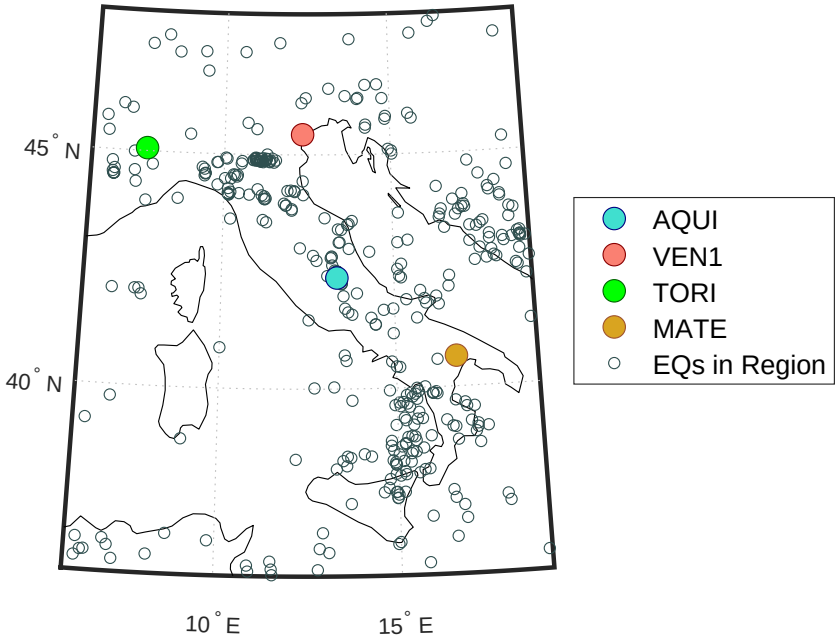

Figure 3.2: Geodetic locations of AQUI, VEN1, TORI and MATE reference stations with recorded EQ epicenters for days in between 2005 and 2016.

Geomagnetic activities disturb multiple regions of ionosphere [94, 95]. Since, geomagnetic activities cause ionospheric disturbances or anomalies, geomagnetic activity related anomalies should be decoupled from the other ionospheric anomalies [96, 97, 98]. Geomagnetic activity and geomagnetic storm related ionospheric disturbances shall be classified by monitoring geomagnetic indices. Widely used

geomagnetic indices shall be listed as: auroral electrojet index (AE), planetary magnetic activity index (A_p), disturbance storm time index (Dst), global geomagnetic storm index (K_p) and sun spot number (SSN) [94, 66, 99]. Hourly, daily, 27 day and yearly averaged AE, A_p, Dst, K_p and SSN shall be accessed via NASA Goddard Space Flight Center OMNIWeb service [100]. Among these geomagnetic indices, Dst and K_p indices are used for identifying geomagnetic storms, SSN is used for estimating amount of solar radiation, AE is used for measuring auroral zone magnetic activity and A_p indices is used for measuring average geomagnetic activity.

In this work, temporal TEC variability is presented with TEC data obtained from "MATE" reference station for two different dates: 11 February 2016 and 12 February 2016. The TEC data is visualized in 3.4. As shown in 3.4, two daily consecutive TEC measurements of a reference station show observable temporal differences. Daily geomagnetic indices of these days are also tabulated in Table 3.2.

Table 3.2: For two different dates: 11 February 2016 and 12 February 2016, daily AE, A_p, Dst, K_p and SSN.

Date (D Month YYYY)	AE	A_p	Dst (nT)	K_p (nT)	SSN (nT)
11 February 2016	268	8	-19	20	85
12 February 2016	176	12	-11	27	63

EQ related data is accessed via Advanced National Seismic System's comprehensive earthquake catalog (ANSS ComCat) [101]. Accessed EQ related data: daily different EQ number and EQ date (first column), EQ time (second column), EQ epicenter (third and fourth columns) and EQ magnitude type (fifth column) is presented in Table 3.7.

3.2 Machine Learning based Earthquake Precursor Detection Technique : EQ-PD

GNSS networks constantly and reliably collect ionosphere related data such as TEC, foF2 and hmF2. The collected data shows anomalies before the strong seismic activities that these anomalies shall be defined as EQ precursors if they are detected prior to the EQs [102]. In this work, ionospheric TEC and machine learning based EQ precursor detection technique, EQ-PD is proposed. The proposed shall detect EQ precursors in a daily basis by using the daily TEC data that is collected from spatially distributed reference stations or from a GNSS network.

The collected TEC data exhibit both spatial and temporal TEC variations. Hence, detection of seismic activity triggered TEC anomalies or EQ precursors requires a precursor detection technique that shall learn and detect spatial and temporal TEC variations in TEC data, simultaneously.

This work is organized as follows. In Section 3.2.1, TEC estimation performance result of a spatio-temporal TEC interpolation technique is presented. In Section 3.2.2, spatial and temporally varying anomaly detection signals are generated. Then, anomaly detection thresholds that shall adapt to these spatial and temporal variations are generated in Section 3.2.3. In Section 3.2.4, anomaly decisions are obtained by thresholding anomaly detection signals and obtained anomaly decisions are combined to form an EQ precursor detection signal. Support Vector Machine (SVM) classifiers are trained, validated and tested on the EQ precursor detection signals and finally, EQ precursor detections are generated as discussed in Section 3.2.5. Flow diagram of the proposed EQ-PD technique is visualized in Fig. 3.3.

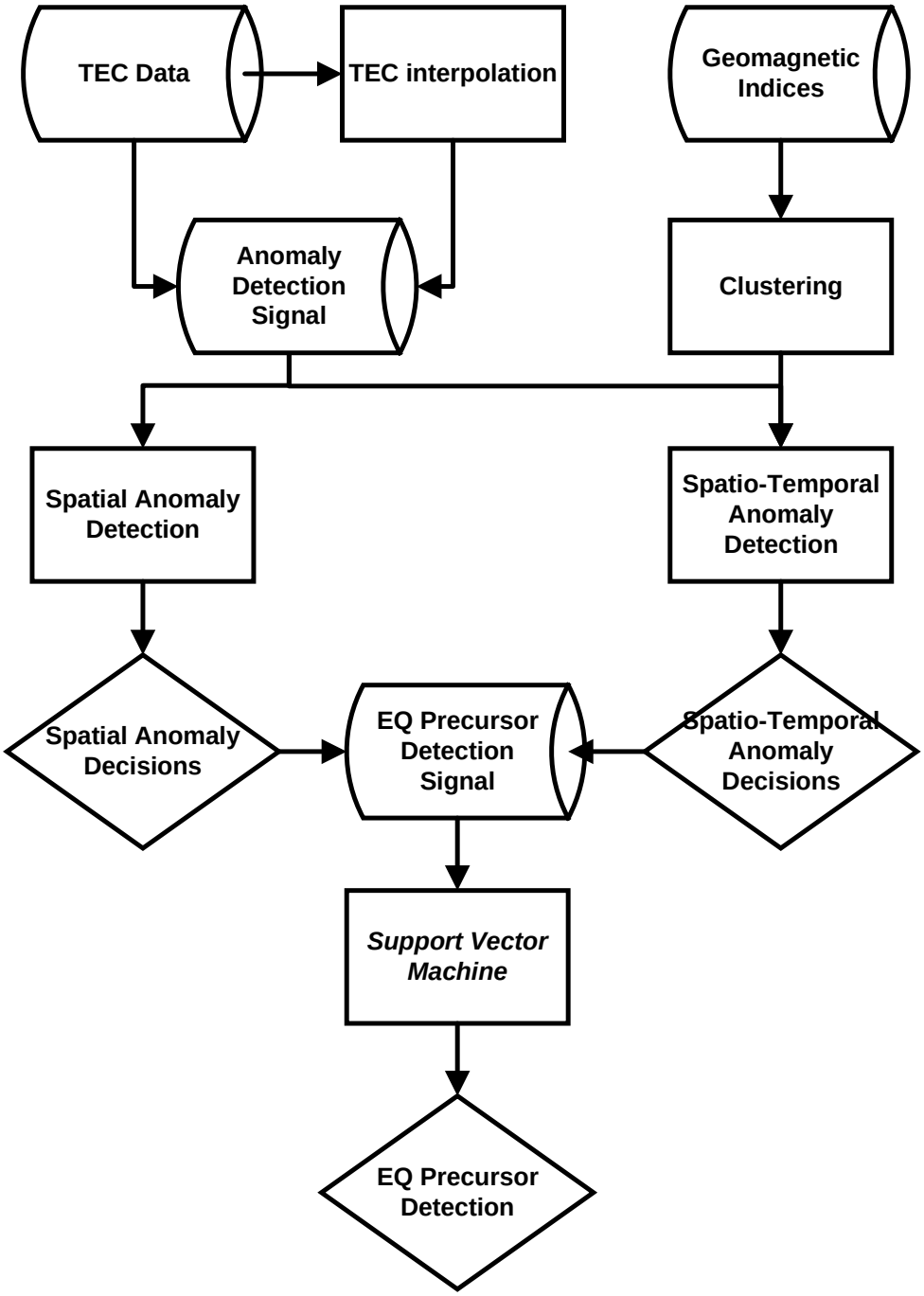

Figure 3.3: Flow diagram of the proposed EQ-PD technique. Detection signals are generated based on regional TEC data and detection thresholds are adaptively chosen based on the geomagnetic indices.

3.2.1 Spatio-Temporal TEC Interpolation

As discussed in Section 2.2, it is possible to obtain a TEC estimate, $\hat{\mathbf{x}}_{u;d;R_r}$ for the TEC measurement of $\mathbf{x}_{u;d}$ by using the neighbouring reference station weight vector $\underline{\boldsymbol{\alpha}}_{u;d_n;R_r}$ in (2.2). Similarity between the obtained TEC estimate, $\hat{\mathbf{x}}_{u;d;R_r}$ and TEC measurement shall be $\mathbf{x}_{u;d}$ measured to generate local TEC variation for the day d and reference station u. TEC estimates, $\hat{\mathbf{x}}_{u;d;R_r}$ and TEC measurements, $\mathbf{x}_{u;d}$ of "MATE" reference station for the chosen dates in Table 3.2 are visualized in Fig. 3.4.

As illustrated in Fig. 3.4, amount of TEC variations show distinguishable differences during daytime and during nighttime. TEC variability sources shall be separated into different categories such as:

$$TECV_{u;d} \simeq TECV_{geo;u;d} + TECV_{seis;u;d} + TECV_{oth;u;d}, \tag{3.1}$$

where $TECV_{u;d}$ is the TEC variability of a reference station u for day d. For the chosen reference station and time, $TECV_{geo;u;d}$ shall be defined as the TEC variability source generated by geomagnetic activities. Similarly, $TECV_{seis;u;d}$ shall be defined as the TEC variability source generated by ongoing seismic activities on the earth's crust. Finally, $TECV_{oth;u;d}$ is the TEC variability source generated by other sources of interactions between ionosphere and space weather. Due to strong solar activity during daytime, $TECV_{geo;u;d}$ shows higher TEC variabilities during daytime compared to the nighttime. However, amount of TEC variability caused by $TECV_{seis;u;d}$ depends on the magnitude of the seismic activity and independent from the time of the day. Therefore, detection of nighttime TEC variabilities caused by $TECV_{seis;u;d}$ shall be easier compared to daytime TEC variabilities due to the absence of $TECV_{geo;u;d}$ during nighttime. The TEC variation window that is presented in Fig. 2.14c shall be applied on the TEC measurements, $\mathbf{x}_{u;d}$ to generate nighttime TEC measurements, $\mathbf{x}^{\text{night}}_{u;d}$. Similarly, nighttime TEC estimates, $\hat{\mathbf{x}}^{\text{night}}_{u;d;R_r}$ shall also be generated with the spatio-temporal estimation technique as presented in Section 2.2. Nighttime TEC estimates, $\hat{\mathbf{x}}^{\text{night}}_{u;d;R_r}$ and

TEC measurements, $\mathbf{x}_{u;d}^{\text{night}}$ of "MATE" reference station for the chosen dates in Table 3.2 are visualized in Fig. 3.5.

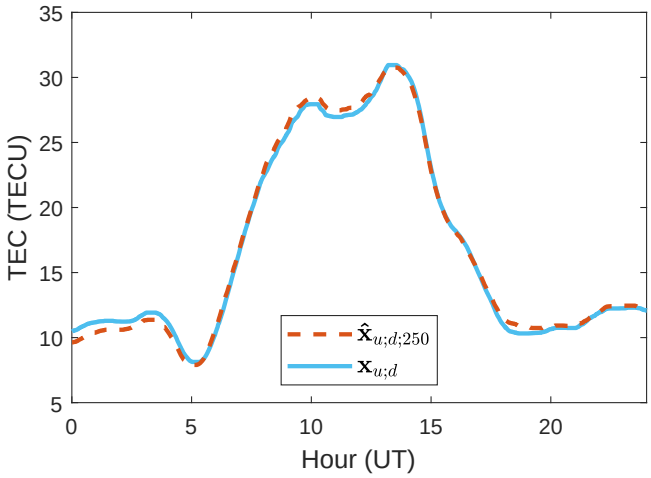

(a)

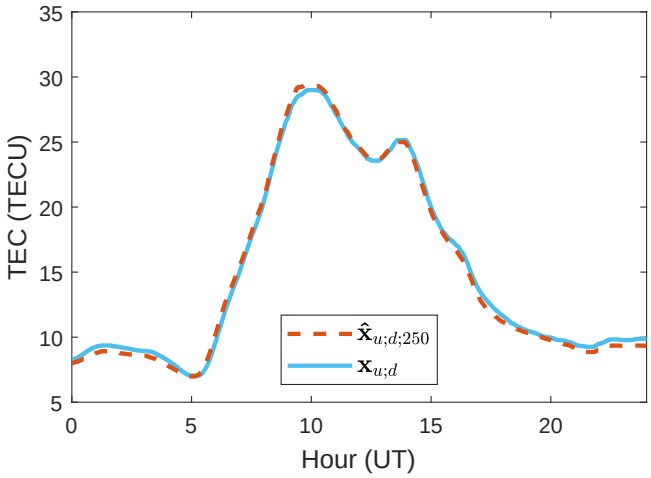

(b)

Figure 3.4: Daily TEC estimates $\hat{\mathbf{x}}_{u;d;R_r}$ and TEC measurements $\mathbf{x}_{u;d}$ for reference station "MATE" for (a) 11 February 2016 and (b) 12 February 2016.

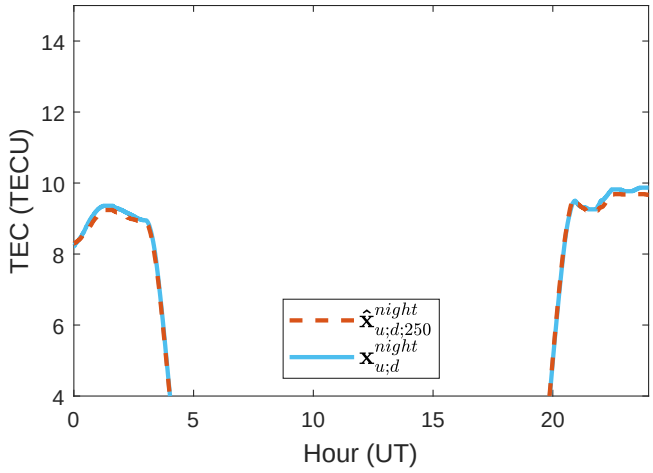

(a)

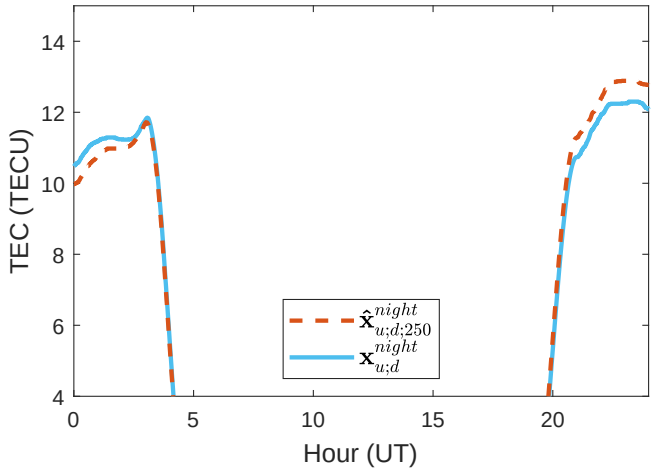

(b)

Figure 3.5: Nighttime TEC estimates $\hat{\mathbf{x}}^{\text{night}}_{u;d;R_r}$ and TEC measurements $\mathbf{x}^{\text{night}}_{u;d}$ for reference station "MATE" for (a) 11 February 2016 and (b) 12 February 2016.

3.2.2 Generation of Whole-day and Night-time Anomaly Detection Signals

Detection of ionospheric TEC related anomalies requires generation of anomaly detection signals. Anomaly detection signals shall be generated by measuring the distance between TEC measurements of all reference stations with their TEC estimates. Symmetric Kullback-Leibler Divergence (SKLD) shall be used as an

appropriate metric to measure the metric distance between TEC estimates $\hat{\mathbf{x}}_{u;d;R_r}$ and TEC measurements $\mathbf{x}_{u;d}$ as also detailed in Section 2.3 [68, 69, 103, 104]. For a reference station u and day d, SKLD based whole-day TEC variation, $TEC_{\Delta}^{\text{w-day}}$ shall be defined as follows:

$$TEC_{\Delta}^{\text{w-day}} = KLD(\hat{\mathbf{P}}_{u;d;R_r}|\mathbf{P}_{u;d}) + KLD(\mathbf{P}_{u;d}|\hat{\mathbf{P}}_{u;d;R_r}), \tag{3.2}$$

where KLD is the abbreviation of Kullback-Leibler Divergence and defined as:

$$KLD(\hat{\mathbf{P}}_{u;d;R_r}|\mathbf{P}_{u;d}) = \left(\sum_{n=1}^{N_{u;d}} \hat{P}_{u;d;R_r}(n) \log\left(\frac{\hat{P}_{u;d;R_r}(n)}{P_{u;d}(n)}\right)\right), \tag{3.3}$$

$$KLD(\mathbf{P}_{u;d}|\hat{\mathbf{P}}_{u;d;R_r}) = \left(\sum_{n=1}^{N_{u;d}} P_{u;d}(n) \log\left(\frac{P_{u;d}(n)}{\hat{P}_{u;d;R_r}(n)}\right)\right), \tag{3.4}$$

where $\mathbf{P}_{u;d}$ ($(N_{u;d} \times 1)$ column vector) is the daily normalized TEC measurement vector and $\hat{\mathbf{P}}_{u;d;R_r}$ ($(N_{u;d} \times 1)$ column vector) is the daily normalized TEC estimate vector. $\mathbf{P}_{u;d}$ and $\hat{\mathbf{P}}_{u;d;R_r}$ shall be defined as follows:

$$\mathbf{P}_{u;d} = \frac{\mathbf{x}_{u;d}}{\|\mathbf{x}_{u;d}\|_1} = \mathbf{x}_{u;d}\left(\sum_{n=1}^{N_{u;d}} x_{u;d}(n)\right)^{-1}, \tag{3.5}$$

$$\hat{\mathbf{P}}_{u;d;R_r} = \frac{\hat{\mathbf{x}}_{u;d;R_r}}{\|\hat{\mathbf{x}}_{u;d;R_r}\|_1} = \hat{\mathbf{x}}_{u;d;R_r}\left(\sum_{n=1}^{N_{u;d}} \hat{x}_{u;d;R_r}(n)\right)^{-1}. \tag{3.6}$$

Note that both $\mathbf{P}_{u;d}$ and $\hat{\mathbf{P}}_{u;d;R_r}$ vectors are unitless since TECU are normalized in (3.5) and (3.6). Similarly, SKLD based nighttime TEC variation, $TEC_{\Delta}^{\text{night}}$ shall be defined as follows:

$$TEC_{\Delta}^{\text{night}} = KLD(\hat{\mathbf{P}}_{u;d;R_r}^{\text{night}}|\mathbf{P}_{u;d}^{\text{night}}) + KLD(\mathbf{P}_{u;d}^{\text{night}}|\hat{\mathbf{P}}_{u;d;R_r}^{\text{night}}), \tag{3.7}$$

where $\mathbf{P}_{u;d}^{\text{night}}$ is the nighttime normalized TEC measurement vector and $\hat{\mathbf{P}}_{u;d;R_r}^{\text{night}}$ is the nighttime normalized TEC estimate vector. $\mathbf{P}_{u;d}^{\text{night}}$ and $\hat{\mathbf{P}}_{u;d;R_r}^{\text{night}}$ shall be defined as follows:

$$\mathbf{P}_{u;d}^{\text{night}} = \frac{\mathbf{x}_{u;d}^{\text{night}}}{\|\mathbf{x}_{u;d}^{\text{night}}\|_1} = \mathbf{x}_{u;d}^{\text{night}}\left(\sum_{n=1}^{N_{u;d}} x_{u;d}^{\text{night}}(n)\right)^{-1}, \tag{3.8}$$

$$\hat{\mathbf{P}}^{\text{night}}_{u;d;R_r} = \frac{\hat{\mathbf{x}}^{\text{night}}_{u;d;R_r}}{\|\hat{\mathbf{x}}^{\text{night}}_{u;d;R_r}\|_1} = \hat{\mathbf{x}}^{\text{night}}_{u;d;R_r} \left(\sum_{n=1}^{N_{u;d}} \hat{x}^{\text{night}}_{u;d;R_r}(n) \right)^{-1}. \tag{3.9}$$

Both whole-day and nighttime anomaly detection signals shall be visualized by kriging interpolation of all $TEC_{\Delta}^{\text{w-day}}$ and $TEC_{\Delta}^{\text{night}}$ for the chosen reference stations presented in Fig. 3.1 and for a chosen date d [70, 71]. For the two consecutive dates presented in Table 3.2, whole-day anomaly detection signals are generated and visualized in Fig. 3.6. As shown in Fig. 3.6, generated whole-day anomaly detection signals show spatial and temporal differences.

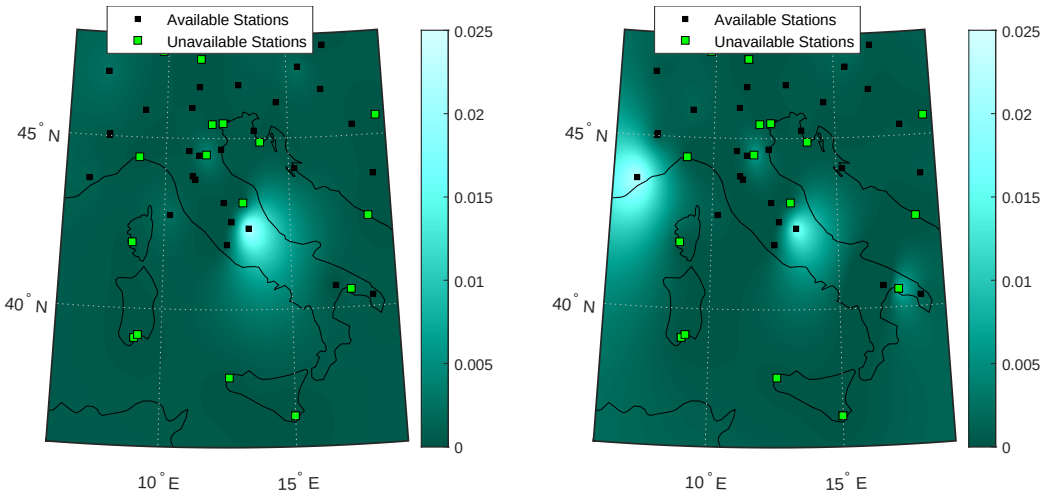

Figure 3.6: Whole-day anomaly detection signals for the chosen reference stations in Fig. 3.1 for (a) 11 February 2016 and (b) 12 February 2016. Reference stations with available $TEC_{\Delta}^{\text{w-day}}$ are marked as black squares and reference stations without a $TEC_{\Delta}^{\text{w-day}}$ are marked as green squares.

3.2.3 Adaptive Generation of the Anomaly Detection Thresholds

Ionospheric local TEC variations shall be detected by using anomaly detection thresholds. These anomaly detection thresholds shall be generated by using past

TEC variation statistics that shall be obtained from past anomaly detection signals. Days of anomaly detection signals are divided into three non-overlapping time intervals named as: training, validation and test set of days. Past TEC variation statistics are generated by using the anomaly detection signals of training and validation sets of days. Anomaly detection signal with test set of dates is reserved for the performance evaluation of the proposed EQ-PD technique which uses TEC variation statistics obtained from training and validation sets of days. After, the TEC variation statistics are obtained, anomaly detection thresholds shall be generated and applied to detect anomalies behaviours in observed $TEC_{\Delta}^{\text{w-day}}$ and $TEC_{\Delta}^{\text{night}}$ in (3.2) and (3.7), respectively.

As presented in Fig. 3.6, TEC anomaly detection signals vary in both space and time. Hence, it is possible to threshold temporal variations, spatial variations or both spatial and temporal variations of the anomaly detection signals. In this study, spatial anomaly detection thresholds that are constant in time are generated to detect spatially varying TEC anomalies and spatio-temporal anomaly detection thresholds are generated to detect both spatially and temporally varying TEC anomalies. The anomaly detection signals of training and validation sets of days are further divided into two non-overlapping sub-classes named as: days with seismic activity and days with no-seismic activity. The TEC variation statistics are obtained from the training and validation days with no-seismic activity.

3.2.3.1 Spatial anomaly detection thresholds

As discussed in Section 2.5.1, it is possible to generate spatial anomaly detection thresholds by modelling TEC variation behaviour for each reference station in a chosen region. The TEC variation behaviour of each reference station shall be estimated by an unique negative Pareto cumulative distribution. Each negative Pareto cumulative distribution maps each local TEC variation of its related reference station to a tail probability. Upper-truncated Pareto negative cumulative distributions shall be modelled by estimating $\hat{\gamma}$, $\hat{\vartheta}$ and $\hat{\rho}$ parameters by using (2.16), (2.17) and (2.18), respectively.

It is also possible to estimate the Pareto cumulative distribution for a chosen reference station by using these distribution parameters. The estimated distribution represents conditional probability of TEC_{Δ} given a chosen reference station in a chosen region and seismically inactive days during a chosen time interval. For the three chosen reference stations: AQUI, TORI and VEN1 located in the region presented in Fig. 3.1 and time interval in between 2005 and 2016, estimated upper-truncated Pareto negative cumulative distributions of $TEC_{\Delta}^{\text{w-day}}$ are presented in Fig. 3.7a. As presented in Fig. 3.7a, a chosen TEC variation tail probability of 0.1 corresponds to different spatial threshold values of 0.015, 0.012 and 0.003 at the reference stations AQUI, TORI and VEN1, respectively. Furthermore, the same estimation procedure shall be repeated for the night-time local TEC variations, $TEC_{\Delta}^{\text{night}}$.

For the TORI reference station and the same time interval as in Fig. 3.7a, estimated upper-truncated Pareto negative cumulative distributions of $TEC_{\Delta}^{\text{w-day}}$ and $TEC_{\Delta}^{\text{night}}$ are presented in Fig. 3.7b. As illustrated in Fig. 3.7b, different negative Pareto cumulative distributions are estimated for whole day and night-time local TEC variations of the same reference station.

For each EPN reference station in the chosen area an upper-truncated Pareto negative cumulative distribution shall be estimated. For a chosen tail probability, a local TEC variation TEC_{Δ} shall also be obtained for each reference station of interest. A spatial anomaly detection threshold is formed by selecting all the chosen local TEC variations as thresholds. Two whole-day spatial anomaly detection thresholds are generated by choosing $TEC_{\Delta}^{\text{w-day}}$ tail probabilities of 0.005 and 0.05. The generated thresholds are presented in Fig. 3.8a and Fig. 3.8b, respectively. As illustrated in Fig. 3.8a and Fig. 3.8b, as the chosen tail probabilities get smaller, resulting local TEC variations get higher. Additionally, changing the tail probabilities result with spatial anomaly detection thresholds with different spatial characteristics.

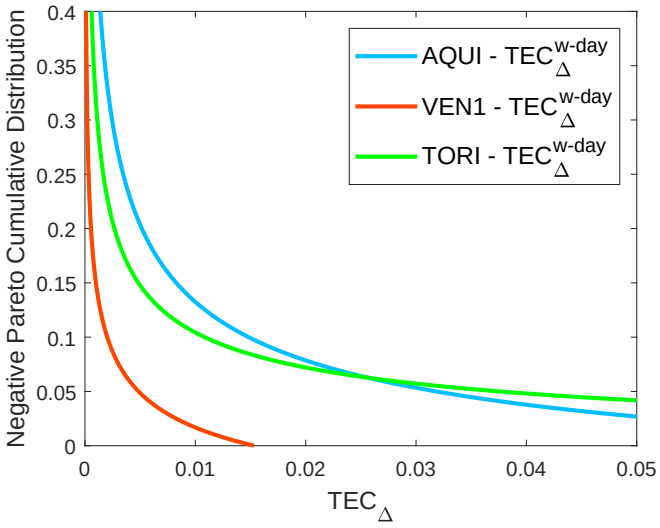

(a)

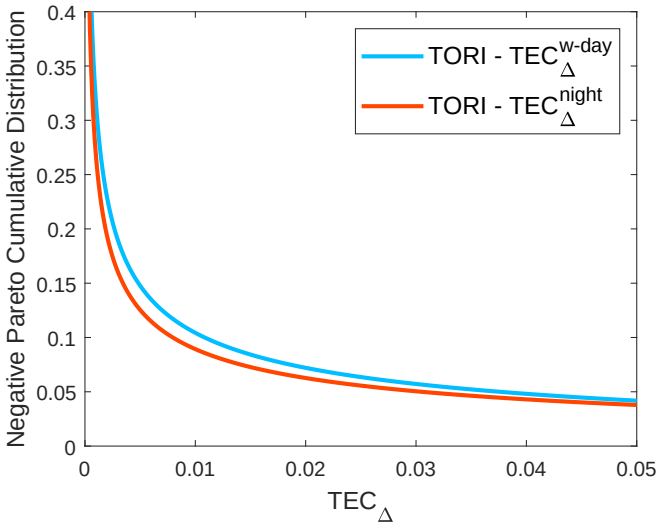

(b)

Figure 3.7: (a) Negative Pareto cumulative distributions of local TEC variations of AQUI, VEN1 and TORI reference stations for the days in between 2005 and 2016. (b) Whole day $TEC_{\Delta}^{\text{w-day}}$ and night-time $TEC_{\Delta}^{\text{night}}$ negative Pareto cumulative distributions of local TEC variations of TORI reference station for the days in between 2005 and 2016.

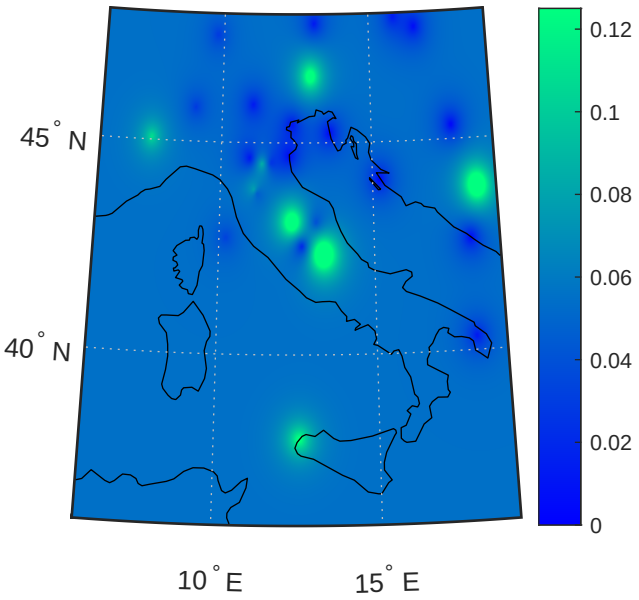

(a)

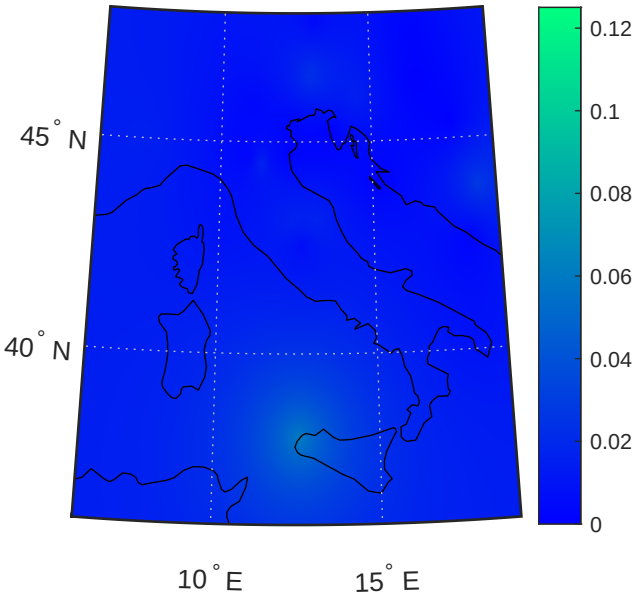

(b)

Figure 3.8: Generated spatial anomaly detection thresholds for the chosen $TEC_{\Delta}^{\text{w-day}}$ tail probabilities (a) 0.005, and (b) 0.05.

The generated spatial anomaly detection thresholds extract the underlying TEC variation distribution of each reference station independently that these

thresholds shall be generated spatially adaptive way for any given reference station or region.

3.2.3.2 Spatio-Temporal anomaly detection thresholds

By using daily geomagnetic parameters, each day of training and validation sets shall be clustered with respect to its geomagnetic activity. After the geomagnetic activity based clustering of the days, it is possible to generate a spatial anomaly detection threshold for each different day cluster. A spatio-temporal anomaly detection threshold which varies in both space and time shall be generated by applying a different spatial anomaly detection threshold for each different day.

Unsupervised machine learning techniques do not require labeled data to operate. k-means clustering is one of the widely used unsupervised machine learning techniques. The technique is based on finding k different cluster means on m dimensional space, iteratively. Pseudocode of the applied k-means clustering technique is presented in Algorithm 2.

To demonstrate clustering performance of the proposed technique, daily geomagnetic parameters data, g_d is defined for day d as a five dimensional vector consisting of daily geomagnetic parameters of A_p, AE, K_p, Dst indices, and SSN. Geomagnetic parameters data is stored for each day in between 2005 and 2016. Each dimension or geomagnetic parameter of the g_d is normalized with respect to its minimum and maximum values. k-means clustering technique is executed on the normalized g_d for different k values that ranges between 1 and 20. For each execution of the technique, a mean silhouette score is calculated and stored. Optimal k value that maximizes the mean silhouette score is chosen as $k = 3$ [105, 106]. Generated cluster means for the geomagnetic parameters data are presented in Table 3.3 with mean value of each dimension of g_d.

When real time operation of the proposed is concerned, the proposed runs in near-real time operation due to requirement for further processing on some of the

chosen geomagnetic parameters. The EQ-PD technique requires some geomagnetic data such as Dst and AE indices that may be provisional and not final for the current time. These geomagnetic parameters require further processing to remove possible artificial noise and baseline shifts [94]. Despite this processing requirement of the data, EQ-PD technique is immune to possible errors on the data. The effect of artificial noise and baseline shifts on k-means clustering technique is minimal that the technique processes data in the order of years. Hence cluster mean locations shall be slightly shifted due to these errors. Furthermore, EQ precursor detection process is also immune to these errors that EQ precursor detection is performed by Support Vector Machine technique which is hardly affected by outliers in the data.

Algorithm 2 k-means Clustering Pseudocode

```
// Parameter Definition //
N_iter ← Maximum number of iterations
N_samples ← Number of day sample
k ← Number of cluster locations

// Initialization //
for i = (1 to k) do
    μ_i ← Initialize the mean for the i'th cluster
end for

// Iterative Search //
for t = (1 to N_iter) do
    for d = (1 to N_samples) do
        z_d = argmin_i ‖μ_i − g_d‖ ← Assign day sample d to the closest mean location
    end for
    for i = (1 to k) do
        μ_i = MEAN(g_d : z_d = k) ← Re-calculate mean of the i'th cluster
    end for
end for
```

Table 3.3: Generated cluster means for the days in between 2005 and 2016 and mean value of each geomagnetic parameter.

k-means cluster	K_p	SSN	Dst (nT)	A_p (nT)	AE (nT)
1	3.19481	51.8314	-25.8080	21.7639	350.6083
2	1.12953	20.9920	-5.4621	4.8475	93.5610
3	1.40000	112.5771	-5.8790	6.2715	127.5974
Mean	1.58834	50.9175	-9.3896	8.3969	150.7634

As shown in Table 3.3, k-means clustering technique obtained the highest mean silhouette score when $k = 3$ and generated three different cluster means based on the chosen geomagnetic parameters of A_p, AE, K_p, Dst indices, and SSN. Each of the day cluster mean represents a different level of ionospheric geomagnetic activity. When cluster mean geomagnetic activity levels are compared to each other, cluster-1 and cluster-3 represent the days with relatively higher geomagnetic activities. Cluster-2 represents the days with relatively lower geomagnetic activities in the ionosphere. Once these cluster means are obtained, each upcoming day shall be classified with respect to its geomagnetic activity by measuring the distance between geomagnetic parameters of a chosen day d, g_d and cluster means. The chosen day will be assigned to the cluster with the smallest distance.

Spatio-temporal anomaly detection thresholds shall be generated by estimating k different Pareto cumulative distributions that are obtained from clustered days of training and validation sets. Clustered days are classified with respect to the k different cluster means that are presented in Table 3.3. For a region of choice, the k different Pareto cumulative distributions shall be estimated for each reference station. For the TORI reference station located in the region presented in Fig. 3.1, time interval in between 2005 and 2016 and three different activity states of the ionosphere, estimated upper-truncated Pareto negative cumulative distributions of $TEC_{\Delta}^{\text{w-day}}$ are presented in Fig. 3.9a.

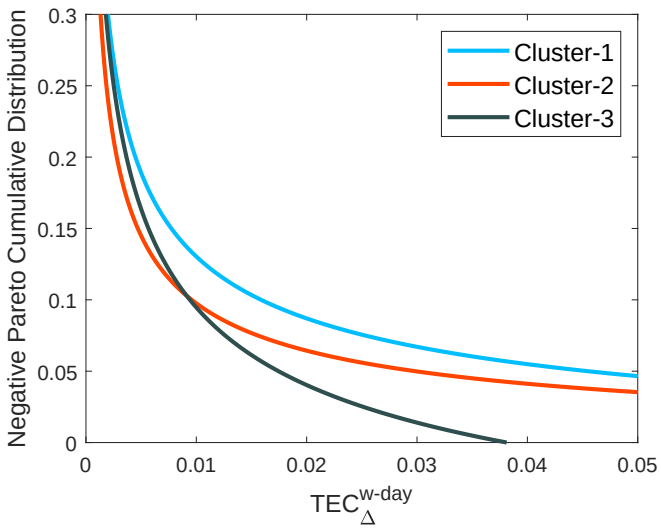

(a)

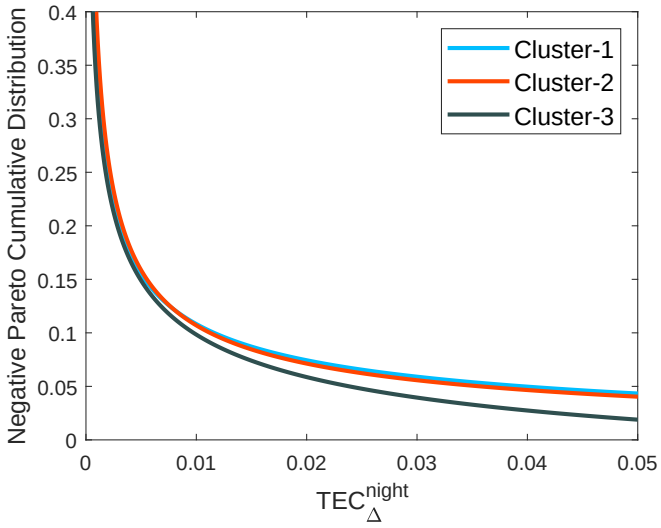

(b)

Figure 3.9: (a) Whole day $TEC_{\Delta}^{\text{w-day}}$ negative upper-truncated Pareto cumulative distributions of TORI reference station for the three different day clusters, (b) Night-time $TEC_{\Delta}^{\text{night}}$ negative upper-truncated Pareto cumulative distributions of TORI reference station for the three different day clusters.

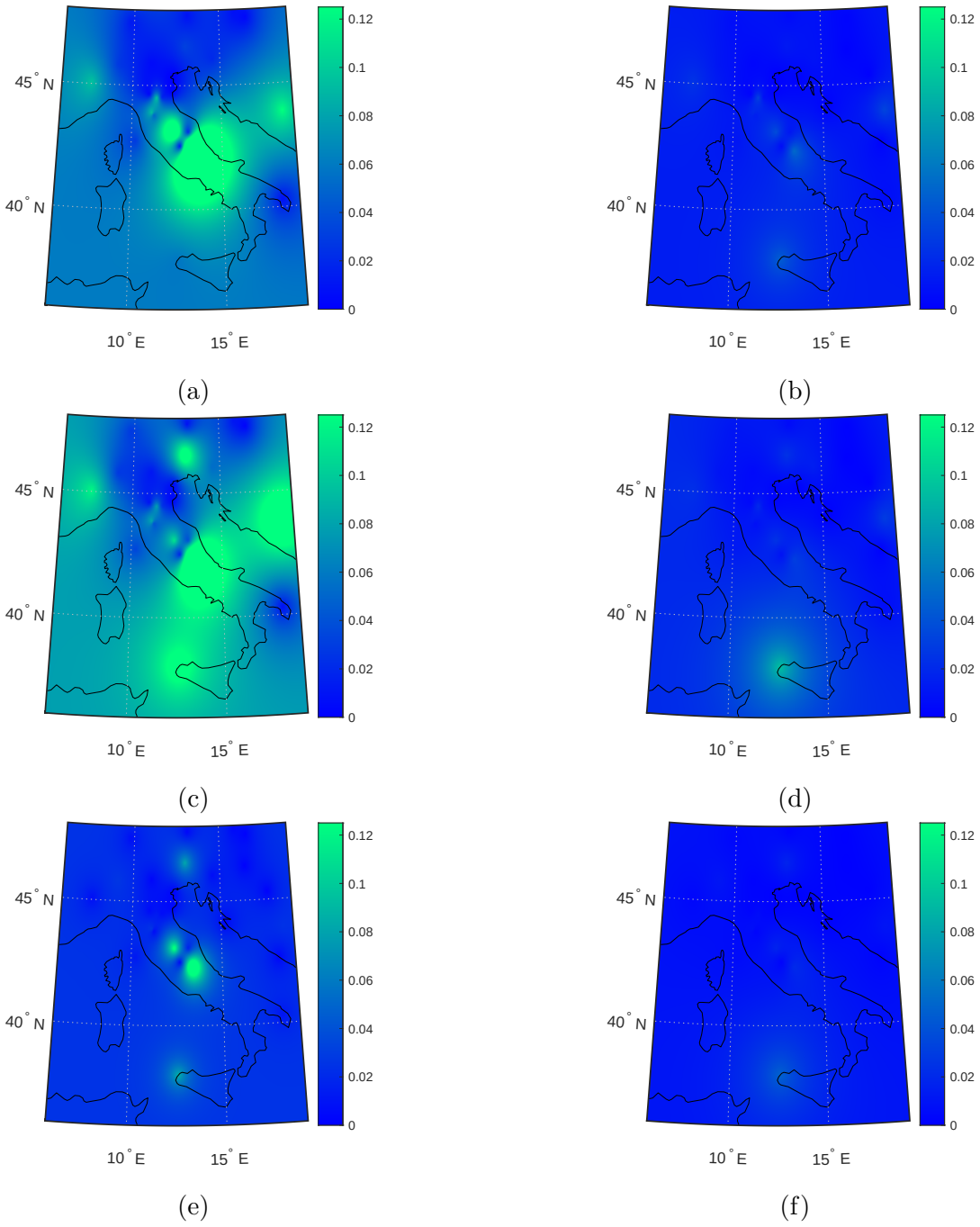

Figure 3.10: Generated spatio-temporal anomaly detection thresholds for the different clusters and chosen $TEC_{\Delta}^{\text{w-day}}$ tail probabilities (a) Cluster-1 0.005, (b) Cluster-1 0.05, (c) Cluster-2 0.005, (d) Cluster-2 0.05, (e) Cluster-3 0.005, (f) Cluster-3 0.05.

As presented in Fig. 3.9a, a chosen TEC variation tail probability of 0.05 corresponds to three different spatial threshold values of 0.045, 0.027 and 0.016 at the TORI reference station for cluster-1, cluster-2 and cluster-3, respectively. Furthermore, the same estimation procedure shall be repeated for the night-time local TEC variations, $TEC_{\Delta}^{\text{night}}$ as shown in Fig. 3.9b. After choosing an appropriate TEC_{Δ} tail probability, it is possible to obtain k different TEC_{Δ} thresholds from each reference station. Hence, a spatio-temporal anomaly detection threshold is generated that it is possible to apply a different spatial threshold for each different day type. Fig. 3.10 presents a spatio-temporal anomaly detection threshold obtained from the set of days that belongs to cluster-1, cluster-2 and cluster-3 in Table 3.3 by choosing TEC_{Δ} tail probability as 0.05 and 0.005. As presented in Fig. 3.10, the generated spatio-temporal anomaly detection thresholds are spatially different than each other.

The generated spatio-temporal anomaly detection thresholds extract the underlying TEC variation distributions of each reference station for different activity states of the ionosphere independently. Hence, these thresholds shall be generated both spatially and temporally adaptive way for any given reference station or region.

3.2.4 Generation of EQ Precursor Detection Signal

The proposed EQ-PD is based on the detection of beyond the expected TEC_{Δ} anomalies triggered by strong seismic activities. TEC_{Δ} behaviours of the reference stations are examined to learn the expected TEC_{Δ} behaviours when there is no seismic activity in the ionosphere. Hence, it is possible to identify beyond the expected TEC_{Δ} anomalies when there is seismic activity in the ionosphere.

For a given TEC_{Δ} tail probability, an anomaly detection threshold can be generated by finding the corresponding TEC_{Δ} on the estimated Pareto distributions for each reference station of interest. Since the estimated Pareto distributions are obtained from no-seismic activity days, they depict the TEC_{Δ} behaviour of each reference station for the days with no-seismic activity. Therefore, each different

TEC_Δ tail probability corresponds to a different probability of false alarm (P_{FA}) or rate of TEC_Δ anomaly detections for the no-seismic activity days class.

Major disturbances in TEC are reported prior to 1 to 9 days prior to strong EQS by several studies [23, 103, 104, 107]. Several TEC related disturbances are reported and statistically analyzed in [38]. As presented in [38], it is 1.8 to 3.6 times more likely to observe TEC disturbances prior to 1 to 9 days to strong EQs than observing these disturbances when there is no seismic activity. Due to these facts, days of seismic activity days class are chosen with respect to 9 days prior to each strong EQ including the EQ days. All the remaining seismically inactive days are included to no-seismic activity days class.

To demonstrate the relationship between TEC_Δ tail probabilities and P_{FA}, first 274 days of 2016 are divided into seismic activity days and no-seismic activity days classes. Since significant TEC disturbances are observed 9 days prior to an EQ, these days including with the EQ day are selected for the seismic activity days class. Seismic activity days class consists of 24 different time intervals including 9 days prior to the 24 EQs that are presented in Table 3.7. The relationship between TEC_Δ tail probability and P_{FA} obtained from a whole-day anomaly detection signal for the no-seismic activity days class is presented in Fig. 3.11. As shown in Fig. 3.11, different statistical behaviours can be obtained for spatial anomaly detection and spatio-temporal anomaly detection thresholds by adjusting TEC_Δ tail probabilities on the estimated Pareto distributions.

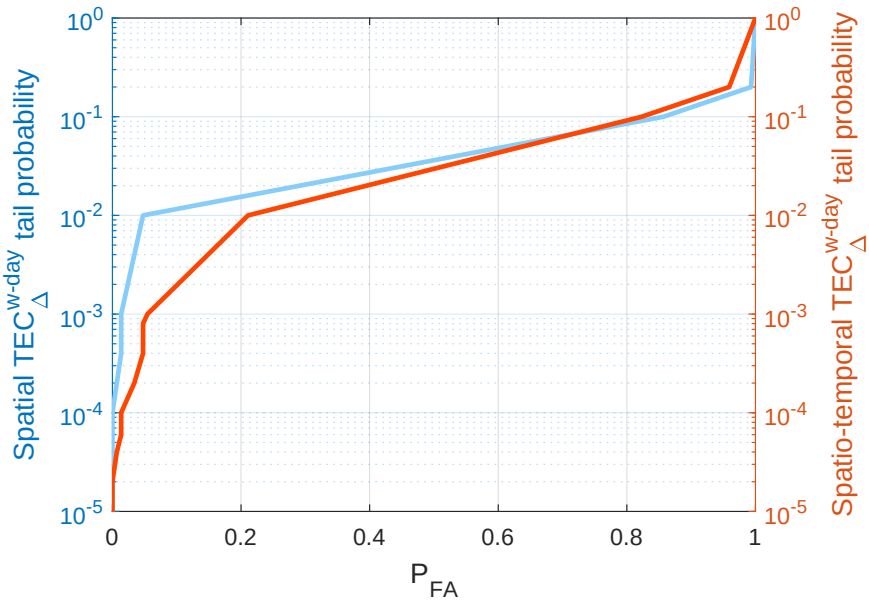

Figure 3.11: Relationship between TEC_Δ tail probability and P_{FA} obtained from the days with no seismic activity during the first 274 days of 2016.

For a TEC_Δ tail probability, anomaly decisions can be made by applying the corresponding anomaly detection thresholds on the anomaly detection signal. EQ precursor detection signals can be generated by gathering all daily anomaly decisions obtained from different combinations of anomaly detection signals and anomaly detection thresholds. In this study, 6 different anomaly detection signals are generated. Three different whole day and three different night-time anomaly detection signals are generated by altering the radius parameter R_r of spatio-temporal TEC interpolation technique depicted in Section 2.2 and Section 2.3. Spatial and spatio-temporal anomaly detection thresholds are generated for these six different anomaly detection signals as detailed in Section 3.2.3.1 and Section 3.2.3.2. During the threshold generation process, 23 different TEC_Δ tail probabilities are chosen for each anomaly detection threshold. For 6 different anomaly detection signals, 2 different anomaly detection threshold types and 23 different threshold levels, $6 \times 2 \times 23 = 276$ different anomaly decisions shall be generated for each day of interest. Each anomaly decision is marked as 1's if there is a threshold exceedance in a chosen anomaly detection signal and anomaly detection threshold. If there is no threshold exceedance, then the related anomaly decision

is marked as 0. Daily EQ precursor detection signal is formed by stacking all 276 different anomaly decisions and visualized in Fig. 3.12.

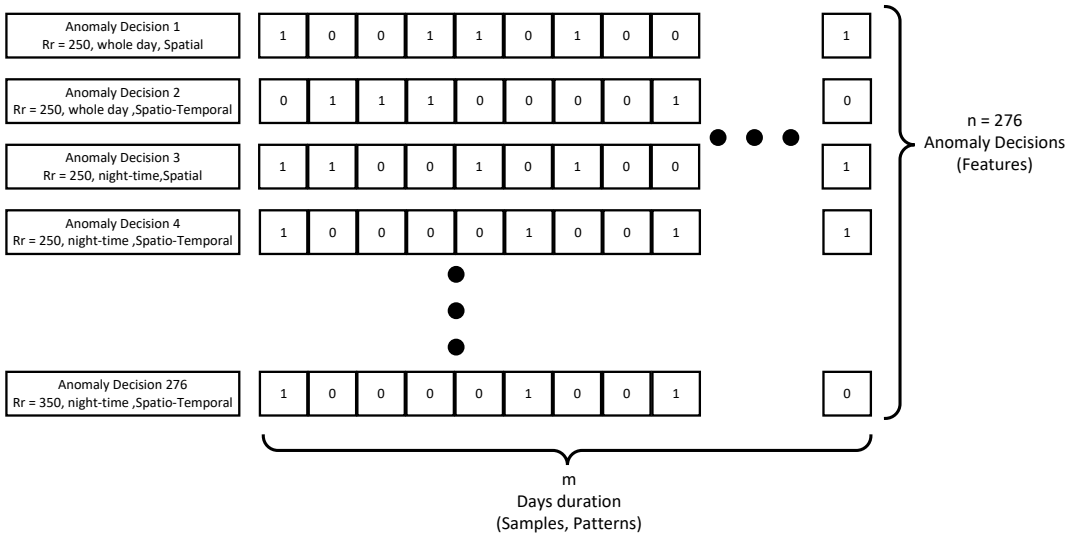

Figure 3.12: EQ precursor detection signal.

3.2.5 Generation of EQ Precursor Detections

Support Vector Machine, (SVM) is one of the most robust and widely used prediction methods used in machine learning [108, 109, 110]. SVM is a supervised machine learning technique that shall either perform binary linear classification or binary non-linear classification with the use of kernels. In this work, SVM is chosen to classify days of EQ precursor detection signal into seismic activity days and no-seismic activity days classes. Each day training and validation set of day is labeled as $y = 1$, if the day belongs to seismic activity days class. All the remaining days of no-seismic activity class are labeled as $y = 0$. The goal of the SVM is to obtain the optimal decision boundary coefficients, $\boldsymbol{\theta}$ that minimize the following cost function:

$$\min_{\boldsymbol{\theta}} C_{reg} \sum_{d=1}^{m} y^{(d)} C_{1;h}(\boldsymbol{\theta}^T \mathbf{s}^{(d)}) + (1 - y^{(d)}) C_{0;h}(\boldsymbol{\theta}^T \mathbf{s}^{(d)}) + \frac{1}{2} \sum_{j=1}^{m} \boldsymbol{\theta}_j^2, \qquad (3.10)$$

where n is the n daily anomaly decisions stacked in EQ precursor detection signal,

m is the day duration of EQ precursor detection signal, C_{reg} is the regularization constant. Hinge loss functions of $C_{0;h}$ and $C_{1;h}$ represent the cost of classifying when day labels are $y = 0$ and $y = 1$, respectively and defined as follows:

$$C_{0;h}(\boldsymbol{\theta}^T \mathbf{s}^{(d)}) = \max(0, (1 + \boldsymbol{\theta}^T \mathbf{s}^{(d)})), \tag{3.11}$$

$$C_{1;h}(\boldsymbol{\theta}^T \mathbf{s}^{(d)}) = \max(0, (1 - \boldsymbol{\theta}^T \mathbf{s}^{(d)})), \tag{3.12}$$

$\mathbf{s}^{(d)}$ represents a m dimensional sample vector that shall be obtained by applying a Gaussian Kernel with parameter σ on the d'th day sample of the EQ precursor detection signal as follows:

$$\mathbf{s}^{(d)} = [\mathbf{s}_1^{(d)} \cdots \mathbf{s}_r^{(d)} \cdots \mathbf{s}_m^{(d)}]^T, \tag{3.13}$$

$$\mathbf{s}_r^{(d)} = \exp\left(- \frac{\|\mathbf{P}_E^{(d)} - \mathbf{P}_E^{(r)}\|^2}{2\sigma^2} \right) = \exp\left(- \frac{\sum_{j=1}^{n} (P_{E;j}^{(d)} - P_{E;j}^{(r)})^2}{2\sigma^2} \right), \tag{3.14}$$

where $P_{E;j}^{(d)}$ represents the j'th entry or anomaly decision of the EQ precursor detection signal for the day d.

During the training of the SVM, each sample vector, $\mathbf{s}^{(d)}$ is multiplied by a sample weight, $w^{(d)}$. Sample weights are initially chosen as 1, $w_{init}^{(d)} = 1$ for d'th sample and normalized with respect to number of samples in each class to approximate prior probabilities of the classes. Prior probability of the no seismic activity class or Class 0, $p_D(0)$ and prior probability of seismic activity class or Class 1, $p_D(1)$ shall be defined as:

$$\mathbf{p}_D = \begin{bmatrix} p_D(0) \\ p_D(1) \end{bmatrix} = \frac{1}{m_0 + m_1} \begin{bmatrix} m_0 \\ m_1 \end{bmatrix}. \tag{3.15}$$

where m_0 is the number of samples in Class 0 and m_1 is the number of samples in Class 1.

Additionally, prior probabilities of these classes shall be modified to train the SVM in a cost-sensitive way. Prior probability vector, $\mathbf{p}_D$ shall be updated by multiplying the vector with a cost matrix as follows:

$$\mathbf{p}_{DC} = \begin{bmatrix} 0 & Cost_{FA} \\ Cost_{MD} & 0 \end{bmatrix} \mathbf{p}_D, \tag{3.16}$$

where $Cost_{FA}$ is the cost of generating a false alarm and $Cost_{MD}$ is the cost of generating a misdetection. Sample weight of the d'th sample shall be obtained by using updated prior probability vector, $\mathbf{p}_{DC}$ for $d \in$ Class 0 as in:

$$w^{(d)} = \frac{w_{init}^{(d)}}{\sum\limits_{\forall d \in Class\ 0} w_{init}^{(d)}} p_{DC}(0), \tag{3.17}$$

and when $d \in$ Class 1:

$$w^{(d)} = \frac{w_{init}^{(d)}}{\sum\limits_{\forall d \in Class\ 1} w_{init}^{(d)}} p_{DC}(1). \tag{3.18}$$

Updated sample weights incorporate cost of misdetection and cost of false alarms into the SVM objective function in (3.10). Hence, SVM generates the decision boundary, $\boldsymbol{\theta}$ with respect to these costs that the training of the SVM will be in a cost-sensitive way. As an example, choosing $Cost_{MD} = 1$ and $Cost_{FA} > 1$ will enforce the trained SVM to reduce number of generated false alarms.

Training of the proposed SVM model requires hyperparameter tuning that C_{reg}, σ and $Cost_{FA}$ parameters affect the precursor detection performance of EQ-PD. Hence, training shall be performed for different combinations of C_{reg}, σ and $Cost_{FA}$ parameters on the training set of days. Thereafter, for each chosen combination decision boundary coefficients, $\boldsymbol{\theta}$ should be obtained. Among all decision boundary coefficient sets, the ones with the highest performance on the validation set of days should be chosen as the optimal decision boundary coefficients. Performance of the EQ-PD will be evaluated with this set of decision boundary coefficients on the test set of days.

In the following section, precursor detection performance of the proposed EQ-PD technique will be investigated for the days in 2014 and 2016.

3.3 Precursor Detection Performance of the Proposed EQ-PD Technique

Performance of the proposed EQ-PD technique is investigated on training, validation and test data sets that provide an unbiased evaluation of the chosen SVM model. To achieve unbiased evaluation of the technique, three nonintersecting EQ precursor detection signals for training, validation and testing of the model are generated and presented in Table 3.4. As shown in Table 3.4, start and end dates, number of days and number of daily different EQs in these time periods are presented for training, validation and test sets. Precursor detection performance of the EQ-PD technique is evaluated on the test set of days. During the test set of dates and the region of choice, 24 daily different EQs had taken place and presented in Table 3.7. All of the presented EQs had a magnitude greater than 4 in Richter scale [101]. If multiple EQs had taken place at the same day in the chosen region, the EQ with the highest magnitude is chosen for the test performance evaluation. As shown in Table 3.7, 24 daily different EQs are investigated out of 43 total EQs.

Table 3.4: Training, validation and test set information.

Data set	Date (D Month YYYY)		Number of Days	Number of daily different EQs
	Start	End		
Training	1 January 2014	1 April 2015	456	35
Validation	2 April 2015	23 December 2015	266	21
Test	24 December 2015	30 September 2016	282	24

Additionally, random guessing experiments are performed to show statistical significance and reliability of the precursor detection performance of the EQ-PD

technique. Results of the experiments are compared with the EQ-PD precursor detection performances to test their statistical significance. Test results and reliability analysis of the proposed are presented in subsequent subsections.

3.3.1 Test Results

In the test performance evaluation, 3 different whole-day and 3 different night-time TEC estimates are generated by adjusting the TEC estimation radius parameter, R_r as 250 km, 300 km and 350 km as detailed in Section 2.2. The TEC estimates are generated for the TEC measurements of reference stations located in the region of choice for the days in between dates 1 January 2005 (first day of training set) and 30 September 2016 (last day of test set). Whole day $TEC_{\Delta}^{\text{w-day}}$ and night-time $TEC_{\Delta}^{\text{night}}$ local TEC variations are calculated and whole-day and night-time anomaly detection signals are generated for all the reference stations located in the region of choice for the same time duration as detailed in Section 3.2.2.

As detailed in Section 3.2.3.1, Spatial TEC_{Δ} behaviours of the generated anomaly detection signals are obtained by estimating TEC_{Δ} Pareto cumulative distributions for the no-seismic activity days in between dates of 1 January 2005 (first day of training set) and 1 April 2015 (last day of training set). Similarly, as detailed in Section 3.2.3.2, spatio-temporal TEC_{Δ} behaviours of the generated anomaly detection signals are obtained by clustering the no seismic activity class days into $k = 3$ different day clusters and estimating TEC_{Δ} Pareto cumulative distributions for each of these day clusters for the no-seismic activity class days in between dates of 1 January 2005 (first day of training set) and 1 April 2015 (last day of training set). In addition to the TEC_{Δ} behaviours, cluster mean locations are also obtained from the training set of days. Upcoming days of validation and test set of days are clustered with respect to these $k = 3$ cluster mean locations. Finally, spatial and spatio-temporal anomaly detection thresholds are also generated by selecting 23 different TEC_{Δ} tail probabilities on the related TEC_{Δ} Pareto cumulative distributions.

EQ precursor signal of training set shall be obtained by thresholding anomaly detection signals with the appropriate anomaly detection thresholds and stacking resulting 276 different daily anomaly decisions for the training set of dates presented in Table 3.4. For the validation and test set of dates presented in Table 3.4, EQ precursor signals are generated by thresholding future anomaly detection signals with the appropriate anomaly detection thresholds that are obtained from training set.

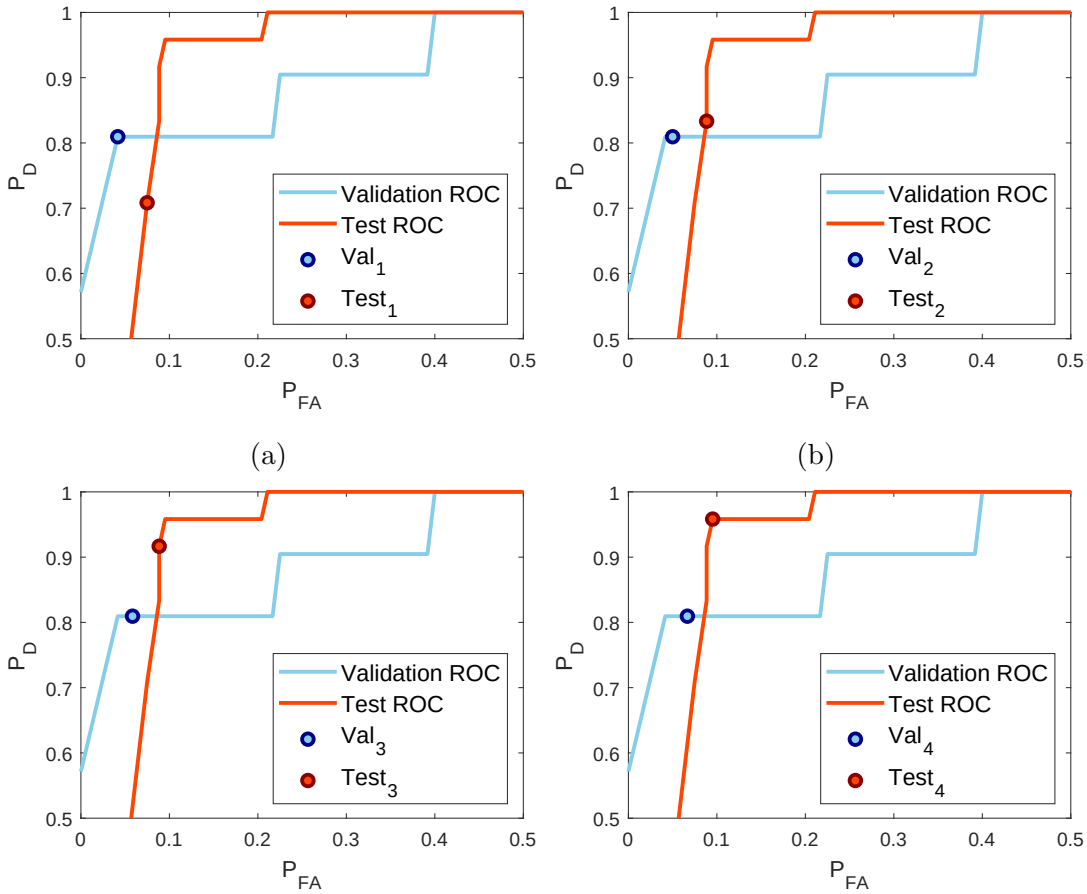

Figure 3.13: ROC curves of validation (blue) and test (orange) sets and the chosen validation (blue circle) and test (orange circle) ROC points for (a) Validation$_1$ and Test$_1$, (b) Validation$_2$ and Test$_2$, (c) Validation$_3$ and Test$_3$, (d) Validation$_4$ and Test$_4$.

For different combinations of the SVM model parameters, C_{reg}, σ and $Cost_{FA}$ different SVM models are trained on the EQ precursor detection signal that is generated for the training set of days. During the training of the models, SVM regularization parameter, C_{reg} is chosen from the range 0.01 and 10000, Gaussian kernel parameter, σ is chosen from the range 0.001 and 1000 and cost of generating a false alarm parameter, $Cost_{FA}$ is chosen from the range 1 and 2.1. Cost of generating a misdetection parameter, $Cost_{MD}$ is chosen as 1 during the training. SVM Decision boundary coefficients, $\boldsymbol{\theta}$ are obtained for each different model parameter combinations. Each SVM decision boundary obtained from the decision boundary coefficients are validated on the EQ precursor detection signal that is generated for the validation set of days. Receiver Operating Characteristic (ROC) curve of validation set is obtained by choosing the validated SVM models with highest probability of detection (P_D) for a given P_{FA} on the validation set of days. Similarly, ROC curve of test set is also obtained by applying the chosen validated SVM models on the EQ precursor detection signal that is generated for the test set of days. Validation and test ROC curves of the chosen SVM models with different parameters are presented in Fig. 3.13.

When the generated ROC curves in Fig. 3.13 are taken into consideration, these curves exhibit a stepped behaviour in P_D axis since P_D values are calculated with respect to small numbers of EQ precursors in validation and test sets. There are 21 EQ precursors in the validation set and 24 EQ precursors in the test set that P_D shall take 21 and 24 distinct nonzero values during the performance evaluations of validation and test sets, respectively. Furthermore, P_{FA} axis shall be controlled by adjusting TEC_{Δ} tail probabilities of anomaly detection thresholds as illustrated in Fig. 3.11. Hence, the generated anomaly detection thresholds have no control over P_D axis that increasing P_{FA} may not always result with increased number of EQ precursor detections. Finally, the generated ROC curves are visualized for $0.5 \leq P_D \leq 1$ and $0 \leq P_{FA} \leq 0.5$ that performances of ROC points with $P_D \leq 0.5$ or $P_{FA} \geq 0.5$ are not taken into consideration during visualization.

To determine EQ precursor detection performance of the proposed, 4 different ROC points are chosen from the validation ROC curve and named as: Validation$_1$,

Validation$_3$, Validation$_3$ and Validation$_4$. EQ precursor detection performance of these ROC points with their corresponding test ROC points are also presented in Fig. 3.13. Furthermore, number of detected EQ precursors, number of false precursor detections and SVM model parameters are presented in Table 3.5. for the chosen ROC points. As shown in Fig. 3.13 and Table 3.5, validation ROC points achieve smaller number of false alarms, while their corresponding test ROC points generate higher number of false alarms.

EQ precursor detection distances shall be calculated by assigning the reference station with the highest level of TEC_{Δ} anomaly to each day. Hence, every EQ precursor detection shall be assigned to a reference station. For a chosen EQ epicenter, EQ precursor detection distance shall be obtained by averaging the distances between the epicenter and locations of the reference stations where the related precursor detected. EQ precursor detection distances shall also be averaged on all EQs to generate average precursor detection distances. For the test ROC points that are presented in Fig. 3.13, average EQ precursor detection distances are presented in Table 3.5. As shown in Table 3.5, Test$_1$ ROC point achieves the smallest average precursor detection distance, while Test$_4$ has the furthermost average EQ precursor detection distance. Precursor detection histograms of these ROC points are also visualized in Fig. 3.14.

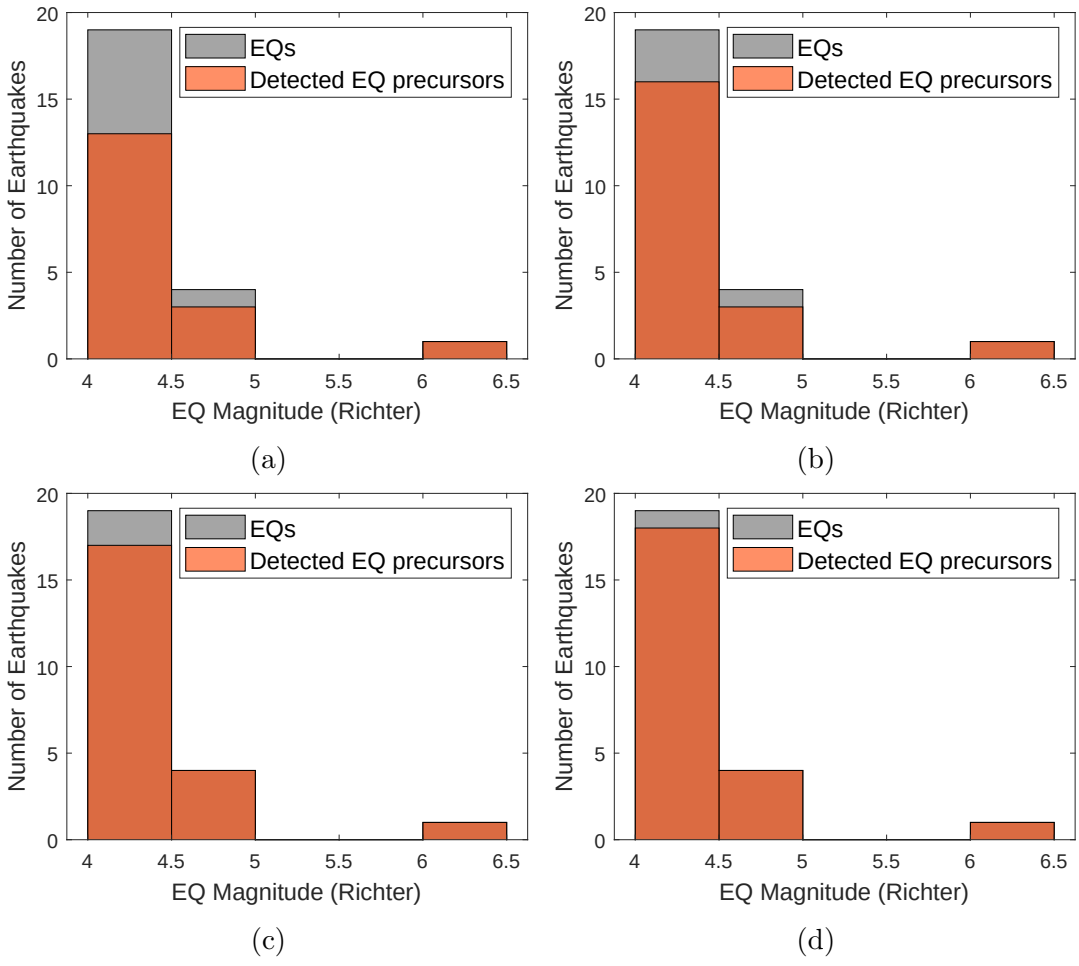

Figure 3.14: EQ Precursor detection histograms for ROC points (a) Test_1, (b) Test_2, (c) Test_3 and (d) Test_4.

Table 3.5: For the chosen validation and test ROC points : number of detected EQ precursors, number of all EQs, number of false precursor detections, number of no-seismic activity days (false alarm days), SVM training parameters and average precursor detection distance for all EQs ($\sum M$), 11 weak EQs with magnitude smaller than 4.3, 10 moderate EQs with magnitudes in between 4.3 and 4.6 and 3 strong EQs with magnitudes greater than 4.6 in Richter scale.

ROC point	Detected EQ Precursors	Number of EQs	Generated False Alarms	No-seismic activity days	Training Parameters			Average precursor detection distance (km)			
					C_{reg}	σ	$Cost_{FA}$	$\sum$M	M< 4.3	4.3 ≤M< 4.6	4.6 ≤M
$Validation_1$	17	21	5	120	80	500	1.6	-			
$Test_1$	17	24	11	147	-			380	389	415	280
$Validation_2$	17	21	6	120	0.2	30	1.2	-			
$Test_2$	20	24	13	147	-			426	495	402	280
$Validation_3$	17	21	7	120	1	40	1.8	-			
$Test_3$	22	24	13	147	-			442	508	431	280
$Validation_4$	17	21	8	120	0.2	20	1.5	-			
$Test_4$	23	24	14	147	-			466	545	443	280

SVM hyperparameter tuning process decides if the resulting decision boundary coefficients are overfitting to the EQ precursor detection signal of the training set of days or not. As the SVM regularization parameter, C_{reg} gets higher, decision boundary coefficient regularization will reduce and results with overfitting of the trained model. Furthermore, as the Gaussian kernel parameter, σ gets smaller, increases the variance of the features and also results with overfitting of the trained model. A shown in Table 3.5, trained SVM models neither overfitting nor underfitting to the training data. As a result, EQ-PD technique detects 22 EQ precursors out of 24 EQs and generates 13 different false alarms in 147 days of no-seismic activity class days in 2016.

3.3.2 Reliability Analysis

In order to show statistical significance and reliability of the precursor detection performance of the EQ-PD technique, 100000 random guessing Monte Carlo simulations are performed with respect to ROC space parameters of the chosen validation and test ROC points. Performance of the proposed is investigated in terms of detected EQ precursors, and generated daily false alarms in Section 3.3.1. However, random guessing simulations shall be performed by using both daily precursor detections and false precursor detections. In order to perform the random guessing simulations, ROC space parameters are defined as follows :

- TP_{EQ}, Number of detected EQ precursors,
- FN_{EQ}, Number of of mis-detected EQ precursors,
- $N_{Pos,EQ}$, Number of EQs,
- TP_{day}, Number of detected daily precursors,
- FN_{day}, Number of of mis-detected daily precursors,
- $N_{Pos,day}$, Number of seismically active days,
- FP_{day}, Number of generated daily false alarms,

- TN_{day}, Number of daily true negatives,
- $N_{Neg,day}$, Number of possible false alarm days.

TP_{EQ}, FN_{EQ} and $N_{Pos,EQ}$ are the ROC space parameters that are related with the detection of an EQ precursor. The remaining, TP_{day}, FN_{day}, $N_{Pos,day}$, FP_{day}, TN_{day} and $N_{Neg,day}$ are the ROC space parameters that are related with daily precursor decisions. Note that, multiple daily precursor decisions may lead to a detection of only one EQ precursor. For the chosen ROC points in Table 3.5, all the ROC space parameters are presented in Table 3.6. Pseudocode of the random guessing simulation is presented in Algorithm 3.

For each random guessing simulation, EQ precursor detection performance is calculated by using Matthews correlation coefficient (MCC) score defined as follows, [111]:

$$MCC(TP, TN, FP, FN) = \frac{TP \times TN - FP \times FN}{\sqrt{(TP + FP) \times (TP + FN) \times (TN + FP) \times (TN + FN)}}. \quad (3.19)$$

MCC score is a one dimensional measurement metric for two dimensional ROC space points. It is possible to compare MCC score of a ROC point with a random guessing experiment. $MCC = 1$ corresponds to the case when all EQ precursors are detected without generating a single false alarm. $MCC = 0$ corresponds to the case when EQ precursor detection performance is not better than random guessing. Finally, $MCC = -1$ corresponds to the case when all EQ precursors are missed and false alarms are generated for each day of no-seismic activity days class.

MCC scores of the chosen ROC points in Table 3.5 are defined as MCC_R and presented in 3.6. Additionally, MCC_R of the related ROC-points and MCC score histograms of random guessing Monte Carlo simulations for the chosen validation and test ROC points are presented in Fig. 3.15 and Fig. 3.16, respectively. Mean and standard deviations of these random guessing simulations are also defined as μ_{RG} and σ_{RG} and presented in Table 3.6. As presented in Fig. 3.15 and Fig.

Algorithm 3 Random Guessing Monte Carlo Simulation

// Parameter Definition //
$N_{MC} \leftarrow$ Number of Monte Carlo Simulations
$N_{Pos,EQ} \leftarrow$ Number of EQs
$N_{Precursor} = TP_{day} + FP_{day} \leftarrow$ Number total precursor detections
$N_{days} \leftarrow$ Number total days
$MCC_{vec} \leftarrow$ A vector to store Matthews correlation coefficient scores

for `n = (1 to` N_{MC}`)` **do**

// Initialization //
$P_{date} \leftarrow$ Assign each precursor detection to an unique date
$EQ_{date} \leftarrow$ Assign each EQ to an unique date
Define Seismic `Activity class days` with respect to EQ_{date}
for `d = (1 to` N_{days}`)` **do**
if `d` $\notin$ `Seismic Activity class days` **then**
$N_{Neg,day} = N_{Neg,day} + 1$
end if
end for

// Find Detected EQ Precursors and False Alarms//
for `EQ = (1 to` EQ_{date}`)` **do**
for `P = (1 to` P_{date}`)` **do**
if `P` related to `EQ` **then**
$TP_{EQ} = TP_{EQ} + 1$
break
end if
end for
end for

for `P = (1 to` P_{date}`)` **do**
if `P` $\notin$ `Seismic Activity class days` **then**
$FP_{day} = FP_{day} + 1$
end if
end for

$FN_{EQ} = N_{Pos,EQ} - TP_{EQ}$
$TN_{day} = N_{Neg,day} - FP_{day}$
$MCC_{vec}(n) = MCC_R(TP_{EQ}, FN_{EQ}, TN_{day}, FP_{day})$

end for

3.16,$MCC_R \geq \mu_{RG} + 2 \times \sigma_{RG}$ holds for all the visualized MCC_R. Furthermore, Z-score of MCC_R shall be obtained with respect to μ_{RG} and σ_{RG}. Resulting Z-score will indicate statistical significance of EQ precursor detection performance of the related ROC point and presented for each chosen ROC point in Table 3.6. As presented in Table 3.6, all the z-scores are higher than 2 that precursor detection performance of EQ-PD is superior to the random guessing simulations for all the chosen ROC points.

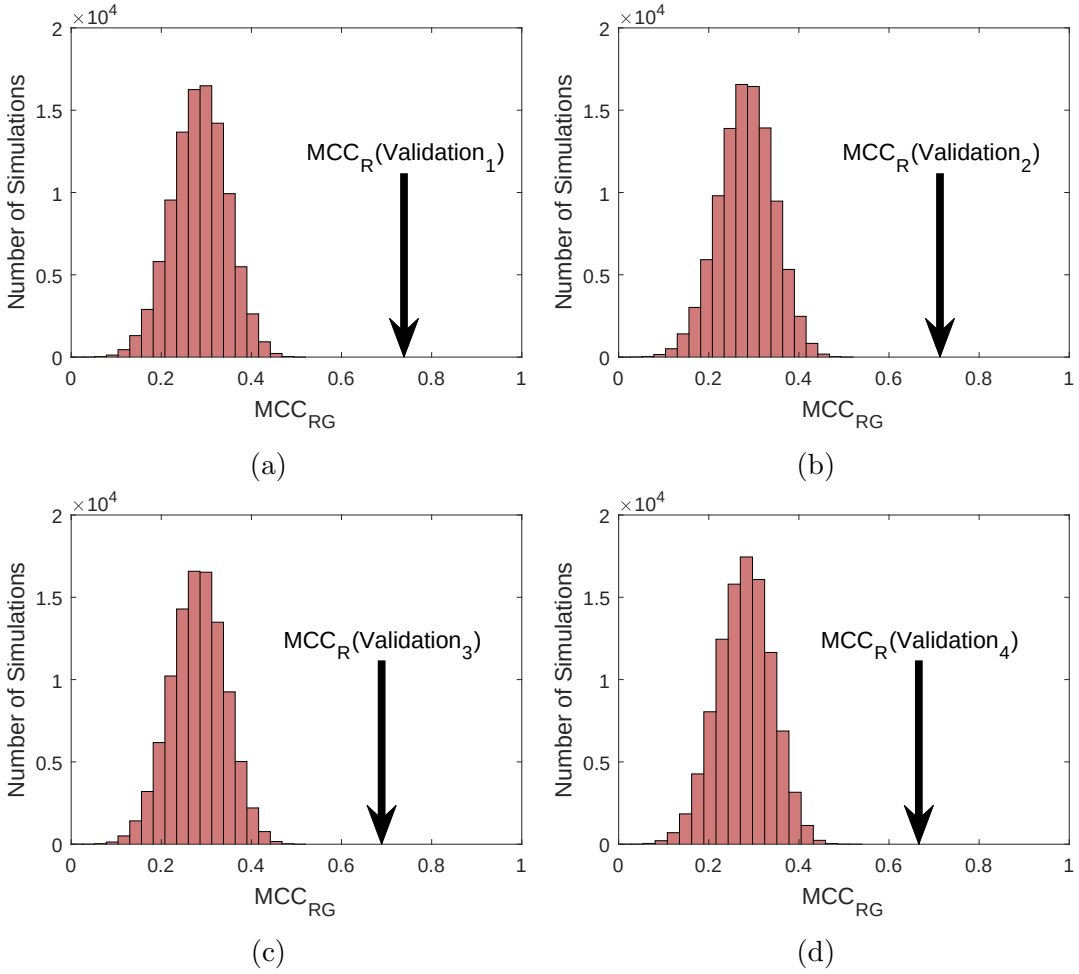

Figure 3.15: MCC score histograms obtained from random guessing Monte Carlo simulations for the chosen ROC points:(a) Validation$_1$, (b) Validation$_2$, (c) Validation$_3$ and (d) Validation$_4$. MCC score of the chosen ROC point is marked by an arrow in each figure.

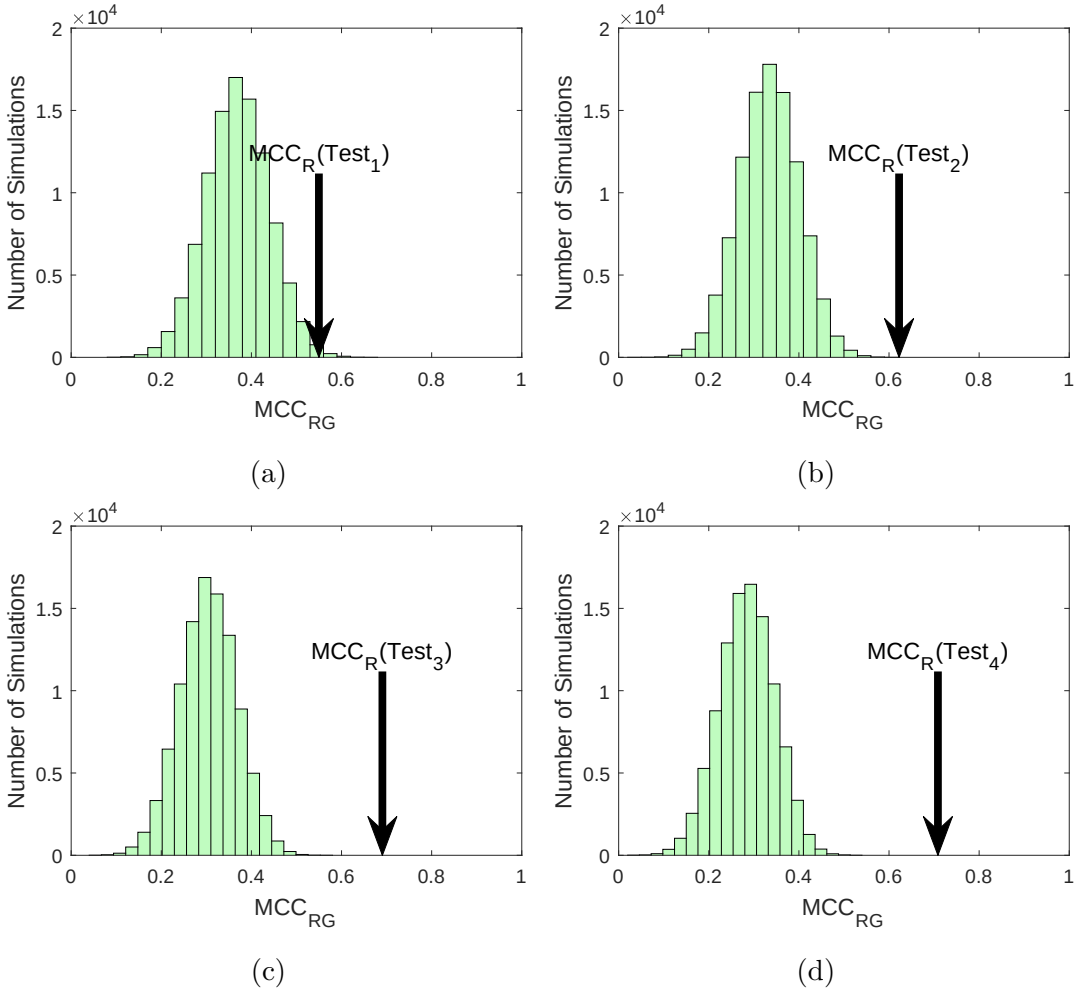

Figure 3.16: MCC score histograms obtained from random guessing Monte Carlo simulations for the chosen ROC points: (a) Test_1, (b) Test_2, (c) Test_3 and (d) Test_4. MCC score of the chosen ROC point is marked by an arrow in each figure.

Table 3.6: For the chosen validation and test ROC points : TP_{EQ}, $N_{Pos,EQ}$, FN_{EQ}, TP_{day}, $N_{Pos,day}$, FN_{day}, FP_{day}, TN_{day} and $N_{Neg,days}$ ROC space parameters, mean and standard deviation of MCC scores of random guessing experiments μ_{RG} and σ_{RG}, MCC score of the related ROC point (MCC_R), Z-score of MCC_R.

ROC point	Validation_1	Test_1	Validation_2	Test_2	Validation_3	Test_3	Validation_4	Test_4
$TP_{EQ}/N_{Pos,EQ}$	17/21	17/24	17/21	20/24	17/21	22/24	17/21	23/24
$FN_{EQ}/N_{Pos,EQ}$	4/21	7/24	4/21	4/24	4/21	2/24	4/21	1/24
$TP_{day}/N_{Pos,days}$	123/146	81/135	123/146	99/135	123/146	115/135	123/146	125/135
$FN_{day}/N_{Pos,days}$	23/146	54/135	23/146	36/135	23/146	20/135	23/146	10/135
$FP_{day}/N_{Neg,days}$	5/120	11/147	6/120	13/147	7/120	13/147	8/120	14/147
$TN_{day}/N_{Neg,days}$	115/120	136/147	114/120	134/147	113/120	134/147	112/120	133/147
$N_{Pos,days} + N_{Neg}$	266	282	266	282	266	282	266	282
Mean (μ_{RG}) MCC score (RG)	0.28476	0.36973	0.28279	0.33400	0.28092	0.30479	0.27894	0.28388
Std (σ_{RG}) MCC score (RG)	0.06053	0.07059	0.06039	0.06597	0.06014	0.06332	0.06008	0.06171
$MCC_R(TP_{EQ}, FN_{EQ}, TN_{day}, FP_{day})$	0.75335	0.59466	0.73187	0.65564	0.71163	0.71304	0.69248	0.72806
$Z = (MCC_R - \mu_{RG})/\sigma_{RG}$	7.7410	3.1859	7.4362	4.8751	7.1613	6.4471	6.8825	7.1969

Table 3.7: 24 daily different EQs that have taken place in the region of choice.

EQ # - Date	Time	EQ Epicenter		Mw
(# - DD Month YYYY)	(hh:mm:ss)	Latitude	Longitude	(Richter)
1 - 2 January 2016	12:36:28	36,4556°N	12,1175°E	4,3
2 - 6 January 2016	18:44:46	39,9354°N	15,5508°E	4,4
3 - 8 January 2016	13:07:42	42,9131°N	18,5153°E	4,6
4 - 13 January 2016	17:01:29	36,1699°N	14,7607°E	4,1
5 - 16 January 2016	18:55:11	41,5846°N	14,6515°E	4,4
6 - 17 January 2016	16:36:07	36,5834°N	12,8374°E	4,2
7 - 8 February 2016	15:35:43	37,023°N	14,8791°E	4,5
8 - 14 February 2016	14:51:29	43,0612°N	17,4307°E	4,4
9 - 4 April 2016	18:53:05	39,2273°N	15,4905°E	4,2
10 - 25 May 2016	22:10:28	36,81°N	15,79°E	4,1
11 - 30 May 2016	20:24:20	42,71°N	11,96°E	4,4
12 - 2 June 2016	10:49:12	36,5748°N	11,1289°E	4
13 - 23 June 2016	14:37:56	44,0943°N	9,9234°E	4,2
14 - 5 July 2016	05:54:38	37,5845°N	17,0005°E	4,5
15 - 30 July 2016	20:21:38	44,94°N	7,21°E	4,2
16 - 24 August 2016	01:36:32	42,723°N	13,1877°E	6,2
16 - 24 August 2016	01:56:01	42,6404°N	13,1986°E	4,6
16 - 24 August 2016	02:01:08	42,7856°N	13,1447°E	4,2
16 - 24 August 2016	02:05:55	42,6352°N	13,3022°E	4,1
16 - 24 August 2016	02:07:31	42,6243°N	13,1756°E	4,2
16 - 24 August 2016	02:19:44	42,6817°N	13,1667°E	4
16 - 24 August 2016	02:33:29	42,8413°N	13,1533°E	5,6
16 - 24 August 2016	02:51:27	42,7596°N	13,1812°E	4,1
16 - 24 August 2016	02:59:36	42,8104°N	13,1056°E	4,1
16 - 24 August 2016	03:40:11	42,6522°N	13,2549°E	4,2
16 - 24 August 2016	04:06:51	42,7959°N	13,0745°E	4,5
16 - 24 August 2016	11:50:31	42,8989°N	13,0834°E	4,6

Continued on next page

Table 3.7 – continued from previous page

EQ # - Date (# - DD Month YYYY)	Time (hh:mm:ss)	EQ Epicenter		Mw (Richter)
		Latitude	Longitude	
16 - 24 August 2016	14:02:22	42,7989°N	13,1462°E	4,3
16 - 24 August 2016	17:46:11	42,7279°N	13,2082°E	4,3
16 - 24 August 2016	23:22:06	42,6589°N	13,1775°E	4,1
17 - 25 August 2016	03:17:16	42,7611°N	13,214°E	4,4
17 - 25 August 2016	04:51:41	42,6397°N	13,2478°E	4,2
17 - 25 August 2016	12:36:07	42,6654°N	13,1732°E	4,4
18 - 26 August 2016	04:28:25	42,6°N	13,29°E	4,8
19 - 27 August 2016	02:50:59	42,8608°N	13,2683°E	4,1
20 - 28 August 2016	13:07:34	42,6665°N	13,2488°E	4,3
20 - 28 August 2016	15:55:35	42,7975°N	13,1733°E	4,2
20 - 28 August 2016	16:42:02	42,8814°N	13,102°E	4,3
21 - 31 August 2016	18:12:52	42,8627°N	13,2213°E	4,1
22 - 3 September 2016	01:34:13	42,831°N	13,0956°E	4,4
22 - 3 September 2016	10:18:51	42,87°N	13,21°E	4,4
23 - 11 September 2016	18:39:02	42,68°N	13,28°E	4
24 - 19 September 2016	23:34:26	42,7166°N	13,1893°E	4,1

3.4 Concluding Remarks

In recent studies, ionospheric TEC disturbances have been reported prior to strong seismic activities and EQs. These studies show the fact that ionosphere is affected from the seismic activities in the Earth's crust and surface.

In this study, a novel EQ precursor detection technique, EQ-PD is presented. EQ precursor detection performance of the proposed is investigated on the ionospheric TEC data obtained from EUREF Permanent GNSS Network (EPN) and

geomagnetic parameter data from NASA Goddard Space Flight Center OMNI-Web service. Each daily TEC data is estimated by using a spatio-temporal TEC estimation technique and local TEC variation is calculated by using the Symmetric Kullback Leibler Divergence (SKLD). Local TEC anomalies are detected on the local TEC variations by using a hypothesis testing technique. Alternative or positive hypothesis is defined as the generated local TEC variations in the period of 10 days starting form 9 days prior to an EQ and ending at day of the EQ contain an anomaly due to precursor of the EQ. A Support Vector Machine (SVM) is trained to decide if a EQ precursor decision is a valid EQ precursor detection or not. Near-real time operation performance of the proposed EQ-PD technique is investigated on a validation set and test set which is not included into SVM training process. During the validation set of days 21 EQs with magnitudes greater or equal to 4 in Richter scale occurred in a chosen region around Italy. During the test set of days 24 EQs with magnitudes greater or equal to 4 in Richter scale occurred in the same region. Performance evaluations indicate that EQ-PD shall detect 17 out of 21 EQ precursors while generating 7 false precursor decisions for validation set of days. Similarly, it shall detect 22 out of 24 EQ precursors while generating 13 false precursor decisions for test set of days.

A reliability analysis is also performed to show statistical reliability of the precursor detection performance of the EQ-PD technique. Random guessing Monte Carlo simulations are performed with respect to ROC space parameters of the chosen validation and test ROC points. Matthews correlation coefficient (MCC) analysis on the performance parameters of the proposed EQ-PD technique is also performed. Results of these analysis suggest that EQ-PD outperforms random guessing simulations in all cases.

In conclusion, the proposed EQ-PD technique has a remarkable precursor detection performance in near real-time for dense GPS networks. EQ precursor decisions of the EQ-PD technique shall be fed to another EQ forecasting technique which may be developed in future.

As future work, EQ precursor decision classification shall be performed by an alternative machine learning technique instead of SVM. The alternative technique

should be a supervised, cost-sensitive machine learning technique. Precursor detection performance of the EQ-PD shall be compared with other machine learning techniques rather than random guessing simulations. Furthermore, another study shall be performed to understand precursor detection statistics for different types of EQs. Finally, a noise sensitivity analysis on the TEC measurements shall be performed to understand noise sensitivity of the proposed model based EQ precursor detection technique.

Chapter 4

A DEEP LEARNING BASED EARTHQUAKE PRECURSOR DETECTION TECHNIQUE

Recent studies report the fact that ionospheric TEC anomalies have been occurring before the strong seismic activities and EQs [60, 61, 62]. In this study, a deep learning based ionospheric EQ precursor detection technique, DL-PD is proposed to detect seismic activity triggered TEC anomalies. DL-PD has the following key contributions to the EQ precursor detection literature.

One of the contributions of the proposed DL-PD technique is that it generates GIM-TEC estimates both spatially and temporally adaptive way. Hence, spatio-temporal TEC estimation capability of DL-PD is far more comprehensive when compared to model based techniques.

Another contribution of the proposed is that DL-PD technique is an unsupervised machine learning technique. DL-PD shall work independently from the seismic activity information. Hence, it generates expected GIM-TEC estimates that shall be compared with the observed GIM-TEC to detect spatio-temporal anomalies.

Final contribution to the literature is that DL-PD shall work with any chosen time duration and region of the world. DL-PD requires daily GIM-TEC data to generate daily or hourly EQ precursor decisions.

In this work, GIM-TEC data obtained from NASA Jet Propulsion Laboratory for the region covering most of the Europe, Anatolian region and Middle East with time duration nearly 1.5 years is processed to generate GIM-TEC estimates. The generated estimates are compared with the actual GIM-TEC data to obtain ionospheric TEC anomalies. EQ precursor detection performance of the generated TEC anomaly decisions are evaluated for 500 consecutive days.

This work consists of multiple processing stages. Processed GIM-TEC data and seismic activity information is presented in Section 4.1. Generation of GIM-TEC estimates and precursor detection technique is presented in Section 4.2. Precursor detection performance of the proposed is evaluated in Section 4.3. Finally, concluding remarks and future research directions are presented in Section 4.4.

4.1 Data Collection and Processing

In this study, TEC based Global Ionospheric Maps (GIM-TEC) are processed. TEC data of International GNSS service (IGS) network reference stations are pre-processed by Jet Propulsion Laboratory to generate GIM-TEC data [112]. The GIM-TEC data shall be further processed by IONOLAB to improve its reliability and robustness [64]. The obtained GIM-TEC maps have a spatial resolution of 1° latitude and 1° longitude with temporal resolution of 15 minutes. Hence, $180 \times 360 \times 96$ dimensional datacube which contains 96 temporally different GIM-TEC maps is stored for each individual day. An example GIM-TEC is presented in Fig. 4.1 for a chosen date of 2017-01-19T11:00.

EQ related data is accessed via Advanced National Seismic System's comprehensive earthquake catalog (ANSS ComCat) [101]. Accessed EQ related data:

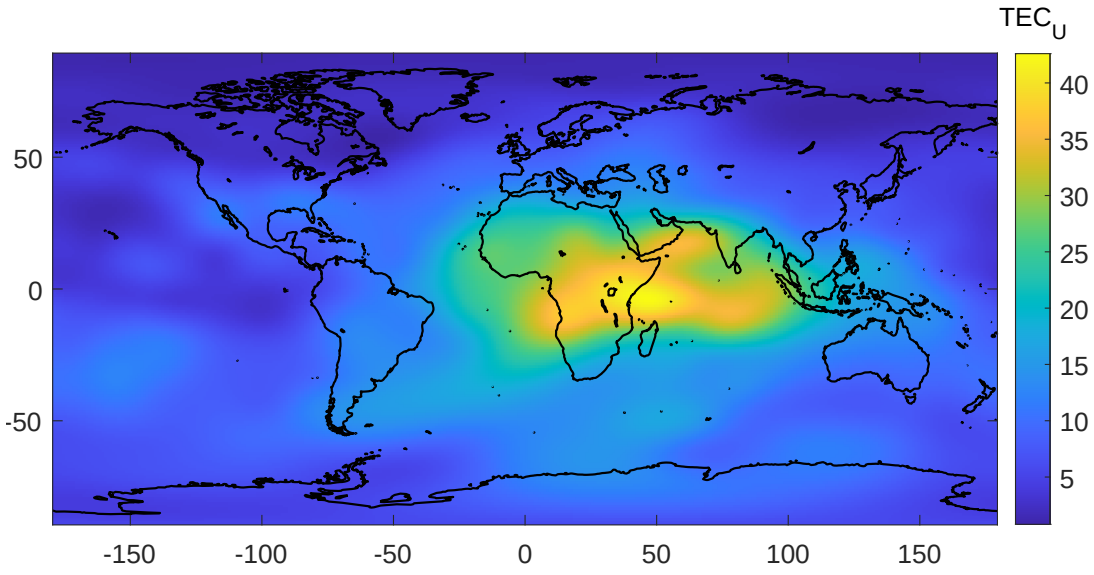

Figure 4.1: GIM-TEC map of the world for the date: 2017-01-19T11:00.

daily different EQ number and EQ date (first column), EQ time (second column), EQ epicenter (third and fourth columns) and EQ magnitude type (fifth column) is presented in Table 4.6.

4.2 Deep Learning based EQ Precursor Detection Technique: DL-PD

The collected GIM-TEC maps shall present detectable ionospheric anomalies that are related with the upcoming strong seismic activities and EQs [38, 102]. In this work, deep learning (DL) and ionospheric GIM-TEC based EQ precursor detection technique, DL-PD is proposed. The proposed shall detect EQ precursors in a daily basis by using the daily GIM-TEC data.

The collected GIM-TEC data exhibit both spatial and temporal TEC variations. Therefore, an anomaly detection technique that shall adopt to the spatio-temporal data is required. The proposed DL-PD technique generates spatio-temporal estimates of GIM-TEC maps which makes the detection of TEC based

ionospheric anomalies possible.

This section is organized as follows. In Section 4.2.1, pre-processing steps of obtained GIM-TEC data is presented. In Section 4.2.2, a deep neural network with spatio-temporal estimation capabilities is presented. Thereafter, EQ precursor detections are generated with respect to the ionospheric anomaly scores as discussed in Section 4.2.3. Flow diagram of the proposed DL-PD technique is visualized in Fig. 4.2.

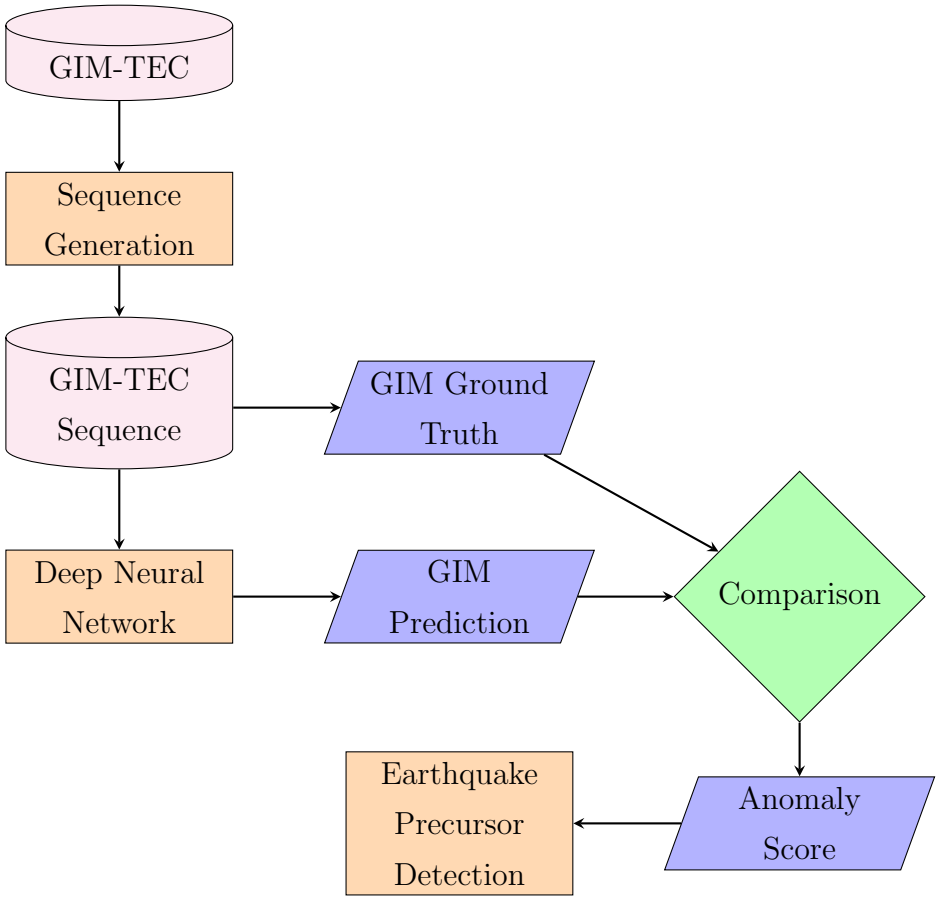

Figure 4.2: Flow diagram of the proposed deep learning based earthquake precursor detection technique, DL-PD.

4.2.1 GIM Pre-Processing

Each GIM-TEC map is spatially cropped with respect to a chosen area presented in Fig. 4.3. The chosen area is limited from -7.5° to 75.5° longitude and from 22.5° to 57.5° latitude. Anatolian region resides at the center of this chosen area and extends from 20.5° to 47.5° longitude and from 34.5° to 45.5° latitude. GIM-TEC map of the chosen area is illustrated in Fig. 4.3 for the GIM-TEC map of the chosen date in Fig. 4.1. EQ epicenters of the EQs with magnitudes greater or equal than 5.4 for the dates of 01.01.2000 and 31.12.2018 are also depicted in Fig. 4.3.

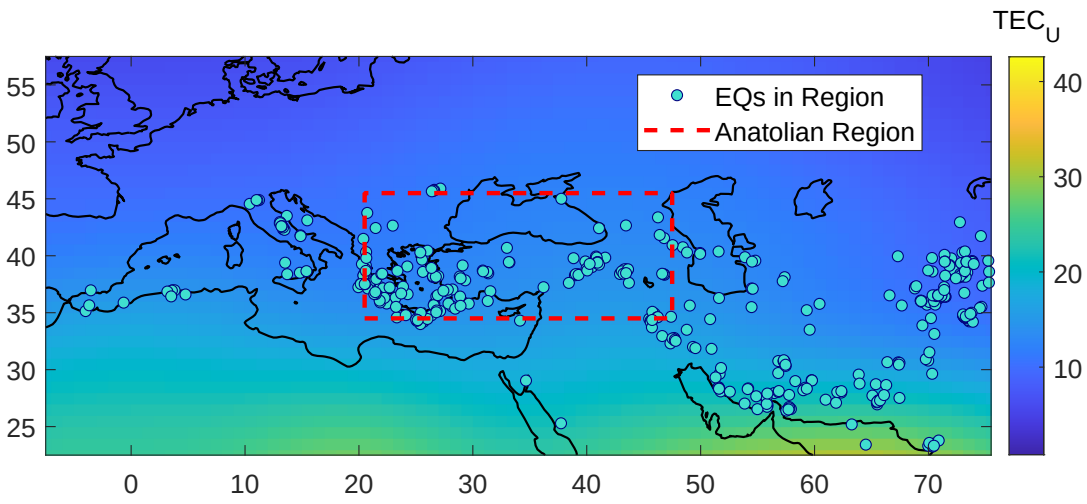

Figure 4.3: Cropped GIM-TEC map of the world for the date 2017-01-19T11:00. EQs with magnitudes greater or equal to 5.4 for the dates of 01.01.2000 and 31.12.2018. Anatolian region is marked with red dashed rectangle.

As shown in Fig. 4.3, GIM-TEC data of the chosen area corresponds to 36×84 dimensional matrix for each time frame. Hourly GIM-TEC data is generated by averaging GIM-TEC data with 15 minutes of time separation and a $36 \times 84 \times 24$ dimensional daily GIM-TEC data is generated. When the total number of days is defined as N_{days}, GIM-TEC data shall be represented as a 4 dimensional datacube with dimensions $36 \times 84 \times 24 \times N_{days}$.

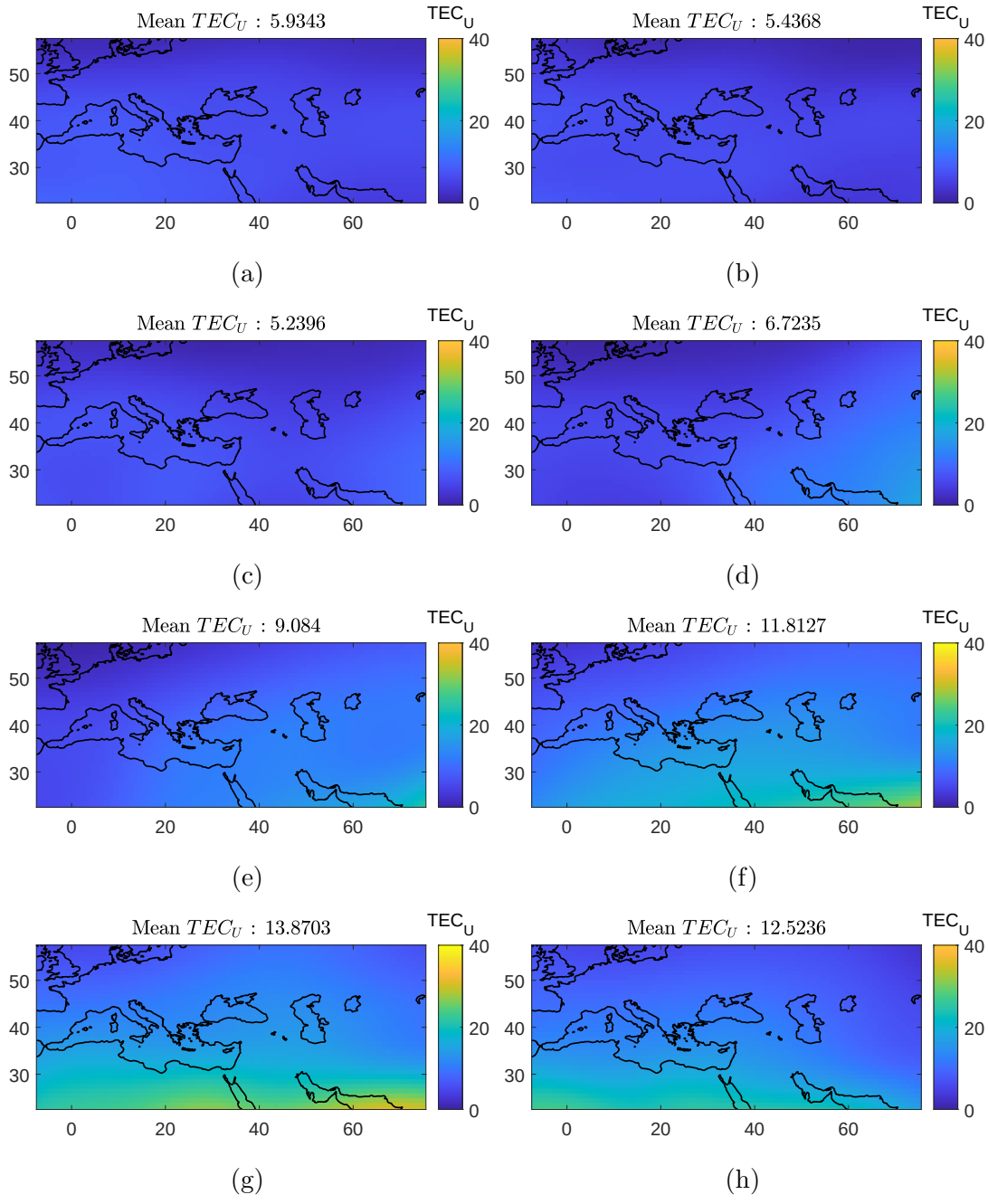

Figure 4.4: (a) 2$^{\text{nd}}$ (2017-01-18T22:00), (b) 4$^{\text{th}}$ (2017-01-19T00:00), (c) 6$^{\text{th}}$ (2017-01-19T02:00), (d) 8$^{\text{th}}$ (2017-01-19T04:00), (e) 10$^{\text{th}}$ (2017-01-19T06:00), (f) 12$^{\text{th}}$ (2017-01-19T08:00) and (g) 14$^{\text{th}}$ (2017-01-19T10:00) GIM-TEC data frames of a 15 timestep GIM-TEC sequence for the date: : 2017-01-19T11:00 (15$^{\text{th}}$ frame). (h) GIM-TEC ground truth of this sequence (2017-01-19T12:00).

Training of recurrent neural networks requires an input data such that each training sample of the data should include a temporal dimension or timesteps. Timesteps dimension defines a temporal data sequence for all spatial samples. Hourly GIM-TEC data shall be processed to generate hourly GIM-TEC sequences. When the number of timesteps is defined as N_{time}, past N_{time} hourly GIM-TEC data frames shall be merged to generate a GIM-TEC sequence for a chosen time and date. Hence, a GIM-TEC sequence shall be defined as a 3 dimensional datacube with $36 \times 84 \times N_{time}$ dimensions. Furthermore, upcoming GIM-TEC data frame with dimension of 36×84 shall be labeled as ground truth for this generated GIM-TEC sequence. The generated hourly GIM-TEC sequence data is a $36 \times 84 \times N_{time} \times 24N_{days}$ dimensional datacube with $36 \times 84 \times 24N_{days}$ dimensional GIM-TEC data ground truth. In Fig. 4.4, even number of GIM-TEC data frames of a 15 timestep GIM-TEC sequence is visualized for the the chosen date in Fig. 4.1. Ground truth of this GIM-TEC sequence is also visualized in Fig. 4.4h [113].

Each generated hourly GIM-TEC sequence is normalized with respect to maximum recorded TEC_U during N_{time} duration and constant minimum value of 0. Corresponding GIM-TEC ground truth of these generated sequences are also normalized with respect to the same minimum and maximum TEC_U values.

4.2.2 Deep Neural Network based GIM prediction

A deep learning neural network model is proposed to estimate upcoming hourly GIM-TEC by using a GIM-TEC sequence with N_{time} temporal samples and 36×84 spatial samples. The proposed model is presented in Fig. 4.5. As shown in Fig. 4.5, the proposed model is composed of Input, Convolutional LSTM (ConvLSTM), and 2-D convolutional neural network layers with a total 282,661 trainable parameters.

ConvLSTM layer is a type of LSTM layer that shall adopt to spatio-temporal data such as GIM-TEC [114],[115]. ConvLSTM layer features a cell memory for time t, c_t that accumulates the state information of the layer. The cell memory

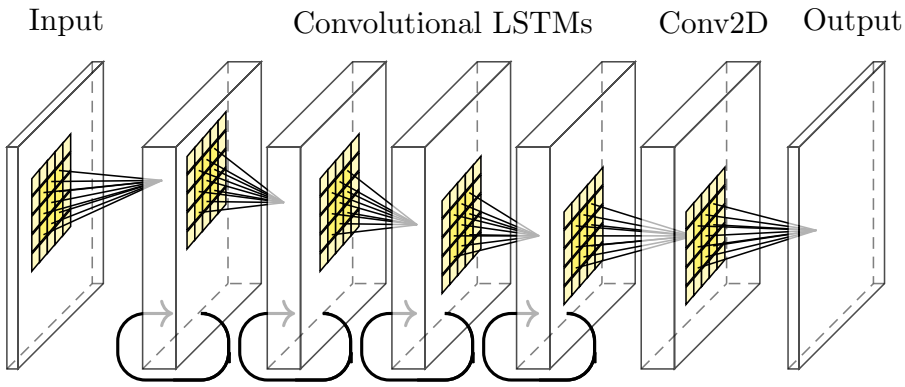

Figure 4.5: Proposed deep neural network with multiple spatio-temporal ConvLSTM layers.

shall be accessed, cleared or erased by control gates. Each of these gates shall have their own training parameters. When a new training sample is fed to the ConvLSTM, input gate i_t is activated. Forget gate, f_t shall remove previous cell state c_{t-1}during the training. Output gate, o_t decides if the latest cell state c_t should propagate through final hidden state h_t or not. Inputs $x_1, \ldots x_t$, cell states $c_1 \ldots c_t$, hidden states $h_1 \ldots h_t$, control gates i_t, f_t and o_t contain 3D spatio-temporal information for each time frame t. Equations of cell state activations are presented in (4.1).

$$
\begin{aligned}
i_t &= \sigma(W_{x,i} * x_t + W_{h,i} * h_{t-1} + W_{c,i} \circ c_{t-1} + b_i) \\
f_t &= \sigma(W_{x,f} * x_t + W_{h,f} * h_{t-1} + W_{c,f} \circ c_{t-1} + b_f) \\
o_t &= \sigma(W_{x,o} * x_t + W_{h,o} * h_{t-1} + W_{c,o} \circ c_t + b_o) \\
c_t &= f_t \circ c_{t-1} + i_t \circ \tanh(W_{c,c} * x_t + W_{h,c} * h_{t-1} + b_c) \\
h_t &= o_t \circ \tanh(c_t)
\end{aligned}
\tag{4.1}
$$

where $*$ denotes convolution, $\circ$ denotes Hadamard product, b_i, b_f, b_o denote input, forget and output gate biases. $W_{x,i}$, $W_{x,f}$, $W_{x,o}$, $W_{h,i}$, $W_{h,f}$, $W_{h,o}$, $W_{c,c}$ and $W_{h,c}$ denote the convolution kernels for the related control gate. An example ConvLSTM layer is visualized in Fig. 4.6 with convolution kernels are represented as W_x and W_h for simplicity.

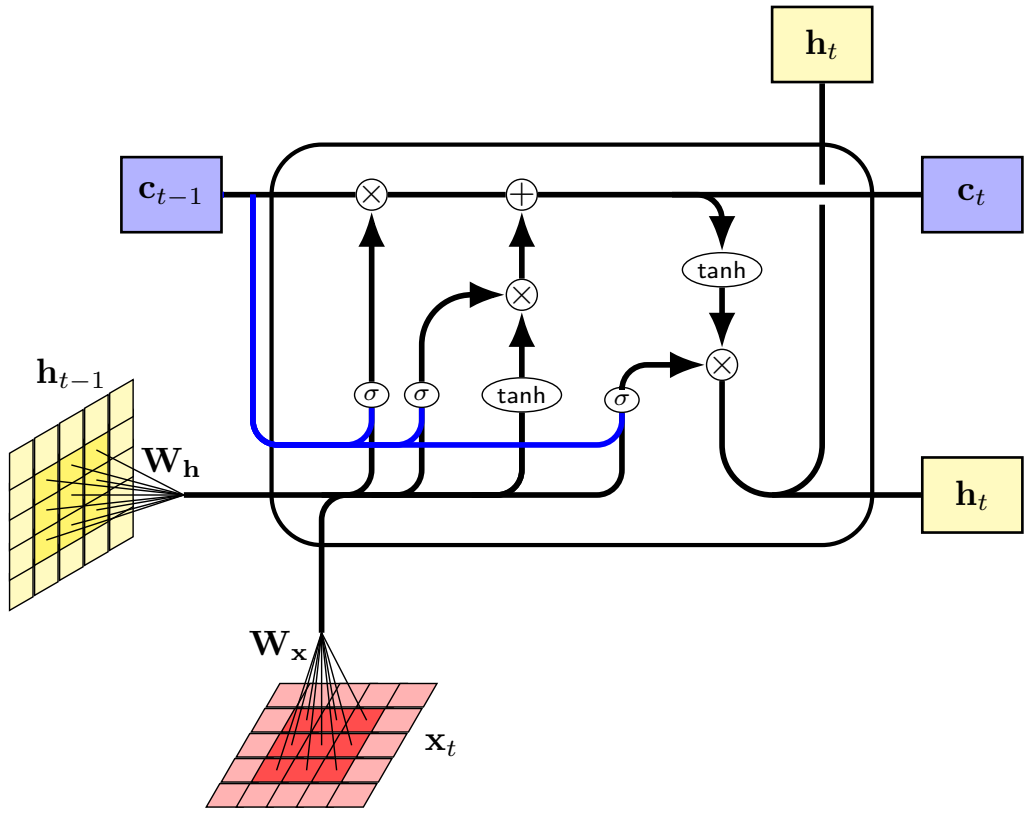

Figure 4.6: ConvLSTM layer with its spatio-temporal inputs x_t, control gates i_t, f_t, o_t, hidden states h_t and cell states c_t. Peephole connections are also visualized in blue.

Each ConvLSTM layer of the proposed network contains 20 different convolution filters that each one of these filters is 5×5 dimensional. First three ConvLSTM layers generate outputs as sequences while the last ConvLSTM layer only return the outputs of latest time frame. Conv2D layer contains only one convolution filter of size 3×3 and has a sigmoid activation function. Output shape of each layer that are presented in Fig. 4.5 are also presented in Table 4.1. As shown in Table 4.1, proposed deep neural network shall take GIM-TEC sequences and generate a GIM-TEC ground truth for a total of $N_{train,batch}$ samples. Additionally, batch normalization is performed after each ConvLSTM layer in order to reduce internal covariate shift between timesteps [116].

Table 4.1: For the proposed network, output shapes of each layer. Number of training samples are represented as $N_{train,batch}$.

Layer	Output Shape
Input	$N_{train,batch} \times N_{time} \times 36 \times 86 \times 1$
$\text{ConvLSTM}_1, \ldots, \text{ConvLSTM}_3$	$N_{train,batch} \times N_{time} \times 36 \times 86 \times 20$
ConvLSTM_4	$N_{train,batch} \times 36 \times 86 \times 20$
Conv2D	$N_{train,batch} \times 36 \times 86 \times 1$

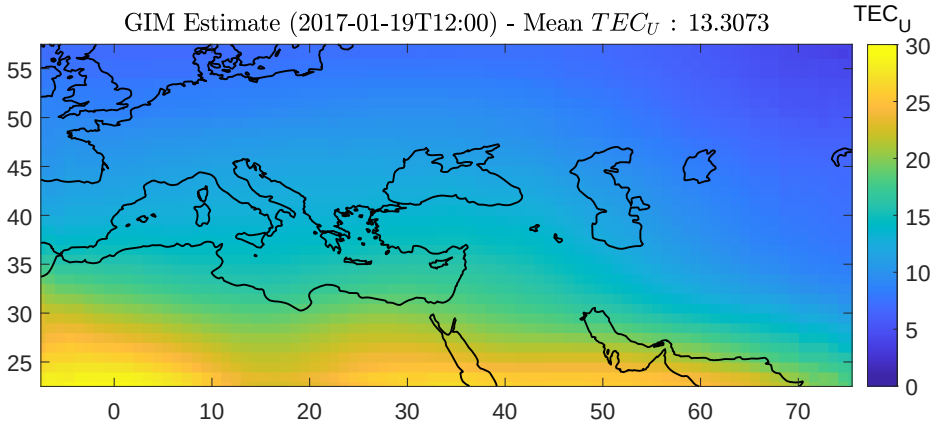

(a)

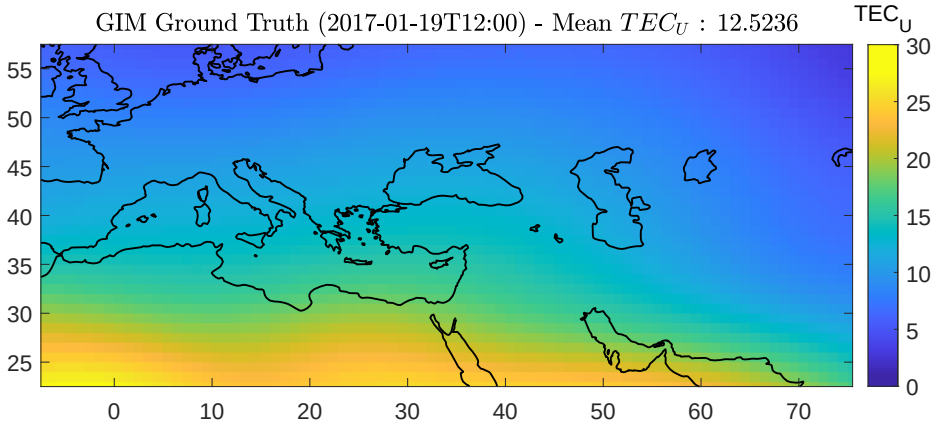

(b)

Figure 4.7: GIM-TEC estimate and GIM-TEC ground truth for the GIM-TEC sequence presented in Fig. 4.4.

GIM-TEC estimation performance of the proposed technique is visualized in Fig. 4.7 for the GIM TEC sequence presented in Fig. 4.4. As illustrated in Fig. 4.7, estimated GIM-TEC resembles the GIM-TEC ground truth of the upcoming hour that RMSE between the GIM-TEC ground truth and the GIM-TEC estimate is 1.0065 TEC_U.

Note that, the proposed deep neural network shall be trained in an unsupervised way. Therefore, explicit class labels are not required during the training of the proposed.

4.2.3 Earthquake Precursor Detection

Detection of an GIM-TEC anomaly requires comparing the GIM-TEC ground truth data with the norm or i.e. GIM-TEC estimates. Result of this comparison is the anomaly score of the compared GIM-TEC data. The anomaly score between these GIM-TEC data shall be calculated by using Structural Similarity Index Measure (SSIM) [117]. SSIM of two images I_1 and I_2 shall be calculated by multiplying luminance, $l(I_1, I_2)$, contrast, $c(I_1, I_2)$ and structure, $s(I_1, I_2)$ terms as follows:

$$l(I_1, I_2) = \frac{2\mu_{I_1}\mu_{I_2} + K_1}{\mu_{I_1}^2 + \mu_{I_2}^2 + K_1}, \tag{4.2}$$

$$c(I_1, I_2) = \frac{2\sigma_{I_1}\sigma_{I_2} + K_2}{\sigma_{I_1} + \sigma_{I_2} + K_2}, \tag{4.3}$$

$$s(I_1, I_2) = \frac{2\sigma_{I_1 I_2} + K_3}{\sigma_{I_1}^2\sigma_{I_2}^2 + K_3}, \tag{4.4}$$

$$SSIM(I_1, I_2) = l(I_1, I_2) \times c(I_1, I_2) \times s(I_1, I_2), \tag{4.5}$$

where μ_{I_1},μ_{I_2} are the pixel mean values, σ_{I_1},σ_{I_2} are the pixel standard deviations, and $\sigma_{I_1 I_2}$ is the cross-covariance for images I_1 and I_2. K_1, K_2 and K_3 are the constants to stabilize the division by weak denominator. $K_1 = (0.01L)^2$, $K_2 = (0.03L)^2$ and $K_3 = K_2/2$. L is the dynamic range of the image and for

a normalized GIM-TEC sequence which changes between $[0, 1]$, value of the L parameter shall be chosen as 1.

SSIM index is a similarity measure that satisfies symmetry $SSIM(I_1, I_2) = SSIM(I_2, I_1)$, boundedness $SSIM(I_1, I_2) \leq 1$ and unique maximum $SSIM(I_1, I_2) = 1 \Leftrightarrow I_1 = I_2$ conditions. Hence, minimum value of the SSIM index is 0 and maximum value of SSIM index is 1. SSIM index of the GIM-TEC estimate and GIM-TEC ground truth presented in Fig. 4.7 shall be obtained as 0.9566. When the value of the SSIM index is close to 1, similarity between the GIM-TEC estimate and GIM-TEC ground truth is high.

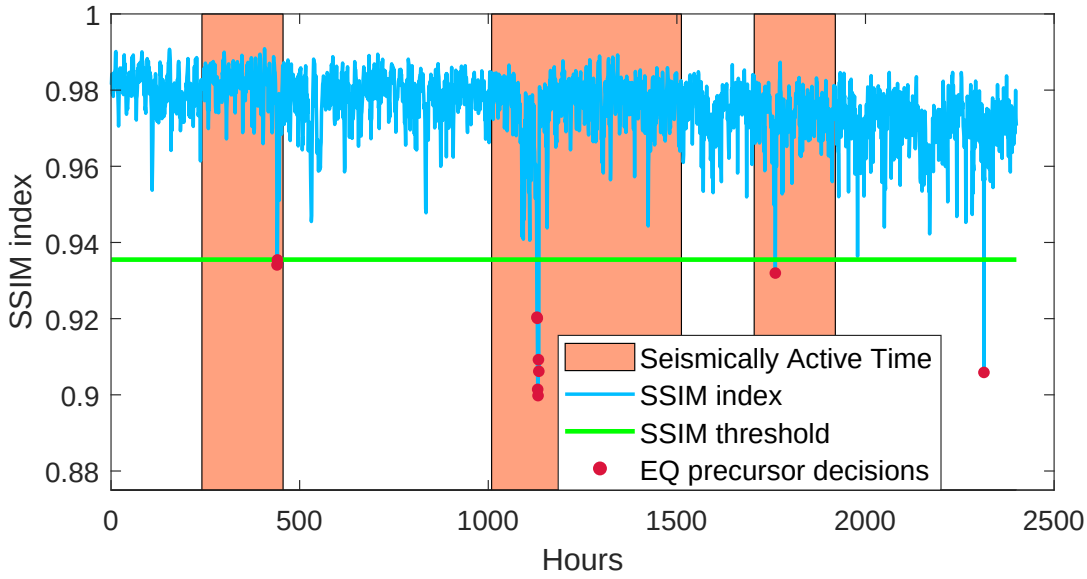

Figure 4.8: Seismic activity time, SSIM index, SSIM threshold and EQ precursor decisions for the last 100 days of 2017.

In order to investigate the relationship of the GIM-TEC anomalies and EQ precursors, last 100 days of 2017 are divided into seismic activity days and no-seismic activity days classes. Seismic activity days are separated with respect to 6 EQs with magnitudes greater or equal to 5 and 8 days prior to these daily different EQs including with the EQ days are selected for the seismic activity days. The proposed DL based neural network generates hourly GIM-TEC estimates. Hence, hours of each seismic activity day is also labeled as seismic activity time

and visualized with SSIM index between GIM-TEC ground truths and estimates for the last 100 days of 2017 in Fig. 4.8.

As illustrated in Fig. 4.8, a SSIM threshold shall be chosen to generate EQ precursor decisions. SSIM indices that are smaller than the chosen threshold shall be labeled as GIM-TEC anomalies. Generated GIM-TEC anomalies shall be associated with the seismic activity times that resulting GIM-TEC anomalies shall be called as EQ precursor decisions. The visualized EQ precursor decisions in Fig. 4.8, detects 4 out of 6 EQ precursors while generating 1 false EQ precursor decision out of 61 no-seismic activity days.

4.3 Performance of the Proposed DL based EQ Precursor Detection Technique

Precursor detection performance of the proposed DL-PD technique is investigated on a GIM-TEC data of 500 days duration for the chosen region presented in Fig. 4.3. Start and end dates, number of days and number of daily different EQs in this time period are presented Table 4.2. EQ precursor decisions are generated for the EQs in Anatolian region as presented in Fig. 4.3. As the spatial region gets larger, GIM-TEC anomalies shall be detected more reliably. However, larger spatial regions may result with simultaneous or consecutive EQs that number of seismically active days will be much higher than the no-seismic activity days. Therefore, performance evaluation is performed with GIM-TEC data of a larger chosen region with EQ epicenters of smaller Anatolian region.

Table 4.2: Processed GIM-TEC data information.

Date (D Month YYYY)		Number of Days	Number of daily different EQs
Start	End		
19 August 2016	31 December 2017	500	32

During the chosen time duration and Anatolian region, 32 daily different EQs

had taken place and presented in Table 4.6. All of the presented EQs had a magnitude greater than 5 in Richter scale [101]. If multiple EQs had taken place at the same day, the EQ with the highest magnitude is chosen for the performance evaluation. As shown in Table 4.6, 32 daily different EQs are investigated out of 37 total EQs.

As detailed in Section 4.2.1, obtained GIM-TEC data is pre-processed to generate hourly GIM-TEC sequences for the chosen 500 days duration. Number of timesteps N_{time} is chosen as 15 that generated GIM-TEC sequence data and GIM-TEC ground truth data have the dimensions of $36 \times 84 \times 15 \times 12000$ and $36 \times 84 \times 12000$, respectively. Note that, the generated GIM-TEC sequences data has a size of $\approx 2\ GB$ when each GIM pixel is represented with a single precision ($4\ bytes$) floating-point number. For the same number of timesteps and days duration, size of the GIM-TEC sequences data of whole world will be $\approx 43\ GB$.

The deep neural network that is proposed in Section 4.2.2 is trained for the generated GIM-TEC sequences and GIM-TEC ground truth data in an unsupervised way. Training parameters of the proposed are tabulated in Table 4.3. The proposed model is implemented in Python programming language and the proposed model is trained on a computer with a single NVIDIA Quadro RTX 8000 GPU.

Table 4.3: Model Training Parameters.

Training Parameter	Value
Learning Rate	0.0002, 0.0005, 0.001
Validation Split	%10
Number of Epochs	200
Batch Size	32
Optimizer	Adam($\beta_1 = 0.9$, $\beta_2 = 0.999$)
Loss	L2 Squared
Early Stopping	Validation loss decay, patience = 20
Performance Metric	PSNR

As shown in Table 4.3, Peak Signal to Noise Ratio (PSNR) is chosen as the appropriate performance evaluation metric. PSNR is a ratio between maximum possible power of image pixels, MAX_I and mean squared error, $MSE(I_1, I_2)$ between the compared images I_1,I_2 and defined below:

$$PSNR(I_1, I_2) = 10 \times \log_{10} \left(\frac{MAX_I^2}{MSE(I_1, I_2)} \right) \tag{4.6}$$

Both SSIM index and PSNR are the widely used image quality assessment metrics with different image quality sensitivities [118]. Training logs of the proposed network are presented in Fig. 4.9.

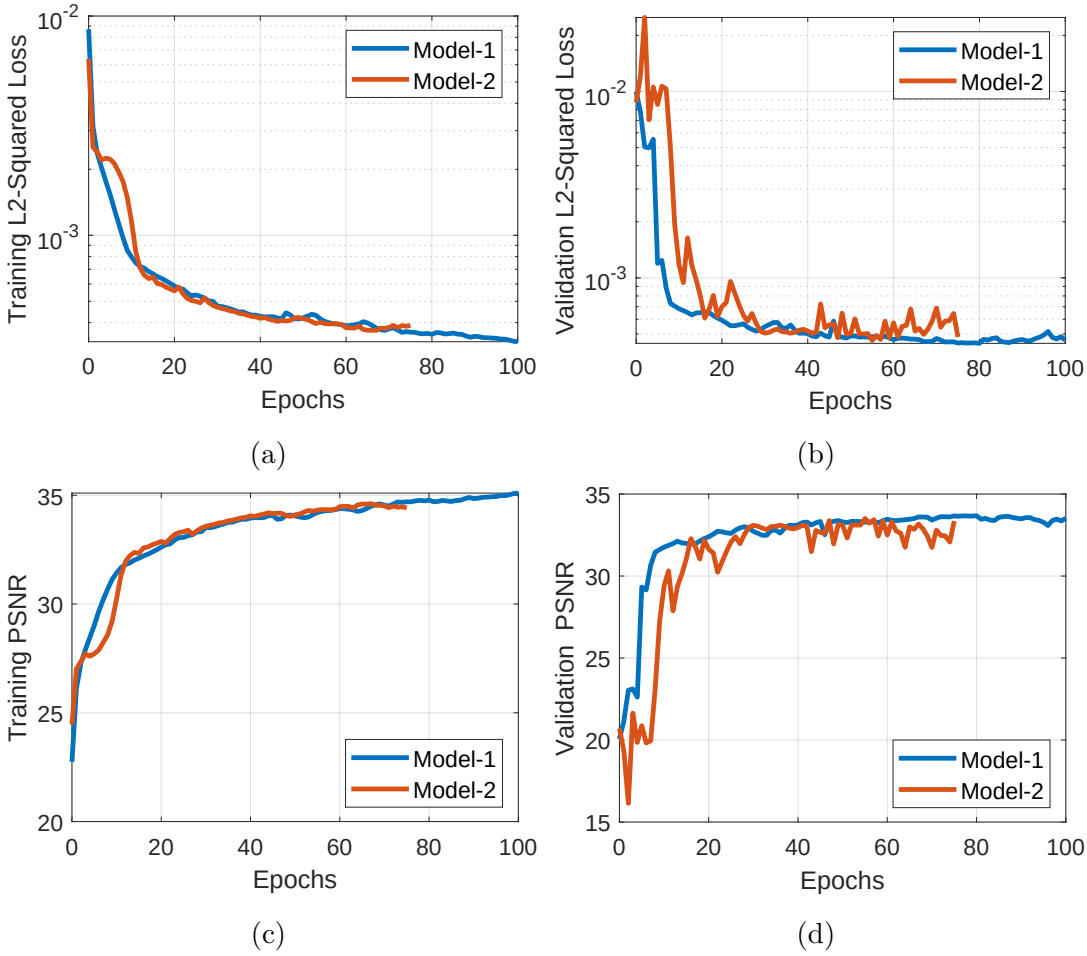

Figure 4.9: Training logs of the proposed model (a) Training loss, (b) Validation Loss, (c) Training PSNR and (d) Validation PSNR.

In Fig. 4.9, models whose validation PSNR value exceeds 32 are chosen and visualized among all the trained models. Furthermore, Model-1 and Model-2 are compared for validation. Model-1 is superior to Model-2 that it achieves lower training and validation losses and higher PSNR values during training and validation. Therefore, Model-1 is the validated model for performance evaluations.

Note that, GIM-TEC data that presented in Table 4.2 is also divided into 3 non-intersecting training, validation and test intervals. Last 15 days of the 2017 is separated for the test dataset. Remaining 475 days are used for training with %10 validation split. Mean SSIM index value for training and validation datasets is 0.9723. Similarly, mean SSIM index is 0.9653 for the test dataset. EQ precursor detection performance evaluations are performed for each day in Table 4.2. During these evaluations days are not divided with respect to their respective datasets, since GIM-TEC estimation performances of trainig, validation and test datasets are very close to each other.

As detailed in Section 4.2.3, EQ precursor decisions are generated for the dates presented in Table 4.2 and EQs presented in Table 4.6 by thresholding SSIM index which serves as an GIM-TEC anomaly score. Resulting EQ precursor detection ROC curves are presented in Fig. 4.10.

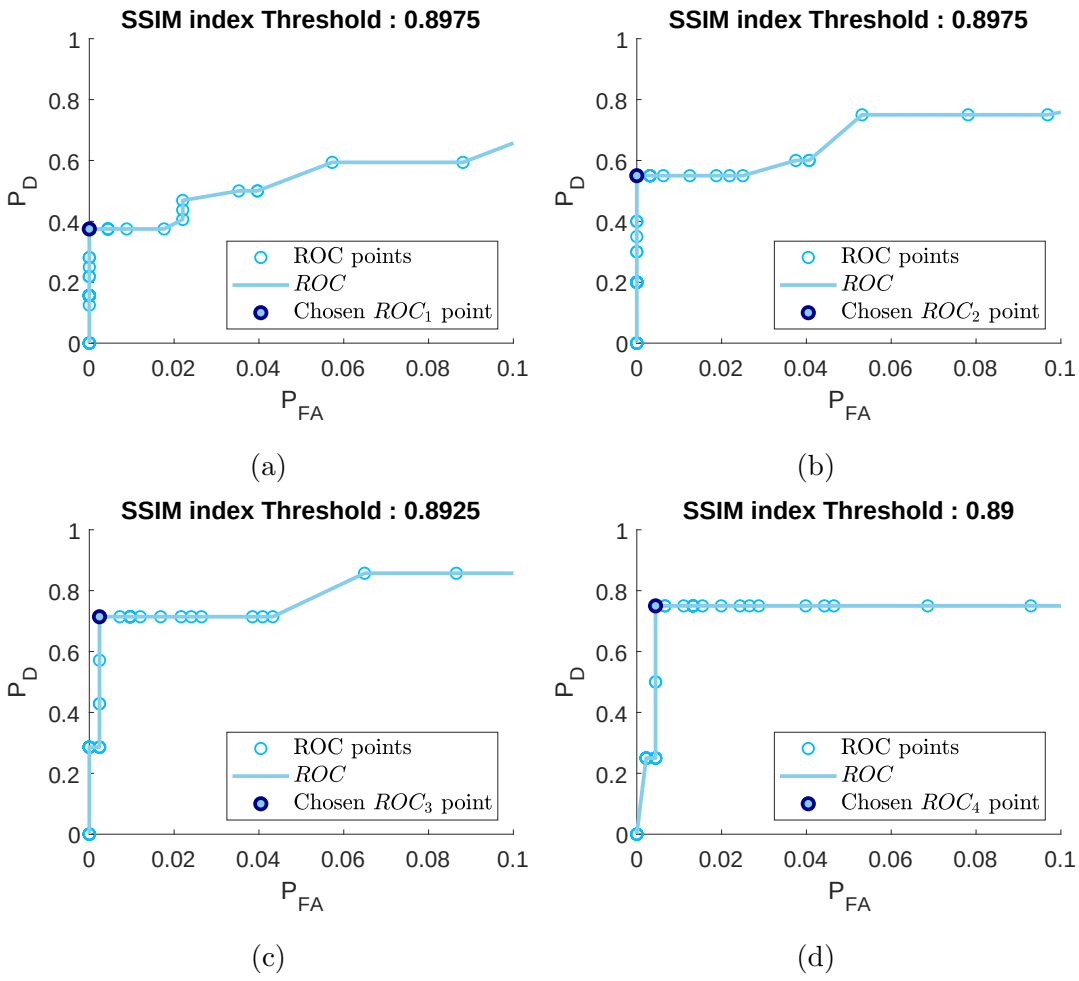

Figure 4.10: ROC curves based on EQ precursor detection performance for EQs with magnitudes (M) (a) M $\geq$ 5, (b) M $\geq$ 5.2, (c) M $\geq$ 5.4 and (d) M $\geq$ 5.6. Chosen ROC points (a) ROC_1, (b) ROC_2, (c) ROC_3 and (d) ROC_4.

When the generated ROC curves in Fig. 4.10 are taken into consideration, these curves exhibit both stepped and piece-vise linear sections in P_D axis. Stepped sections in P_D axis shall be attributed to the fact that P_D values are calculated with respect to small numbers of EQ precursors. As presented in Table 4.4, precursor detection performances are evaluated for 32 M $\geq$ 5 EQ precursors, 20 M $\geq$ 5.2 EQ precursors, 7 M $\geq$ 5.4 EQ precursors and 4 M $\geq$ 5.6 EQ precursors. Therefore, P_D shall take 32, 20, 7 and 4 distinct nonzero values during the performance evaluations in Fig. 4.10a, Fig. 4.10b, Fig. 4.10c and Fig.

4.10d, respectively. As shown in Fig. 4.10, piece-vise linear sections in P_D axis shall be attributed to the fact that operational ROC points are interpolated to generate the ROC curves. Hence, piece-vise linear sections of the ROC curves are not operational except vertices of these linear sections. Finally, the generated ROC curves are visualized for $0 \leq P_D \leq 1$ and $0 \leq P_{FA} \leq 0.1$ that performances of ROC points with $P_{FA} \geq 0.1$ are not taken into consideration during visualization. Note that number of possible false precursor decisions are higher than the number of all EQ precursors when $P_{FA} = 0.1$ and minimum EQ magnitude M $\geq$ 5.2.

As shown in Fig. 4.10, four different ROC curves are obtained for 4 different group of EQs and 4 different ROC points, ROC_1,ROC_2,ROC_3 and ROC_4, respectively. Number of detected EQ precursors, number of all EQs, number of false precursor decisions, number of no-seismic activity days are presented for the chosen ROC points in Table 4.4. As presented in both Fig. 4.10 and Table 4.4, the proposed DL-PD technique detects 5 out of 7 EQ precursors while generating 1 false EQ precursor decision out of 416 no-seismic activity days. SSIM threshold shall be selected between 0.90 and 0.89 to label a GIM-TEC estimate as an anomaly. Furthermore, probability of precursor detection increases as the magnitude of the desired EQs increases while generated false EQ precursor decisions remains low. Hence, the proposed achieves its highest performance when the EQ precursors that belong to EQs with magnitudes greater or equal to 5.4 are detected.

Note that, reliable positioning of precursor detection locations require further spatial processing techniques. In order to correlate a precursor detection with a specific EQ epicenter, seismic activity triggered spatial GIM-TEC variations should be processed and detected around the EQ epicenter. Such a detection technique requires processing multiple GIM-TEC regions independently and combining their SSIM based anomaly scores to position accurate precursor detection location. In this work, such a spatial processing technique is not implemented and left as a future work. Instead, a simple TEC difference based precursor detection distance positioning technique is implemented.

Each EQ precursor is detected by prior precursor decisions. Precursor decision location shall be obtained by comparing GIM-Estimate with GIM Ground truth of the date when the precursor decision is generated. Precursor decision location pixel is located by obtaining a pixel that has the highest TEC difference between GIM-Estimate and GIM Ground truth images. Precursor decision location shall be obtained by converting this pixel location into geodetic coordinates. Precursor detection distance, d_{prec} for an EQ shall be calculated by measuring the distance between EQ epicenter and precursor decision location information. Furthermore, multiple precursor decisions shall contribute to the detection of an EQ precursor. Therefore, multiple precursor detection distances shall also be obtained. When multiple precursor detection distances are generated, mean of these distances, $\sum d_{prec}$ represents the detection distance of the precursor. Mean precursor detection distances, $\sum d_{prec}$ and standard deviation of these precursor detection distances, $\sigma(\sum d_{prec})$ are presented in Table 4.5. As shown in Table 4.5, precursors of EQs with M $\geq$ 5.4 shall be detected from longer distances with smaller precursor detection distance standard deviations.

Table 4.4: For the chosen ROC points : number of detected EQ precursors, number of all EQs, number of false precursor decisions, number of false precursor decisions resulting with detection of weaker EQ precursors, number of no-seismic activity days (false alarm days), SSIM index threshold and minimum EQ magnitude in Richter scale.

ROC point	Detected EQ Precursors	Number of EQs	False Prec. Detections	Weaker EQ Prec. Detections	No-seismic activity days	SSIM index Threshold	Min EQ magnitude
ROC_1	12	32	0	0	227	0.8975	5
ROC_2	11	20	0	0	320	0.8975	5.2
ROC_3	5	7	1	1 M $\geq$ 5.2	416	0.8925	5.4
ROC_4	3	4	2	1 M $\geq$ 5.2 1 M $\geq$ 5.4	452	0.89	5.6

Table 4.5: For the chosen ROC points : Mean EQ precursor detection distances ($\sum d_{prec}$), standard deviation of EQ precursor detection distances ($\sigma(\sum d_{prec})$) and minimum EQ magnitude in Richter scale.

ROC point	$\sum d_{prec}$ Precursor Detection Distance (km)	$\sigma(\sum d_{prec})$ Precursor Detection Distance (km)	Min EQ magnitude
ROC_1	2042.8887	833.9594	5
ROC_2	2031.674	916.2285	5.2
ROC_3	2300.6086	632.8927	5.4
ROC_4	2235.5288	807.1093	5.6

Number of generated false precursor decisions that result with the detection of weaker EQ precursors are further investigated for the chosen ROC points. ROC_1 and ROC_2 points do not generate false precursor decisions. There is a false precursor decision of the ROC_3 point. As presented in Table 4.4, the precursor decision is a false precursor decision for the EQs with M $\geq$ 5.4 while it is a precursor detection for the EQs with M $\geq$ 5.2. Similarly, 2 false precursor decisions of ROC_4 point result with detection of 1 EQ precursor with EQ M $\geq$ 5.4 and another EQ precursor with EQ M $\geq$ 5.2. Hence, these false EQ precursor decisions shall be attributed to EQ precursors that belong to weaker EQs. Furthermore, EQ precursor decisions of the chosen ROC point, ROC_3 are visualized in Fig. 4.11. As illustrated in Fig. 4.11, there are 7 distinct seismically active time periods representing 7 different EQs with M $\geq$ 5.4. The false precursor decisions among these precursory decisions are also visualized in Fig. 4.12. There are three hourly different false precursory decisions that are 7, 10 and 13 hours prior to the seismically active time of the EQ that had taken place 20 July 2017 with magnitude M = 6.6 around Anatolia region. Since, these false hourly EQ precursor decisions are made at the same day, they are marked as 1 daily false EQ precursor decision for ROC_3 point in Table 4.4.

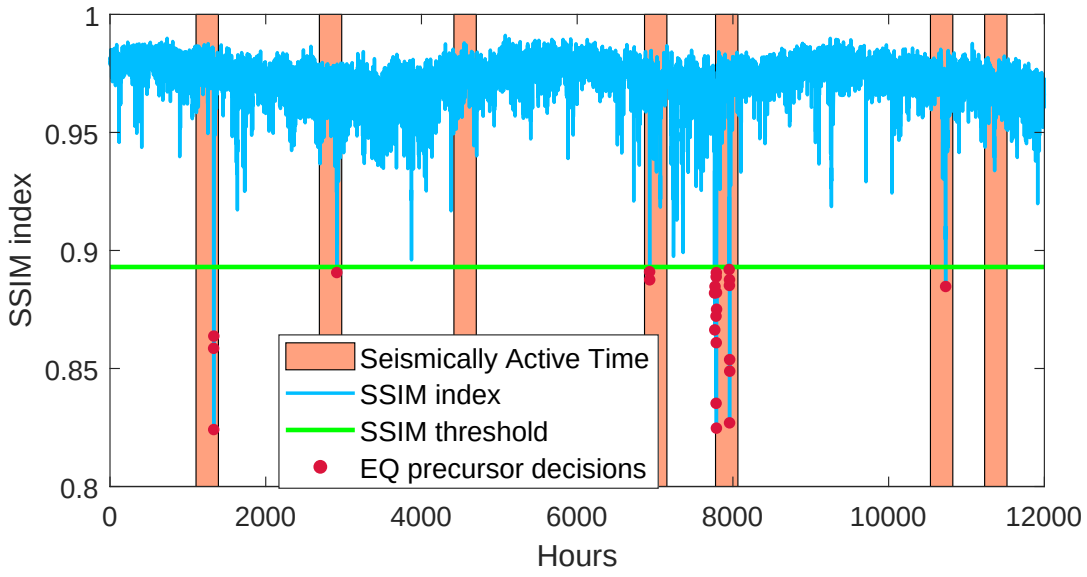

Figure 4.11: Seismic activity time, SSIM index, SSIM threshold and EQ precursor decisions for the last 500 days of 2017. Seismically active time is generated with respect to 7 different EQs with M $\geq$ 5.4.

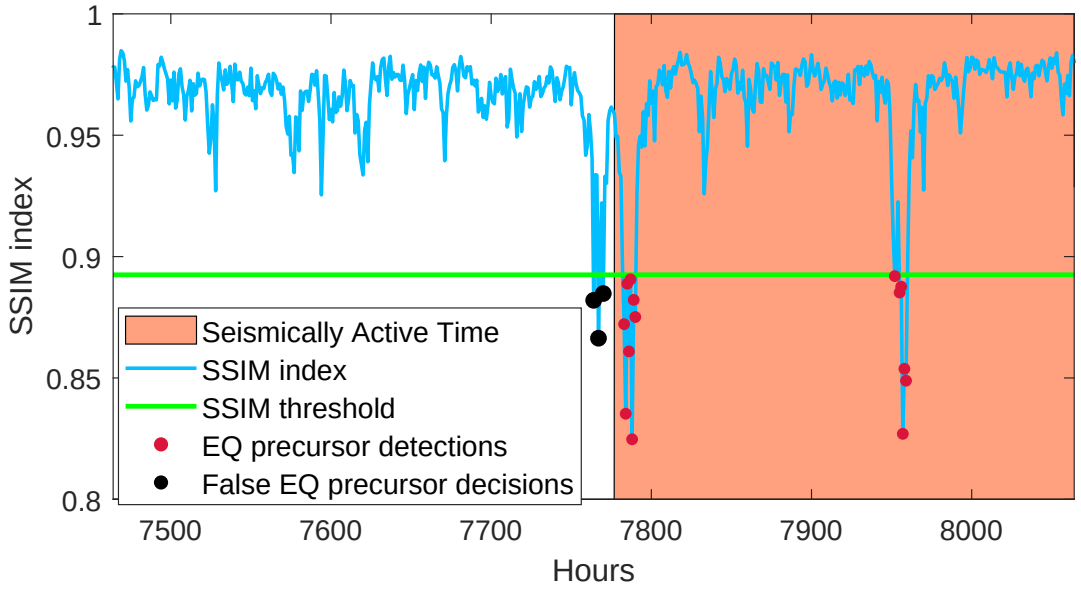

Figure 4.12: Seismic activity time, SSIM index, SSIM threshold, EQ precursor detections and false EQ precursor decisions for the last 25 days prior to the EQ that had taken place 20 July 2017 with magnitude M = 6.6 around Anatolia region.

Table 4.6: 32 daily different EQs that have taken place around Anatolian region.

EQ # - Date (# - DD Month YYYY)	Time (hh:mm:ss)	EQ Epicenter		Mw (Richter)
		Latitude	Longitude	
1 - 11 September 2016	13:10:08	42.0081°N	21.4876°E	5.1
2 - 27 September 2016	20:57:08	36.3888°N	27.6141°E	5.1
3 - 28 September 2016	07:17:35	36.7738°N	21.912°E	5
4 - 15 October 2016	08:18:32	42.2088°N	30.7242°E	5.1
4 - 15 October 2016	20:14:49	39.8063°N	20.6463°E	5.5
5 - 16 October 2016	00:09:58	39.7659°N	20.7143°E	5
5 - 16 October 2016	00:41:14	39.8168°N	20.5912°E	5.2
5 - 16 October 2016	02:21:04	39.7866°N	20.6113°E	5
6 - 20 December 2016	06:03:44	36.5393°N	26.9187°E	5.4
7 - 25 January 2017	18:50:51	35.3583°N	26.4196°E	5.2
8 - 06 February 2017	03:51:40	39.5986°N	26.0647°E	5.3
8 - 06 February 2017	10:58:02	39.5734°N	26.0755°E	5.2
9 - 07 February 2017	02:24:04	39.5279°N	26.0993°E	5.3
10 - 12 February 2017	13:48:16	39.6004°N	26.0884°E	5.3
11 - 02 March 2017	11:07:26	37.616°N	38.4305°E	5.6
12 - 13 April 2017	16:22:16	37.1253°N	28.6913°E	5
13 - 21 April 2017	13:09:22	38.7709°N	29.0638°E	5
14 - 03 May 2017	08:53:37	42.175°N	46.9611°E	5.2
15 - 11 May 2017	17:58:02	40.0382°N	40.7422°E	5.1
16 - 27 May 2017	15:53:24	38.7729°N	27.8234°E	5.1
17 - 12 June 2017	12:28:39	38.9296°N	26.365°E	6.3
18 - 17 June 2017	19:50:04	38.8864°N	26.4186°E	5.2
19 - 15 July 2017	20:30:17	34.925°N	25.4294°E	5.3
20 - 20 July 2017	22:31:11	36.9293°N	27.4139°E	6.6
21 - 21 July 2017	17:09:45	36.9074°N	27.3012°E	5
22 - 31 July 2017	21:29:14	34.5158°N	24.0577°E	5.3
23 - 08 August 2017	07:42:22	36.9645°N	27.5711°E	5.3

Continued on next page

Table 4.6 – continued from previous page

EQ # - Date (# - DD Month YYYY)	Time (hh:mm:ss)	EQ Epicenter		Mw (Richter)
		Latitude	Longitude	
24 - 23 August 2017	13:42:53	36.1833°N	44.9358°E	5.1
25 - 27 August 2017	23:14:52	37.9475°N	47.1318°E	5.2
26 - 11 September 2017	16:20:15	39.2104°N	21.5733°E	5
27 - 11 October 2017	22:49:44	39.1647°N	24.2379°E	5.1
28 - 12 November 2017	18:18:17	34.9109°N	45.9592°E	7.3
28 - 12 November 2017	18:29:52	34.9224°N	45.5873°E	5.3
29 - 15 November 2017	19:48:03	40.3082°N	47.3317°E	5.2
30 - 22 November 2017	20:22:53	37.0511°N	28.6427°E	5.1
31 - 24 November 2017	21:49:15	37.0845°N	28.6223°E	5.2
32 - 11 December 2017	14:09:57	35.0786°N	45.7614°E	5.4

4.4 Concluding Remarks

In this work, a deep learning based EQ precursor detection technique, DL-PD is presented and implemented by using GIM-TEC data obtained from the International GNSS Service Network (IGS). A deep learning based neural network is trained to predict upcoming GIM-TEC data and GIM-TEC estimation performance of this network is measured by SSIM index. Precursor decisions are generated by thresholding these SSIM indices.

Precursor detection performance of the proposed DL-PD technique is evaluated for 32 earthquakes occurred around Anatolian region with magnitudes higher than 5 in Richter scale. Precursor detection performance evaluations of the proposed technique indicate that the technique shall detect 11 out of 20 earthquake precursors that belongs to EQs with magnitudes greater than 5.2 and generate no false precursor decisions. For the EQs with magnitudes greater or equal to

5.4, the proposed shall detect 5 out of 7 earthquake precursors and generate 1 false precursor decision out of 416 no-seismic activity days. Results of this work suggests the fact that it is possible to implement the DL-PD technique in near real-time by monitoring anomalous behaviours in GIM-TEC data for a chosen region.

As future work, another deep learning architecture that shall take inputs of both GIM-TEC estimates and GIM-TEC ground truths or the statistics derived from these images shall generate EQ precursor decisions and their locations, when the new architecture is trained in a supervised way. Another future work shall be merging decisions of multiple DL based EQ precursor decisions in such a way that higher detection rates with lower false alarm rates shall be achieved. Finally, an accurate precursor location positioning technique shall be implemented by processing multiple GIM-TEC regions independently and combining their SSIM based anomaly scores.

Chapter 5

CONCLUSIONS

In this dissertation, Total Electron Content (TEC) anomaly detection techniques are developed by using model based, machine learning based and deep learning based techniques on various TEC data obtained from GNSS sensor networks. The developed techniques detect TEC anomalies by comparing a TEC estimate with the actual recorded TEC data.

In Chapter 2, a model based EQ precursor detection technique is presented with the TEC data obtained from the Turkish National Permanent GPS Network (TNPGN-Active). Local TEC variations are generated and thresholded by using TEC variation statistics obtained from a chosen region around Turkey for the days of 2011. Since the proposed technique is trained in a supervised way, days of 2011 are divided into 10 distinct day sets and 10-fold cross validation is performed for performance evaluation of the proposed. It is shown that the proposed technique shall detect 14 out of 23 EQ precursors while generating 8 false precursor decisions during 211 days of no-seismic activity.

In Chapter 3, a machine learning based EQ precursor detection technique, EQ-PD is presented with the TEC data obtained from EUREF Permanent GNSS Network (EPN) and geomagnetic parameter data obtained from NASA Goddard Space Flight Center OMNIWeb service. Local TEC variations are generated

and thresholded by using TEC variation statistics obtained from a chosen region around Italy for the days in between 01.01.2014 and 01.04.2015. EQ-PD technique is trained in a supervised way that labels of seismic activity and no-seismic activity day classes are used during the training. Hence, TEC data is divided into three non-intersecting time periods, training, validation and test for unbiased evaluation of precursor detection performance of the proposed. It is observed that for the validation set of dates the EQ-PD technique shall detect 17 out of 21 EQ precursors while generating 7 false precursor decisions during 120 days of no-seismic activity. Additionally, for the test set of dates the EQ-PD shall detect 22 out of 24 EQ precursors while generating 13 false precursor decisions during 147 days of no-seismic activity.

Finally in Chapter 4, a deep learning based EQ precursor detection technique, DL-PD is presented with the GIM-TEC data obtained from the International GNSS Service Network (IGS). A deep learning model that has the spatio-temporal data prediction capabilities is trained in an unsupervised way for the GIM-TEC data obtained from a chosen region around Europe for the days in between 19.08.2016 and 31.12.2017. A GIM-TEC anomaly score is obtained by measuring the similarity between GIM-TEC estimates and GIM-TEC ground truths. Generated GIM-TEC anomaly score is thresholded to obtain EQ precursor detection performance of the DL-PD technique. It is shown that the proposed technique shall detect 5 out of 7 EQ precursors while generating 1 false precursor decision during 416 days of no-seismic activity.

In conclusion, the proposed techniques have robust performances over geographically separated with reliable TEC data and for a wide range of time duration and resolution. They display remarkable precursor detection performances for EQs with different magnitudes.

As a future work for the Chapter 2, positions active fault lines shall be processed for better precursor detection performances. For the Chapter 3 of the dissertation, a future research direction shall be implementation of other cost-sensitive machine learning techniques to compare their EQ precursor detection performances with EQ-PD. For the Chapter 4, another deep neural network that

shall further process the GIM anomaly scores to generate EQ precursors shall be implemented. When all three EQ precursor detection techniques are considered, precursor detection performances of these techniques shall be compared with each other by choosing the same region and time duration during the performance evaluations.

Bibliography

[1] "FAQs, Can you predict earthquakes?, U.S. Geological Survey." https://www.usgs.gov/faqs/can-you-predict-earthquakes. Accessed: 2018-04-03.

[2] M. Wyss, "Cannot earthquakes be predicted?," *Science*, vol. 278, no. 5337, pp. 487–490, 1997.

[3] R. J. Geller, "Cannot earthquakes be predicted," in *Responses, Science 278 N5337*, Citeseer, 1997.

[4] R. J. Geller, "Earthquake prediction: a critical review," *Geophysical Journal International*, vol. 131, pp. 425–450, 1997.

[5] R. Bendick and R. Bilham, "Do weak global stresses synchronize earthquakes?," *Geophysical Research Letters*, vol. 44, no. 16, pp. 8320–8327, 2017.

[6] S. Kannan, "Innovative mathematical model for earthquake prediction," *Engineering Failure Analysis*, vol. 41, pp. 89–95, 2014.

[7] B. Papazachos and C. A. Papaioannou, "Long-term earthquake prediction in the aegean area based on a time and magnitude predictable model," *pure and applied geophysics*, vol. 140, no. 4, pp. 593–612, 1993.

[8] A. Boucouvalas, M. Gkasios, N. Tselikas, and G. Drakatos, "Modified-fibonacci-dual-lucas method for earthquake prediction," in *Proc. of SPIE Vol*, vol. 9535, pp. 95351A–1, 2015.

[9] M. Moustra, M. Avraamides, and C. Christodoulou, "Artificial neural networks for earthquake prediction using time series magnitude data or seismic electric signals," *Expert systems with applications*, vol. 38, no. 12, pp. 15032–15039, 2011.

[10] J. Mahmoudi, M. A. Arjomand, M. Rezaei, and M. H. Mohammadi, "Predicting the earthquake magnitude using the multilayer perceptron neural network with two hidden layers," *Civil engineering journal*, vol. 2, no. 1, pp. 1–12, 2016.

[11] G. Asencio-Cortés, F. Martínez-Álvarez, A. Morales-Esteban, and J. Reyes, "A sensitivity study of seismicity indicators in supervised learning to improve earthquake prediction," *Knowledge-Based Systems*, vol. 101, pp. 15–30, 2016.

[12] G. Asencio-Cortés, F. Martínez-Álvarez, A. Morales-Esteban, J. Reyes, and A. Troncoso, "Improving earthquake prediction with principal component analysis: application to chile," in *International Conference on Hybrid Artificial Intelligence Systems*, pp. 393–404, Springer, 2015.

[13] M. Last, N. Rabinowitz, and G. Leonard, "Predicting the maximum earthquake magnitude from seismic data in israel and its neighboring countries," *PloS one*, vol. 11, no. 1, p. e0146101, 2016.

[14] K. M. Asim, A. Idris, T. Iqbal, and F. Martínez-Álvarez, "Earthquake prediction model using support vector regressor and hybrid neural networks," *PloS one*, vol. 13, no. 7, p. e0199004, 2018.

[15] M. Shakeel, K. Itoyama, K. Nishida, and K. Nakadai, "Detecting earthquakes: a novel deep learning-based approach for effective disaster response," *Applied Intelligence*, pp. 1–11, 2021.

[16] R. Jena, B. Pradhan, A. Al-Amri, C. W. Lee, and H.-j. Park, "Earthquake probability assessment for the indian subcontinent using deep learning," *Sensors*, vol. 20, no. 16, p. 4369, 2020.

[17] M. Ibrahim, J. Park, and N. Athens, "Earthquake warning system: Detecting earthquake precursor signals using deep neural networks," *Technical Report CS 230*, 2018.

[18] Q. Wang, Y. Guo, L. Yu, and P. Li, "Earthquake prediction based on spatiotemporal data mining: An lstm network approach," *IEEE Transactions on Emerging Topics in Computing*, 2017.

[19] A. Panakkat and H. Adeli, "Recurrent neural network for approximate earthquake time and location prediction using multiple seismicity indicators," *Computer-Aided Civil and Infrastructure Engineering*, vol. 24, no. 4, pp. 280–292, 2009.

[20] L. Allegri, F. Bella, G. Della Monica, A. Ermini, S. Improta, V. Sgrigna, and P. Biagi, "Radon and rilt anomalies detected before the irpinia (south italy) earthquake of november 23, 1980 at great distances from the epicenter," *Geophysical Research Letters*, vol. 10, no. 4, pp. 269–272, 1983.

[21] J. Hartmann and J. K. Levy, "Hydrogeological and gasgeochemical earthquake precursors–a review for application," *Natural Hazards*, vol. 34, no. 3, pp. 279–304, 2005.

[22] T. Gulyaeva, F. Arikan, and I. Stanislawska, "Persistent long-term (1944–2015) ionosphere-magnetosphere associations at the area of intense seismic activity and beyond," *Advances in Space Research*, vol. 59, no. 4, pp. 1033–1040, 2017.

[23] S. Karatay, F. Arikan, and O. Arikan, "Investigation of total electron content variability due to seismic and geomagnetic disturbances in the ionosphere," *Radio Science*, vol. 45, no. 5, 2010.

[24] S. Pulinets, T. Gaivoronska, A. L. Contreras, L. Ciraolo, *et al.*, "Correlation analysis technique revealing ionospheric precursors of earthquakes," *Natural Hazards and Earth System Science*, vol. 4, no. 5/6, pp. 697–702, 2004.

[25] A. Namgaladze, O. Zolotov, I. Zakharenkova, I. Shagimuratov, and O. Martynenko, "Ionospheric total electron content variations observed before

earthquakes: Possible physical mechanism and modeling," *arXiv preprint arXiv:0905.3313*, 2009.

[26] K.-I. Oyama, M. Devi, K. Ryu, C. Chen, J. Liu, H. Liu, L. Bankov, and T. Kodama, "Modifications of the ionosphere prior to large earthquakes: report from the ionosphere precursor study group," *Geoscience Letters*, vol. 3, no. 1, p. 6, 2016.

[27] A. Tronin, P. Biagi, O. Molchanov, Y. Khatkevich, and E. Gordeev, "Temperature variations related to earthquakes from simultaneous observation at the ground stations and by satellites in Kamchatka area," *Physics and Chemistry of the Earth, Parts A/B/C*, vol. 29, no. 4, pp. 501–506, 2004.

[28] A. A. Tronin, M. Hayakawa, and O. A. Molchanov, "Thermal IR satellite data application for earthquake research in Japan and China," *Journal of Geodynamics*, vol. 33, no. 4, pp. 519–534, 2002.

[29] S. Pulinets, D. Ouzounov, A. Karelin, K. Boyarchuk, and L. Pokhmelnykh, "The physical nature of thermal anomalies observed before strong earthquakes," *Physics and Chemistry of the Earth, Parts A/B/C*, vol. 31, no. 4, pp. 143–153, 2006.

[30] G. Asteriadis and E. Livieratos, "Pre-seismic responses of underground water level and temperature concerning a 4.8 magnitude earthquake in greece on october 20, 1988," *Tectonophysics*, vol. 170, no. 1-2, pp. 165–169, 1989.

[31] R. A. Grant and T. Halliday, "Predicting the unpredictable; evidence of preseismic anticipatory behaviour in the common toad," *Journal of Zoology*, vol. 281, no. 4, pp. 263–271, 2010.

[32] C. Fidani, "The earthquake lights (EQL) of the 6 April 2009 Aquila earthquake, in Central Italy," *Nat. Hazards Earth Syst. Sci*, vol. 10, no. 5, pp. 967–978, 2010.

[33] S. Pulinets and D. Ouzounov, "Lithosphere–atmosphere–ionosphere coupling (laic) model–an unified concept for earthquake precursors validation," *Journal of Asian Earth Sciences*, vol. 41, no. 4-5, pp. 371–382, 2011.

[34] S. Pulinets and D. Davidenko, "The nocturnal positive ionospheric anomaly of electron density as a short-term earthquake precursor and the possible physical mechanism of its formation," *Geomagnetism and Aeronomy*, vol. 58, no. 4, pp. 559–570, 2018.

[35] S. Pulinets, K. Boyarchuk, A. Lomonosov, V. Khegai, and I. Y. Lyu, "Ionospheric precursors to earthquakes: a preliminary analysis of the fof2 critical frequencies at chung-li ground-based station for vertical sounding of the ionosphere (taiwan island)," *Geomagnetism and Aeronomy*, vol. 42, no. 4, pp. 508–513, 2002.

[36] J.-Y. Liu, Y.-I. Chen, H.-K. Jhuang, and Y.-H. Lin, "Ionospheric fof2 and tec anomalous days associated with m¿ or= 5.0 earthquakes in taiwan during 1997-1999," *Terrestrial Atmospheric and Oceanic Sciences*, vol. 15, no. 3, pp. 371–384, 2004.

[37] J.-Y. Liu, Y. Chen, Y. Chuo, and C.-S. Chen, "A statistical investigation of preearthquake ionospheric anomaly," *Journal of Geophysical Research: Space Physics*, vol. 111, no. A5, 2006.

[38] H. Le, J.-Y. Liu, and L. Liu, "A statistical analysis of ionospheric anomalies before 736 m6. 0+ earthquakes during 2002–2010," *Journal of Geophysical Research: Space Physics*, vol. 116, no. A2, 2011.

[39] S. Kon, M. Nishihashi, and K. Hattori, "Ionospheric anomalies possibly associated with m $\geq$ 6.0 earthquakes in the japan area during 1998–2010: Case studies and statistical study," *Journal of Asian Earth Sciences*, vol. 41, no. 4-5, pp. 410–420, 2011.

[40] S. Pulinets, "Seismic activity as a source of the ionospheric variability," *Advances in Space Research*, vol. 22, no. 6, pp. 903–906, 1998.

[41] S. Kouris, K. Polimeris, and L. R. Cander, "Specifications of TEC variability," *Advances in Space Research*, vol. 37, no. 5, pp. 983–1004, 2006.

[42] M. Akhoondzadeh, "Decision tree, bagging and random forest methods detect tec seismo-ionospheric anomalies around the time of the chile,(mw=

8.8) earthquake of 27 february 2010," *Advances in Space Research*, vol. 57, no. 12, pp. 2464–2469, 2016.

[43] D. Davidenko and S. Pulinets, "Deterministic variability of the ionosphere on the eve of strong (m $\geq$ 6) earthquakes in the regions of greece and italy according to long-term measurements data," *Geomagnetism and Aeronomy*, vol. 59, no. 4, pp. 493–508, 2019.

[44] J. Liu, Y. Chen, S. Pulinets, Y. Tsai, and Y. Chuo, "Seismo-ionospheric signatures prior to M$\geq$ 6.0 Taiwan earthquakes," *Geophysical research letters*, vol. 27, no. 19, pp. 3113–3116, 2000.

[45] J. Y. Liu, Y. Chuo, S. Shan, Y. Tsai, Y. Chen, S. Pulinets, S. Yu, *et al.*, "Pre-earthquake ionospheric anomalies registered by continuous GPS TEC measurements," in *Annales Geophysicae*, vol. 22, pp. 1585–1593, 2004.

[46] J. Liu, C. Chen, Y. Chen, W. Yang, K. Oyama, and K. Kuo, "A statistical study of ionospheric earthquake precursors monitored by using equatorial ionization anomaly of gps tec in taiwan during 2001–2007," *Journal of Asian Earth Sciences*, vol. 39, no. 1, pp. 76–80, 2010.

[47] M. Devi, A. Medhi, A. J. D. S. Sarma, and A. K. Barbara, "Growth and inhibition of equatorial anomaly prior to an earthquake (eq): case studies with total electron content (tec) data for major eqs of japan 2011 and indonesia 2012," *Positioning*, vol. 2013, 2013.

[48] D. Ouzounov, S. Pulinets, A. Romanov, A. Romanov, K. Tsybulya, D. Davidenko, M. Kafatos, and P. Taylor, "Atmosphere-ionosphere response to the M9 Tohoku earthquake revealed by multi-instrument space-borne and ground observations: Preliminary results," *Earthquake Science*, vol. 24, no. 6, pp. 557–564, 2011.

[49] O. Zolotov, A. Namgaladze, and B. Prokhorov, "Specific features of ionospheric total electron content variations in the periods of preparation of the earthquakes on march 11, 2011 (japan) and october 23, 2011 (turkey)," *Russian Journal of Physical Chemistry B*, vol. 7, no. 5, pp. 599–605, 2013.

[50] K. S. Yadav, S. P. Karia, and K. N. Pathak, "Anomalous variation in gps based tec prior to the 5 earthquakes in 2009 and 2010," *Positioning*, vol. 6, no. 04, p. 96, 2015.

[51] A. Trigunait, M. Parrot, S. Pulinets, and F. Li, "Variations of the ionospheric electron density during the bhuj seismic event," in *Annales Geophysicae*, vol. 22, pp. 4123–4131, Copernicus GmbH, 2004.

[52] W. Li, J. Guo, J. Yue, Y. Yang, Z. Li, and D. Lu, "Contrastive research of ionospheric precursor anomalies between calbuco volcanic eruption on april 23 and nepal earthquake on april 25, 2015," *Advances in space research*, vol. 57, no. 10, pp. 2141–2153, 2016.

[53] M. Zhang, J. Shi, X. Wang, and S. Radicella, "Ionospheric variability at low latitude station: Hainan, China," *Advances in Space Research*, vol. 34, no. 9, pp. 1860–1868, 2004.

[54] S. Pulinets, "Ionospheric precursors of earthquakes; recent advances in theory and practical applications," *Terrestrial Atmospheric and Oceanic Sciences*, vol. 15, no. 3, pp. 413–436, 2004.

[55] S. Pulinets, A. Leyva-Contreras, G. Bisiacchi-Giraldi, and C. Ciraolo, "Total electron content variations in the ionosphere before the Colima, Mexico, earthquake of 21 January 2003," *Geofísica Internacional*, vol. 44, no. 4, 2005.

[56] V. Plotkin, "GPS detection of ionospheric perturbation before the 13 February 2001, El Salvador earthquake," *Natural Hazards and Earth System Science*, vol. 3, no. 3/4, pp. 249–253, 1999.

[57] S. Kouris and D. Fotiadis, "Ionospheric variability: a comparative statistical study," *Advances in Space Research*, vol. 29, no. 6, pp. 977–985, 2002.

[58] S. Pulinets, A. Kotsarenko, L. Ciraolo, and I. Pulinets, "Special case of ionospheric day-to-day variability associated with earthquake preparation," *Advances in Space Research*, vol. 39, no. 5, pp. 970–977, 2007.

[59] F. Arikan, M. Deviren, O. Lenk, U. Sezen, and O. Arikan, "Observed ionospheric effects of 23 october 2011 van, turkey earthquake," *Geomatics, Natural Hazards and Risk*, vol. 3, no. 1, pp. 1–8, 2012.

[60] A. A. Akyol, "Investigation on the Reliability of Earthquake Prediction Based on Ionospheric Electron Content Variation," Master's thesis, Bilkent University, Ankara, 2013.

[61] A. A. Akyol, O. Arikan, F. Arikan, and M. N. Deviren, "Investigation on the reliability of earthquake prediction based on ionospheric electron content variation," in *Information Fusion (FUSION), 2013 16th International Conference on*, pp. 1658–1663, IEEE, 2013.

[62] A. A. Akyol, O. Arikan, and F. Arikan, "A machine learning-based detection of earthquake precursors using ionospheric data," *Radio Science*, vol. 55, no. 11, pp. 1–21, 2020.

[63] U. Sezen, F. Arikan, O. Arikan, O. Ugurlu, and A. Sadeghimorad, "Online, automatic, near-real time estimation of gps-tec: Ionolab-tec," *Space Weather*, vol. 11, no. 5, pp. 297–305, 2013.

[64] "IONOLAB, Ionospheric Research Laboratory." http://www.ionolab.org/. Accessed: 2022-01-01.

[65] M. Deviren, F. Arikan, and O. Arikan, "Spatio-temporal interpolation of total electron content using a gps network," *Radio Science*, vol. 48, no. 3, pp. 302–309, 2013.

[66] SILSO World Data Center, "The International Sunspot Number," *International Sunspot Number Monthly Bulletin and online catalogue*, 2005-2016.

[67] K. G. Mehrotra, C. K. Mohan, and H. Huang, *Anomaly detection principles and algorithms*. Springer, 2017.

[68] N. Turel and F. Arikan, "Probability density function estimation for characterizing hourly variability of ionospheric total electron content," *Radio Science*, vol. 45, no. 6, 2010.

[69] S. Karatay, F. Arikan, and O. Arikan, "Investigation of Hourly and Daily Patterns for Lithosphere-Ionosphere Coupling Before Strong Earthquakes," *Recent Advances in Space Research*, 2009.

[70] M. L. Stein, *Interpolation of spatial data: some theory for kriging*. Springer, 1999.

[71] I. Stanislawska, G. Juchnikowski, L. R. Cander, L. Ciraolo, P. Bradley, Z. Zbyszynski, and A. Swiatek, "The kriging method of TEC instantaneous mapping," *Advances in Space Research*, vol. 29, no. 6, pp. 945–948, 2002.

[72] M. Sugiura, T. Kamei, A. Berthelier, and M. Menvielle, *Equatorial Dst Index: 1957-1986*. ISGI Publications Office, 1991.

[73] T. Gulyaeva and I. Stanislawska, "Derivation of a planetary ionospheric storm index," in *Annales Geophysicae*, vol. 26, pp. 2645–2648, Copernicus GmbH, 2008.

[74] A. Mikhailov, A. Depueva, V. Depuev, *et al.*, "Daytime f2-layer negative storm effect: what is the difference between storm-induced and q-disturbance events?," in *Annales Geophysicae*, vol. 25, pp. 1531–1541, 2007.

[75] C. Lee and D. A. Landgrebe, "Feature extraction based on decision boundaries," *IEEE Transactions on Pattern Analysis and Machine Intelligence*, vol. 15, no. 4, pp. 388–400, 1993.

[76] I. B. Aban, M. M. Meerschaert, and A. K. Panorska, "Parameter estimation for the truncated Pareto distribution," *Journal of the American Statistical Association*, vol. 101, no. 473, pp. 270–277, 2006.

[77] L. Zaninetti and M. Ferraro, "On the truncated Pareto distribution with applications," *Central European Journal of Physics*, vol. 6, no. 1, pp. 1–6, 2008.

[78] A. A. Akyol, O. Ankan, and F. Ankan, "Generation of earthquake detection signal based on ionospheric electron content variation," in *2014 22nd Signal Processing and Communications Applications Conference (SIU)*, pp. 590–593, IEEE, 2014.

[79] W. Elmenreich, "A review on system architectures for sensor fusion applications," in *Software Technologies for Embedded and Ubiquitous Systems*, pp. 547–559, Springer, 2007.

[80] R. C. Eberhart and Y. Shi, "Particle swarm optimization: developments, applications and resources," in *evolutionary computation, 2001. Proceedings of the 2001 Congress on*, vol. 1, pp. 81–86, IEEE, 2001.

[81] C. Kuo, J. Huba, G. Joyce, and L. Lee, "Ionosphere plasma bubbles and density variations induced by pre-earthquake rock currents and associated surface charges," *Journal of Geophysical Research*, vol. 116, no. A10, p. A10317, 2011.

[82] R. Kohavi *et al.*, "A study of cross-validation and bootstrap for accuracy estimation and model selection," in *Ijcai*, vol. 14, pp. 1137–1145, 1995.

[83] T. Dietterich, "Overfitting and undercomputing in machine learning," *ACM computing surveys (CSUR)*, vol. 27, no. 3, pp. 326–327, 1995.

[84] J. Fürnkranz, "Pruning algorithms for rule learning," *Machine Learning*, vol. 27, no. 2, pp. 139–172, 1997.

[85] C. Scott, "Performance measures for neyman–pearson classification," *Information Theory, IEEE Transactions on*, vol. 53, no. 8, pp. 2852–2863, 2007.

[86] K. Davies and G. Hartmann, "Studying the ionosphere with the global positioning system," *Radio Science*, vol. 32, no. 4, pp. 1695–1703, 1997.

[87] F. Arikan, C. Erol, and O. Arikan, "Regularized estimation of vertical total electron content from gps data for a desired time period," *Radio Science*, vol. 39, no. 6, 2004.

[88] I. Sayin, F. Arikan, and O. Arikan, "Regional tec mapping with random field priors and kriging," *Radio Science*, vol. 43, no. 5, 2008.

[89] F. Arikan, C. Erol, and O. Arikan, "Regularized estimation of vertical total electron content from Global Positioning System data," *Journal of Geophysical Research*, vol. 108, no. A12, p. 1469, 2003.

[90] C. Bruyninx, H. Habrich, W. Söhne, A. Kenyeres, G. Stangl, and C. Völksen, "Enhancement of the euref permanent network services and products," in *Geodesy for Planet Earth*, pp. 27–34, Springer, 2012.

[91] F. Arikan, O. Arikan, and C. B. Erol, "Regularized estimation of tec from gps data for certain midlatitude stations and comparison with the iri model," *Advances in Space Research*, vol. 39, no. 5, pp. 867–874, 2007.

[92] H. Nayir, F. Arikan, O. Arikan, and C. Erol, "Total electron content estimation with reg-est," *Journal of Geophysical Research: Space Physics*, vol. 112, no. A11, 2007.

[93] F. Arikan, H. Nayir, U. Sezen, and O. Arikan, "Estimation of single station interfrequency receiver bias using gps-tec," *Radio Science*, vol. 43, no. 4, 2008.

[94] M. Mandea and M. Korte, *Geomagnetic observations and models*, vol. 5. Springer, 2010.

[95] T. Fuller-Rowell, M. Codrescu, and P. Wilkinson, "Quantitative modeling of the ionospheric response to geomagnetic activity," in *Annales Geophysicae*, vol. 18, pp. 766–781, Copernicus GmbH, 2000.

[96] T. Gulyaeva, F. Arikan, I. Stanislawska, and L. Poustovalova, "Global distribution of zones of enhanced risk for the ionospheric weather," *Journal of Geography, Environment and Earth Science International*, vol. 4, no. 1, pp. 1–13, 2016.

[97] T. Gulyaeva and F. Arikan, "Statistical discrimination of global postseismic ionosphere effects under geomagnetic quiet and storm conditions," *Geomatics, Natural Hazards and Risk*, vol. 8, no. 2, pp. 509–524, 2017.

[98] T. Gulyaeva, F. Arikan, and I. Stanislawska, "Earthquake aftereffects in the equatorial ionization anomaly region under geomagnetic quiet and storm conditions," *Advances in Space Research*, vol. 60, no. 2, pp. 406–418, 2017.

[99] G. Rostoker, "Geomagnetic indices," *Reviews of Geophysics*, vol. 10, no. 4, pp. 935–950, 1972.

[100] "NASA OMNIWeb, SPDF Goddard Space Flight Center." https://omniweb.gsfc.nasa.gov/form/dx1.html. Accessed: 2017-04-17.

[101] "ANSS Comprehensive Catalog (ComCat), U.S. Geological Survey." https://earthquake.usgs.gov/earthquakes/search/. Accessed: 2017-04-17.

[102] D. Ouzounov, S. Pulinets, K. Hattori, and P. Taylor, *Pre-earthquake processes: A multidisciplinary approach to earthquake prediction studies*, vol. 234. John Wiley & Sons, 2018.

[103] F. Arikan, S. Shukurov, H. Tuna, O. Arikan, and T. Gulyaeva, "Performance of gps slant total electron content and iri-plas-stec for days with ionospheric disturbance," *Geodesy and Geodynamics*, vol. 7, no. 1, pp. 1–10, 2016.

[104] M. Necat Deviren, T. Gulyaeva, U. Sezen, F. Arikan, and O. Arikan, "Detection of seismic precursors using distance metrics between gps-tec and iri-plas," in *40th COSPAR Scientific Assembly*, vol. 40, 2014.

[105] P. J. Rousseeuw, "Silhouettes: a graphical aid to the interpretation and validation of cluster analysis," *Journal of computational and applied mathematics*, vol. 20, pp. 53–65, 1987.

[106] L. Kaufman and P. J. Rousseeuw, *Finding groups in data: an introduction to cluster analysis*, vol. 344. John Wiley & Sons, 2009.

[107] S. Karatay, F. Arikan, and O. Arikan, "Investigation of hourly and daily patterns for lithosphere-ionosphere coupling before strong earthquakes," in *Recent Advances in Space Technologies, 2009. RAST'09. 4th International Conference on*, pp. 670–674, IEEE, 2009.

[108] C. Cortes and V. Vapnik, "Support-vector networks," *Machine learning*, vol. 20, no. 3, pp. 273–297, 1995.

[109] C. J. Burges, "A tutorial on support vector machines for pattern recognition," *Data mining and knowledge discovery*, vol. 2, no. 2, pp. 121–167, 1998.

[110] J. Platt, "Sequential minimal optimization: A fast algorithm for training support vector machines," 1998.

[111] B. W. Matthews, "Comparison of the predicted and observed secondary structure of t4 phage lysozyme," *Biochimica et Biophysica Acta (BBA)-Protein Structure*, vol. 405, no. 2, pp. 442–451, 1975.

[112] J.-I. G. S. Data, "Crustal dynamics data information system (cddis)," 2022. Last accessed 01 January 2022.

[113] T. Cooijmans, N. Ballas, C. Laurent, Ç. Gülçehre, and A. Courville, "Recurrent batch normalization," *arXiv preprint arXiv:1603.09025*, 2016.

[114] S. Xingjian, Z. Chen, H. Wang, D.-Y. Yeung, W.-K. Wong, and W.-c. Woo, "Convolutional lstm network: A machine learning approach for precipitation nowcasting," in *Advances in neural information processing systems*, pp. 802–810, 2015.

[115] A. Graves, "Generating sequences with recurrent neural networks," *arXiv preprint arXiv:1308.0850*, 2013.

[116] C. Laurent, G. Pereyra, P. Brakel, Y. Zhang, and Y. Bengio, "Batch normalized recurrent neural networks," in *2016 IEEE International Conference on Acoustics, Speech and Signal Processing (ICASSP)*, pp. 2657–2661, IEEE, 2016.

[117] Z. Wang, A. C. Bovik, H. R. Sheikh, and E. P. Simoncelli, "Image quality assessment: from error visibility to structural similarity," *IEEE transactions on image processing*, vol. 13, no. 4, pp. 600–612, 2004.

[118] A. Hore and D. Ziou, "Image quality metrics: Psnr vs. ssim," in *2010 20th international conference on pattern recognition*, pp. 2366–2369, IEEE, 2010.